UNDERSTANDING DIATOMIC MOLECULAR DYNAMICS TRIGGERED BY A FEW-CYCLE PULSE

by

SHUO ZENG

B.S., Sichuan University, China, 2008

AN ABSTRACT OF A DISSERTATION

submitted in partial fulfillment of the
requirements for the degree

DOCTOR OF PHILOSOPHY

Department of Physics
College of Arts and Sciences

KANSAS STATE UNIVERSITY
Manhattan, Kansas
2015

Abstract

In strong field physics, complex atomic and molecular motions can be triggered and steered by an ultrashort strong field. With a given pulse as an carrier-envelope form, $\mathcal{E}(t) = \mathcal{E}_0(t)\cos(\omega t + \varphi)$, we established our photon-phase formalism to decompose the solution of a time-dependent Schrödinger equation in terms of photons. This formalism is further implemented into a general analysis scheme that allows extract photon information direct from the numerical solution. The φ-dependence of any observables then can be understood universally as an interference effect of different photon channels. With this established, we choose the benchmark system H_2^+ to numerically study its response to an intense few-cycle pulse. This approach helps us identify electronic, rovibrational transitions in terms of photon channels, allowing one to discuss photons in the strong field phenomena quantitatively. Furthermore, the dissociation pathways are visualized in our numerical calculations, which help predicting the outcome of dissociation. Guided by this photon picture, we explored the dissociation in a linearly polarized pulse of longer wavelengths (compared to the 800 nm of standard Ti:Saphire laser). We successfully identified strong post-pulse alignment of the dissociative fragments and found out that such alignment exists even for heavy molecules. More significant spatial asymmetry is confirmed in the longer wavelength regime, because dissociation is no longer dominated by a single photon process and hence allowed for richer interference. Besides, quantitative comparison between theory and experiment have been conducted seeking beyond the qualitative features. The discrepancy caused by different experimental inputs allows us to examine the assumptions made in the experiment. We also extend numerical studies to the dissociative ionization of H_2 by modeling the ionization.

UNDERSTANDING DIATOMIC MOLECULAR DYNAMICS TRIGGERED BY A FEW-CYCLE PULSE

by

SHUO ZENG

B.S., Sichuan University, China, 2008

A DISSERTATION

submitted in partial fulfillment of the
requirements for the degree

DOCTOR OF PHILOSOPHY

Department of Physics
College of Arts and Sciences

KANSAS STATE UNIVERSITY
Manhattan, Kansas
2015

Approved by:

Major Professor
Brett D. Esry

Abstract

In strong field physics, complex atomic and molecular motions can be triggered and steered by an ultrashort strong field. With a given pulse as an carrier-envelope form, $\mathcal{E}(t) = \mathcal{E}_0(t)\cos(\omega t + \varphi)$, we established our photon-phase formalism to decompose the solution of a time-dependent Schrödinger equation in terms of photons. This formalism is further implemented into a general analysis scheme that allows extract photon information direct from the numerical solution. The φ-dependence of any observables then can be understood universally as an interference effect of different photon channels. With this established, we choose the benchmark system H_2^+ to numerically study its response to an intense few-cycle pulse. This approach helps us identify electronic, rovibrational transitions in terms of photon channels, allowing one to discuss photons in the strong field phenomena quantitatively. Furthermore, the dissociation pathways are visualized in our numerical calculations, which help predicting the outcome of dissociation. Guided by this photon picture, we explored the dissociation in a linearly polarized pulse of longer wavelengths (compared to the 800 nm of standard Ti:Saphire laser). We successfully identified strong post-pulse alignment of the dissociative fragments and found out that such alignment exists even for heavy molecules. More significant spatial asymmetry is confirmed in the longer wavelength regime, because dissociation is no longer dominated by a single photon process and hence allowed for richer interference. Besides, quantitative comparison between theory and experiment have been conducted seeking beyond the qualitative features. The discrepancy caused by different experimental inputs allows us to examine the assumptions made in the experiment. We also extend numerical studies to the dissociative ionization of H_2 by modeling the ionization.

Table of Contents

List of Figures

List of Tables

Acknowledgments

A doctoral degree in physics has been the most challenging task I have ever attempted. During these years, I have acquired not only extensive knowledge in physics, chemistry, math, computer science *etc*, but also unique life experience that shapes my mind profoundly and makes me the person today. Neither of these would have happened without countless help, guidance and encouragement from all people I have encountered over the years. This acknowledgement is dedicated to those individuals who influenced me enormously and helped me reach this stage.

It is an honor for me to learn and work with my advisor Dr. Brett D. Esry. His passion for physics has always been a source of inspiration for me to pursue my research. I have been constantly amazed by his encyclopedic knowledge and greatly benefited from it throughout these years. His meticulous and conscientious style in work has been permanently printed in my memory, and I am certain that this experience will be carried onto the next stage of my carrier. For that, I owe my deepest and heartiest gratitude to Brett. I am also grateful to my group colleagues, who works with me day in and day out, for making this bulk of work possible. My role model, Dr. Yujun Wang, has selflessly shared his invaluable experience with me in research, career planning and many other circumstances. Dr. Fatima Anis, Dr. Jesus Hernandez, Dr. Blake Laing and Dr. Jiangjun Hua offered me helpful guidance at the early stage of my research. A special thank goes to Dr. Christian Madsen, who helped me patiently in the absence of Brett during his sabbatical. It has been a great pleasure to work with other individuals, Dr. Gregary Armstrong, Yuliang Yu, Brandon Rigsbee, Dustin Ursery, Russ Averin. Everyone contributes a different character in the group, creating a diverse, dynamic and interesting environment that I always enjoyed.

I would also like to thank many of my collaborators. Many part of my work originated from the collaboration with Dr. Itzik Ben-Itzhak and his group. In particular, I would like to thank Dr. Kevin D. Carnes for patiently revising our paper, Dr. Mohammad A. Zohrabi

for explaining numerous experimental details to me. Meanwhile, I would like to express my gratitude to those collaborators in distance, Dr. Tim Rathje and Dr. A. Max Sayler in Friedrich Schiller University Jena, Germany, Dr. Nora Kling in Max-Planck-Institut, Germany, who shared data with us and had many discussions on the projects via dozens of long emails.

Additionally, I owe a thank to Dr. Chi-Dong Lin, Dr. Brian Washburn and Dr. Larry Weaver for their informative classes and discussions we had over the years. I am grateful to Larry Mcfeeter and PCSC for sparing us from computer technical difficulties from time to time.

Life would have been so boring without all the friends I made in Kansas, Moham-mad Zohrabi, Amy Ruinfar, Varun Makhija, Bachana Lomsadze, Youliang Yu, Xiaoming Ren, Sean McBride, Sachiko McBride, Chenchen Wang, Qi Zhang, Junliang Xu, Neda Dadashzadeh, Wes Erbsen, Tianlong Zu and many others. Thank you for creating so many interesting and memorable moments of my life.

Last but certainly not the least, I would not have come this far without the support from my family. I am forever indebted to my Mom and Dad to walk me through good and bad times. My aunt, Xiaoling, uncle Hejian and cousin Jiexi also enriched me with endless care throughout my stay in the united states. Thank you for everything.

Dedication

To my dear parents, Yali Hu and Xingmin Zeng

Chapter 1

Introduction

1.1 Atom and molecules in a strong field

Strong-field physics is built upon the fact that an external force can be used to manipulate the internal motion of an atom or molecule, inducing processes such as excitation, dissociation and ionization. To realize this, one first needs to generate a sufficiently intense field. In principle, one may produce such a strong field by focusing light sources, such as sunlight, into a small area. However, one would quickly realize that this attempt is bound to fail. Sunlight, which is the visible radiation from hot plasma in the sun, produces about 0.12 W/cm^2 intensity on the earth surface. To obtain some sense of how effective this field is on the microscopic level, recall that the electric field at the $1s$ orbital of electron inside of hydrogen atom in the Bohr-model is 1 a.u., or an intensity of 3.5×10^{16} W/cm^2 using a sinusoidal field. By this estimate, one would have to construct a concave mirror the size of Kansas and focus the sunlight into the area of one pixel in a computer screen in order to achieve equivalent intensity.

Fortunately, "light amplification by stimulated emission of radiation", namely the laser, provides an artificial light source that can be controlled in a much more feasible manner. The microscopic emissions in a laser system can be superposed constructively to form an instantaneous, strong field. Significant improvement has been made to generate more intense lasers in the recent few decades, which is largely attributed to the invention of the chirped

pulse amplification [3] and the self-mode-locked Ti:Sapphire laser system [4]. These emerged laser techniques have made it possible to generate an intense field comparable to the internal binding field inside atoms and molecules. It is not uncommon for contemporary research laboratories to generate a laser beam reaching up to the intensity of 10^{18} W/cm^2 [5, 6]. With the capability to generate an intense field, one can promote rich dynamics of atoms and molecules and many interesting phenomena in these regime have been discovered.

For atoms, an intense field can strip electrons from the core and the ionized electron were found to absorb an excess amount of photons during ionization and lead to multiple photon peaks in the ionization spectra, which was first discovered by Agostini in 1979 [7] and later referred to as the above-threshold ionization [8, 9]. The mechanism of atomic ionization is commonly characterized into two regimes, multiphoton and tunneling, which was originally proposed by Keldysh in the 1960s [10]. These two regimes are distinguished by the value of the so-called Keldysh parameter, the ratio of the binding energy of the atom and the ponderomotive energy of the ionized electron in the field. The continual development on the ionization mechanism was summarized by Popov in Ref. [11]. In an intense field, especially in the tunneling regime, the ionized electron can gain a significant amount of energy from the field and rescatter with the parent ions [12], leading to double ionization, recombination *etc.* One very important consequence of rescattering is the emission of harmonic radiation, which opens up an possibility for generating broad bandwidth attosecond pulses [13–15].

For molecules, an even richer variety of dynamics in the intense field can be explored. Early studies revealed the photodissociation of diatomic molecules by absorbing one photon as bond-softening, illustrated in H_2^+ [16]. Like above-threshold-ionization, molecules can also dissociate by absorbing excessive number of photons, leading to above-threshold dissociation [17, 18]. Besides dissociation, nuclear rotation is also studied extensively with the aid of laser pulse. An intense laser field can drive Raman transitions by exchanging angular momenta with the system. This brought about topics of the laser-induced molecular alignment and orientation [19, 20]. Recently, a sequence of pulses was used to align a

difluoroiodobenzene molecule in three-dimensions [21], making performing molecular frame measurements possible. Another broad class of applications of intense fields is the light-induced coherent control [22–24], which aims to drive a system to desired states, or in a practical point of view, control the final chemical products. To this end, many experimental techniques have been developed to explore this area, such as pump-probe scheme [25, 26], phase-tagging technique [27] and pulse shaping [28]. The control capability of laser pulse has extended to polyatomic systems, allowing one to manipulate torsion within the chemical compounds [29, 30] and control isomerization [31].

All of the topics mentioned above are merely the tip of the iceberg of the contemporary atomic, molecular and optical physics research. Being fully aware of the diversity of the atomic and molecular systems as well as the vast choices of intense laser tools, we are mostly interested in one specific subject, laser-induced phenomena by a few-cycle pulse. Such interest rises not only from the fact there have been wide-ranging discussions among the community over the years, which we will summarize in the next section, but also that we find that these phenomena can be understood universally.

1.2   General carrier-envelope phase effects

A few-cycle pulse can be described in a generic carrier-envelope form, $\mathcal{E}_0(t)\cos(\omega t + \varphi)$. The relative phase φ, the so called the carrier-envelope phase (CEP), provides a "knob" for controlling an intense field, triggering enormous scientific interest in its applications.

The CEP-stabilized intense laser developed in the late 90s [32, 33], allows researchers to study the phase dependence of observables. Such effects in strong field studies were first discovered experimentally in photoionization of noble gas atoms [34, 35], where photoelectrons were shown to be preferentially emitted in one direction. It was clearly demonstrated that this asymmetry is sensitive to the CEP of the pulse [36–39]. Theoretical studies were developed aiming to retrieve the CEP from the photoelectron spectra [40–43]. This led to the development of the phase-tagging technique that allows the CEP-sensitive measurements to

be performed more efficiently [27, 44–46]. Such strong CEP dependence in photoelectron dynamics is not unique to atoms, but is also found in molecules [47, 48] and nano-scale objects [49–51]. At the same time, the ionized electrons can be driven back to recombine with the parent ions and emit high harmonic radiation, which is frequently described with the three-step model introduced by Corkum [52], Kulander *et al.* [53], and later supported by Lewenstein *et al.* [54]. Based on this model, the kinetic energy of the rescattered electrons sensitively depends on the instantaneous waveform, which can be controlled by the CEP. The HHG spectrum will be modulated accordingly [55–62].

Similar CEP effects exist in the dissociation of molecules by a few-cycle pulse. It was firstly predicted by Roudnev *et al.* that HD^+ and H_2^+ can dissociate asymmetrically along the polarization direction controlled by the CEP [63]. Many theoretical calculations also revealed similar effects of few-cycle pulses on molecular systems [64–74]. The first experimental observation of the CEP-controlled spatial asymmetry was reported in the dissociative ionization of D_2 [75]. The subsequent measurements reaffirmed that one can vary the CEP to manipulate the spatial asymmetry of the fragments in the dissociative ionization of HD [76], CO [77–79], H_2 [80], DCl [81] and the photodissociation of H_2^+ [1, 2], among which the CEP-dependent total yields were also observed in Ref. [2, 78, 79, 82]. Recently, it has been demonstrated that CEP can be used to control different fragmentation channels of polyatomic molecules such as acetylene (C_2H_2), ethylene (C_2H_4), butadiene (C_2H_6) [83] and H_3^{2+} [84, 85]. At the same time, there has also been substantial effort to enhance the CEP effects by employing wavelengths longer than those of the Ti:Sapphire laser [67, 68, 86, 87].

Besides the traditional strong-field studies such as ionization and dissociation, CEP effects can be found ubiquitously in processes triggered by a few-cycle pulse. The CEP of a radio frequency few-cycle pulse was found effective to manipulate the ejection direction of electrons from a Rydberg atom [88], and to manipulate the population of the Zeeman sublevels of ground state Rb [89]. Lötstedt *et al.* demonstrated theoretically that the CEP can be used to control a nuclear reaction induced by an extreme field [90]. Further

applications of CEP effects in atomic and molecular processes can be found in the review collections [5, 8, 91, 92].

1.3 Goal of the study

It is not difficult to notice that CEP-related studies have permeated through the literature. Yet understanding various physical processes on a case-to-case basis can be challenging and overwhelming. In this thesis, we intend to extend our studies of CEP effects based on general framework [93], which will be explained in Chapter 2 and referred as photon-phase formalism throughout this thesis. We apply this formalism in our studies and consolidate the understanding of the physical phenomena induced by a few-cycle intense pulse. For multiple reasons, I choose the simplest molecule, H_2^+, as a numerical showcase to demonstrate phenomena induced by a few-cycle pulse. First, H_2^+ is comprised of only three charged particles, which allows us to solve the TDSE including vibration, rotation and excitation; second, its well-separated electronic structure in energy permits using only a handful of states to represent the electronic dynamics under certain limits, simplifying the physical picture; third, theory-experiment comparisons on this target can be conducted to seek quantitative agreement. Besides, all knowledge gained from this system can be naturally translated to other systems, since the photon-phase formalism is completely general. In this way, H_2^+ provides solid physical insights due to the fewer assumptions made as required for solving more complicated molecules, but the value of this dissertation will not be limited by the system chosen.

On the other hand, I also allocate part of this dissertation to focus on how to compare our full-dimensional TDSE calculation for H_2^+ to the experimental data with minimal physical approximation. This is extremely important because part of goal for studying a simple system such as H_2^+ is to conduct quantitative theory-experiment comparison, which is usually scarce in the studies of strong field phenomena.

1.4   Structure of the dissertation

In Chapter 2, I start with the characterization of a few-cycle pulse. By recognizing the underlying periodicity of the carrier-envelope phase in the Hamiltonian, we are able to derive a general formalism to build our intuition of strong-field phenomena in terms of the photon pathways. The photon interpretation is given in relation to the Floquet picture, and is exemplified by decomposing the photon structures in the above-threshold-ionization (ATI) [8] spectra from a hydrogen atom.

In Chapter 3, I lay out the details of our full-dimensional TDSE calculation for H_2^+ and the analysis within the context of the photon-phase formalism. The mathematical formulation of the problem provides the framework for the diatomic studies in the remainder of the dissertation.

In Chapter 4, the rotation of H_2^+ subjected to a strong field is studied extensively. Post-pulse alignment(PPA) is highlighted during photodissociation using a mid-infrared pulse, and its impact can be extended to heavy diatomic systems. This emphasizes the necessity of including rotation in photodissociation in order to evaluate the momentum distribution correctly, which plays an important role in studying the spatial asymmetry of the dissociative fragments in Chapters 5 – 7.

In Chapter 5, I discuss the CEP-controlled asymmetric dissociation of H_2^+ and the possibility of enhancing these CEP effects with longer wavelengths in comparison to the Ti:Sapphire laser.

In Chapter 6, I apply our theory to make quantitative comparisons with two recently reported experiments [1, 2]. The experimental data and calculations agree well, although some discrepancies highlight the need for including higher channels and using a realistic spectrum.

In Chapter 7, the dissociative ionization of H_2 is briefly covered with close relation to the studies of the molecular ions in the previous chapters. Through modeling of the ionization step, similar asymmetric dissociation is observed and the results are compared

with contemporary literature.

Chapter 2

Photon-phase formalism

2.1 Basic formalism

2.1.1 Periodicity of carrier-envelope phase and Fourier expansion

To demonstrate that this is a general approach to study the phenomena of atoms and molecules triggered by a few-cycle pulse, we start deriving our photon-phase formalism from the Schrödinger equation in a generic form. We follow the procedure outlined in Refs [64, 93]. An arbitrary system is governed by a time-independent Hamiltonian H_0 and the time-dependent field-matter interaction $V(t)$. We express the laser-matter interaction in the length gauge $V(t) = -\mathcal{E}(t) \cdot \mathbf{d}$ in terms of the instantaneous field and dipole operator, although it can be equivalently represented in any gauge. The instantaneous electric field of a few-cycle pulse takes the form

$$\mathcal{E}(t) = \mathcal{E}_0(t) \cos(\omega t + \varphi), \tag{2.1}$$

where $\mathcal{E}_0(t)$ is the envelope of the pulse, ω and φ are the center frequency and the carrier-envelope phase (CEP), respectively. The field can be alternatively defined in a more general form by the Fourier transform,

$$\mathcal{E}(t) = \int_{-\infty}^{\infty} \tilde{\mathcal{E}}(\omega') e^{i\omega' t + i\varphi} d\omega', \tag{2.2}$$

where $\tilde{\mathcal{E}}(\omega)$ is the complex amplitude of the Fourier-transform of the pulse, and then φ is merely a constant phase in the frequency domain. In either form, the key property

$\mathcal{E}(\varphi;t) = \mathcal{E}(\varphi + 2\pi;t)$ holds, hence the laser-matter interaction can be generically expressed as $V(\varphi;t)$ with a periodicity of 2π in φ in the TDSE,

$$\left[H_0 + V(\varphi;t)\right]\Psi(\varphi;t) = i\frac{\partial}{\partial t}\Psi(\varphi;t). \tag{2.3}$$

Since φ does not participate in the TDSE as a dynamical variable, it permits a Fourier expansion of the wavefunction:

$$\Psi(\varphi;t) = \sum_m \Psi_m(t)e^{im\varphi}, \tag{2.4}$$

where the expansion coefficients Ψ_m are independent of the CEP and all φ dependence can be analytically separated into the Fourier basis. These expansion coefficient Ψ_m can be arbitrarily multiplied a phase $\Psi_m(t) = \phi_m(t)e^{im\omega t}$ without changing its magnitude. We can substitute this expression combined with Eq. (2.4) into Eq (2.3), which leads to the CEP-Fourier equation,

$$(H_0 + m\omega)\phi_m(t) - \frac{1}{2}\mathcal{E}_0(t)\cdot\mathbf{d}\left[\phi_{m-1}(t) + \phi_{m+1}(t)\right] = i\frac{\partial}{\partial t}\phi_m(t). \tag{2.5}$$

Then only the envelope $\mathcal{E}_0(t)$ is involved in the equation. Consequently, each channel ϕ_m is governed by the Hamiltonian dressed by integer multiples of the photon energy ω, and coupled to its neighboring channels by the pulse envelope. We associate the quantum number m with net number of photons because Eq. (2.5) in the long pulse limit will reduce to the Floquet equation where photon is defined [64, 93], which will be seen more clearly in the remainder of this chapter. One can solve Eq. (2.5) for Ψ_m and evaluate the φ-dependent wavefunction $\Psi(\varphi;t)$ from Ψ_m by Eq. (2.4). Thus the parametric φ-dependence in the projection of the wave function on any eigenstate $|\Omega\rangle$ can be expressed explicitly as

$$|\langle\Omega|\Psi\rangle|^2 = \sum_m |\langle\Omega|\Psi_m\rangle|^2$$
$$+ \sum_{\substack{m,m' \\ m\neq m'}} \langle\Omega|\Psi_{m'}\rangle^*\langle\Omega|\Psi_m\rangle e^{i(m-m')\varphi}. \tag{2.6}$$

This expression gives an interpretation that the modulation of any observables caused by CEP can be considered as the interference of different photon channels, regardless of the physical system. This robust mathematical formalism combined with an intuitive physical picture provides a powerful tool for treating multiphoton processes induced by a few-cycle pulse.

2.1.2 Fourier analysis procedure

The CEP-Fourier equation (2.5) has its merits and drawbacks. This approach is particularly useful because it separates the CEP dependence from the wavefunctions analytically so that all effects caused by CEP can be understood universally. However, performing actual calculations based on this formalism is not particularly efficient for large problems. Even though a single CEP-Fourier calculation solves once for all CEPs, it introduces extra channels and the couplings in between. As a result, one calculation for the CEP-Fourier equation usually takes much longer than the original TDSE if many photon channels are occupied within the strong field.

With the exact periodic relation in Eq. (2.4), we can solve the regular TDSE with a set of different CEPs and then discrete Fourier transform the wave function $\Psi(\varphi_k; t)$ to obtain the photon information,

$$\Psi_m(t) = \frac{1}{N} \sum_{k=1}^{N} \Psi(\varphi_k; t) e^{-im\varphi_k}, \tag{2.7}$$

where N is the number of sampling points of φ. This normalization is chosen to ensure that Eq. (2.4) holds. The Fourier analysis approach is mathematically equivalent to solving the CEP-Fourier equation. However, performing the Fourier analysis does offer significant advantages over its counterpart. To solve the CEP-Fourier equation, one needs to ensure that the range of m in the calculation is sufficiently large in order to contain the wavefunction throughout the propagation. This usually means that the range of m is larger than the states are physically occupied. On the other hand, a regular TDSE calculation with a definite CEP does not have this truncation error and thus preserves all photon information. Instead,

truncation errors for this Fourier analysis approach only come sampling from a finite set of CEPs in the Fourier transform. By sampling equally-spaced CEPs for the transform in Eq. (2.7), one can resolve only N distinct frequencies with N CEPs points, which typically means one can obtain at most N photon channels. However, given the condition that the wavefunction is exactly periodic $\Psi(\varphi; t) = \Psi(\varphi + 2\pi; t)$, one can derive the error from the Fourier transform by Eq. (2.7) for the mth channel analytically as [94]

$$\Delta\Psi_m = \sum_{q=1}^{\infty}(\Psi_{m-qN} + \Psi_{m+qN}). \tag{2.8}$$

From the expression above, the sampling error for Ψ_m is physically contributed by the photon channels that are $\pm N$, $\pm 2N$, ... photons apart. This offers a significant advantage of using "photon" as a physical argument to estimate errors. To make it more concrete, it is more helpful to project Eq. (2.8) onto a field-free energy basis,

$$\langle E|\Delta\Psi_m\rangle = \sum_{q=1}^{\infty}\Big(\langle E|\Psi_{m-qN}\rangle + \langle E|\Psi_{m+qN}\rangle\Big). \tag{2.9}$$

For example, if 4 CEP points are used for the transform in Eq (2.7), there are only 4 unique Ψ_m for m ranging from $-\infty$ to ∞, whereas Ψ_m, $\Psi_{m\pm4}$, $\Psi_{m\pm8}$ ... are identical. However, since the error to $\langle E|\Delta\Psi_m\rangle$ is only contributed by the physical photon channels that are 4 photons apart, the actual error from sampling is expected to be exponentially small in the energy region where m-photon process dominates.

Therefore, in terms of observables, the CEP points needed for extracting photon channels can be much smaller than the number of the occupied photon channels. This will be illustrated with photoionization of hydrogen atom in Sec. 2.2. Unlike solving the CEP-Fourier equation in the truncated photon blocks, the errors in the Fourier analysis do not affect the time propagation. Furthermore, in terms of computation, breaking one CEP-Fourier calculation into several independent regular TDSE calculations is convenient to compute in parallel.

Recognizing this general periodic φ-dependence not only helps build this photon-phase formalism, but it can also minimize the repetitive averaging step when one intends to eval-

uate a CEP-averaged observable. For example, in Ref. [95], calculations with 12 different CEP values were performed in order to evaluate the photoelectron spectra of hydrogen atom, in which, according to our formalism, only three to four CEPs are needed to extract same amount of information since we do not expect large overlap of many photon channels in energy given the 6.3-fs 760-nm pulse in Ref. [95].

2.1.3   Relation to Floquet

Equation (2.5) appears to be very similar to the conventional Floquet approach for treating a system in a periodic field. The standard Floquet method [96] takes advantage of the periodicity of the Hamiltonian in time in the continuous-wave laser field, $V(t) = V(t + T)$ and $T = 2\pi/\omega$, and applies the Floquet theorem to solve $\left[H_0 + V(t)\right]\Psi(t) = i\partial_t\Psi(t)$. Mathematically, the theorem allows one to separate the non-periodic component of the wavefunction from the periodic part by introducing the quasienergy ε,

$$\Psi(t) = e^{-i\varepsilon t}\sum_m \Phi_m e^{im\omega t}, \tag{2.10}$$

where Φ_m is time-independent. Therefore, the time-dependent problem can be solved equivalently as a multi-channel eigenvalue problem:

$$\sum_m \left(H_{m'm} + \delta_{m'm}m\omega\right)\Phi_m = \varepsilon\Phi_{m'}, \tag{2.11}$$

where

$$H_{m'm} = \frac{1}{T}\int_0^T e^{-im'\omega t}\left[H_0 + V(t)\right]e^{im\omega t}dt. \tag{2.12}$$

More importantly, the relation between this individual term of the expansion, referred to as the Floquet or field-dressed states, to the number of photon states in the quantized field picture was first recognized in Ref [97]. This provides one way to understand physical processes in terms of photons despite the fact the field is not inherently quantized in our Schrödinger equation. Notice that if the interaction is given the length gauge form $V(t) =$

12

$-\mathcal{E}_0 \cos(\omega t) \cdot \mathbf{d}$, Eq. (2.11) becomes

$$(H_0 + m\omega)\Phi_m - \frac{1}{2}\mathcal{E}_0 \cdot \mathbf{d}\Big[\Phi_{m-1} + \Phi_{m+1}\Big] = \varepsilon\Phi_m. \qquad (2.13)$$

The expression above is equivalent to Eq. (2.5) in the long pulse limit, which identifies the individual terms in Eq. (2.5), $\Psi_m(t)$, as photon channels.

As pulsed lasers move away from the monochromatic limit in order to study molecular and electronic dynamics on short time scales, it becomes troublesome to apply the standard Floquet approaches because the basic assumption of a time-periodic Hamiltonian no longer holds. Generalizations such as the adiabatic Floquet approach [98, 99] or two-time operator [100], need to be made in order to apply the Floquet theorem in the non-periodic field.

Our photon-phase formalism does not rely on the Floquet theorem but only the periodicity of CEP. Therefore, the expansion in Eq. (2.4) is not limited by the pulse duration. Even in the few-cycle regime, our formalism still offers a mathematically exact decomposition of the wave function, so that we can understand physical problems in terms of "photons", while the photon energy has a bandwidth determined by the pulse envelope.

2.2   Hydrogen ionization in a strong field

To give an example, we apply our method to explain a well-known phenomenon, above threshold ionization (ATI) [7, 9] from a hydrogen atom, where an electron absorbs photons in excess of the minimum number required for ionization, and exhibits multiple peaks in the photoelectron spectrum separated by the photon energy.

2.2.1   Photon-decomposed ATI spectrum

A $1s$ state hydrogen is exposed to a 5 fs linearly polarized pulse with a central angular frequency $\omega = 0.165$ a.u., corresponding to 4.5 eV in energy. A finite-difference scheme [101] is applied to solve the three-dimensional hydrogen problem with a spherical harmonic expansion for the angular dependence. The numerical code is adapted from an existing $3D$
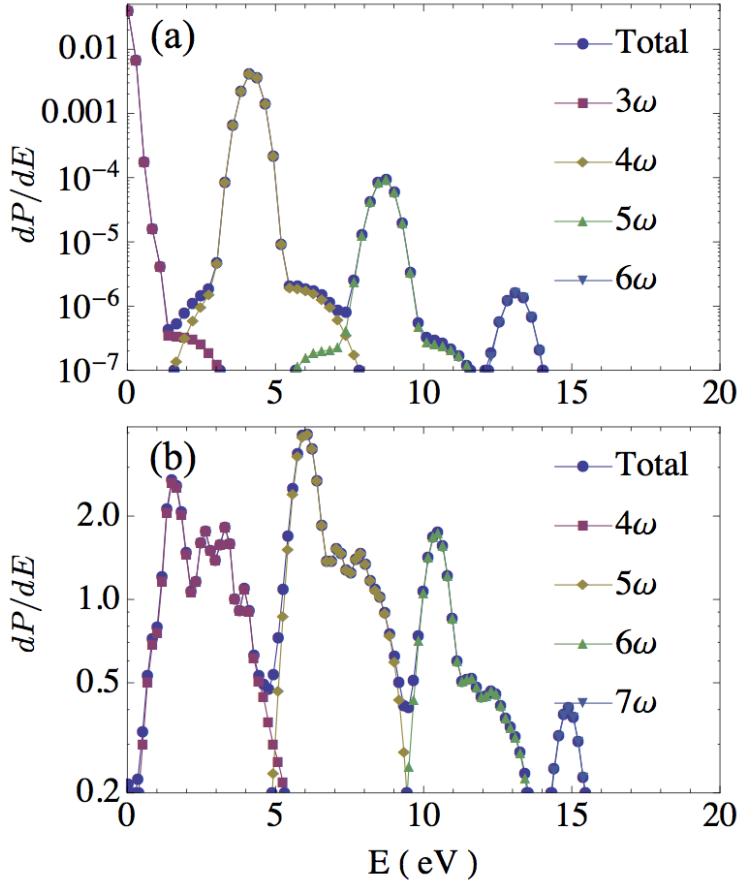
Figure 2.1: *Hydrogen atom total ATI spectra and its individual photon channels from Fourier analysis. The laser parameters are $\omega = 4.5$ eV for both calculations and (a) $\tau_{\text{FWHM}} = 5$ fs, $I_0 = 2.0 \times 10^{13}$ W/cm^2 (b) $\tau_{\text{FWHM}} = 5$ fs, $I_0 = 4.0 \times 10^{14}$ W/cm^2. The total spectrum is chosen to be the calculation with $\varphi = 0$. The individual photon channels are extracted from 5 sets of calculations with equally spaced CEPs.*

code for solving TDSE in full dimensionality for H_2^+ [102]. We will skip the mathematical formulation and refer to the similar treatment for H_2^+ in Chapter 3. The observable of particular interest here is the kinetic energy spectrum of the photoelectron. The differential spectrum with respect to energy is converged to about 2 digits across the energy range shown in Fig. 2.1. To decompose the photon channel contribution, we performed 5 calculations with different φ that are equally spaced in the range from 0 to 2π. Performing discrete-Fourier-transform on these sets of wavefunctions yields the photon channels.

The decomposed photon contribution is plotted along with the total ATI spectrum as a comparison. In Fig. 2.1(a), the spectrum reveals well-separated peak structures in logarithmic scale with a spacing of 4.5 eV. As the intensity is increased to 4×10^{14} W/cm^2 in Fig. 2.1(b), the ionization yield grows substantially and more complex structures appear. Nevertheless, the dominant peaks separated by the photon energy are still recognizable.

It is very important to notice that, even for a pulse duration as long as 7 cycles, where CEP effects are expected to be small, our analysis still holds as long as the sampling points are sufficient to extract high-frequency φ-components. Therefore, Fourier analysis can be applied to analyze physical processes involving of thousands of photons such as microwave interaction with Rydberg states [88]. It is the periodicity of the CEP in the Hamiltonian which allows us to employ the analysis in a wide range of problems.

2.2.2 Intensity-dependent shift

Another well-known feature observed in Fig. 2.1 is the ponderomotive shift. Electrons absorb an excessive number of photons from the field and get ionized. In the presence of a strong field, the ionized electron quivers with the field, which requires additional energy for the quivering motion. This quivering motion will diminish as the field fades away, thus the kinetic energy of such motion, the ponderomotive energy U_p, does not contribute to the final kinetic energy of the electron. Therefore, the position of the m-photon ATI peak will be shifted by $U_p = \mathcal{E}_0^2/(4\omega^2)$, defined as the cycle-averaged kinetic energy of the electron,

$$E_m = m\omega - I_p - U_p \tag{2.14}$$

where I_p is the binding energy of the electron. It suggests, for example, that the 4ω peak should be at 4.2 eV and 1.5 eV for 3×10^{13} W/cm^2 and 4×10^{14} W/cm^2, respectively. In Fig. 2.1(a) and 2.1(b), the most prominent photon peaks are located at the designated positions.

Given the simple assumption of the Hamiltonian being a periodic function of CEP, our photon-phase formalism in interpreting observables can be applied it in more complex

physical problems where photon signatures are no longer obvious in observables. This will apply in detail in the H_2^+ study in the next chapter.

2.3 Summary

In this chapter, we present a general analysis scheme for the solutions of a TDSE in order to extract photon channels. This analysis is constructed based on the periodicity of the carrier-envelope phase of the electric field instead of time, which is completely independent of the system itself. This analysis allows one to extract the photon information from several independent calculations directly, instead of solving the CEP-Fourier equation, as a result saving computation time. We demonstrate the strengths of the analysis method in an example of hydrogen ionization in a strong field. We show that the analysis can reproduce the photon features that are consistent with the current knowledge of the ionization process.

Chapter 3

Full-dimensional H_2^+ TDSE

3.1 Coupled-channel equation

We solve the time-dependent Schrödinger equation within the Born-Oppenheimer (BO) representation. In particular, we include all nuclear degrees of freedom and allow for electronic excitation to higher manifolds. However, since including ionization within the BO representation is highly nontrivial—and a full-dimensional treatment of H_2^+ without the BO representation is not currently tractable—we will neglect ionization. Consequently, to ensure that our calculations still accurately reflect reality, we will limit the intensities we consider to those at which ionization is negligible.

We obtain the electronic states Φ for the BO representation by solving the field-free adiabatic equation in the body frame using prolate spheroidal coordinates ξ and η [103]:

$$H_{\mathrm{ad}}\Phi_{n\Lambda\sigma_z}(R;\xi,\eta) = U_{n\Lambda\sigma_z}(R)\Phi_{n\Lambda\sigma_z}(R;\xi,\eta). \tag{3.1}$$

In this expression, R is the internuclear distance, H_{ad} is the fixed-R Hamiltonian, n is the separated-atom principal quantum number, Λ is the absolute value of the projection of the electronic orbital angular momentum onto the internuclear axis, and σ_z is the reflection of the electronic coordinates with respect to the $z = 0$ plane in the body frame. Note that the usual gerade and ungerade symmetries correspond to positive and negative values of $(-1)^\Lambda \sigma_z$, respectively. The potentials $U_{n\Lambda\sigma_z}(R)$ are illustrated in Fig. 3.1.

17
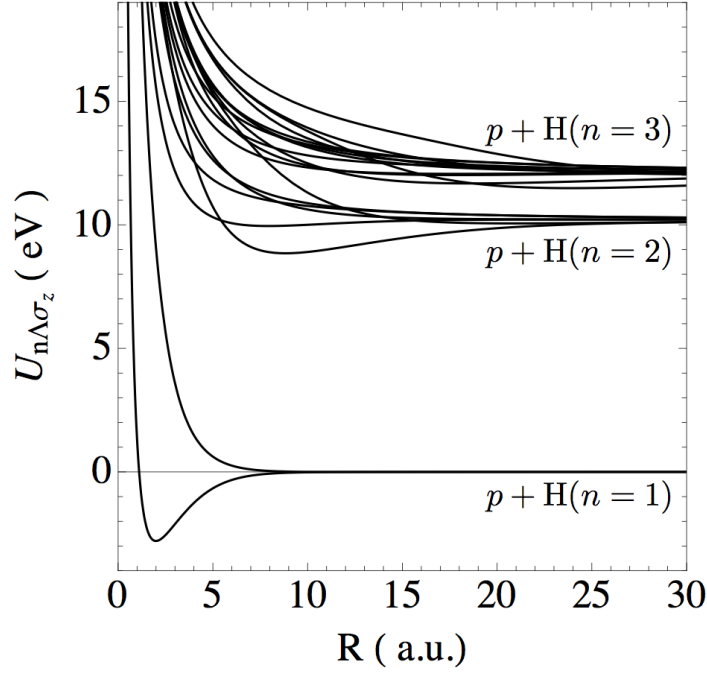
Figure 3.1: *Potentials curves for* H_2^+ *up to* $n = 3$ *manifold.*

The total wave function can thus be written in the laboratory frame as

$$\Psi(\mathbf{R}, \mathbf{r}, t) = \sum_{\beta J M} \frac{F_{\beta J M}(R, t)}{R} \Omega_{M\Lambda}^{J\pi}(\theta, \phi, \chi) \Phi_\beta(R; \xi, \eta), \tag{3.2}$$

including the nuclear rotation via the symmetrized symmetric top wave function $\Omega_{M\Lambda}^{J\pi}$ [103, 104]. Its arguments are the Euler angles—the first two of which, θ and ϕ, are the spherical polar angles of the internuclear vector and χ is the azimuthal angle of the electron in the body frame. Besides Λ, the indices of Ω are the total orbital angular momentum J, its projection M on the laboratory-frame z axis, and the total parity π. The index β collectively represents all indices other than J and M.

In the length gauge, the time-dependent Schrödinger equation is (atomic units are used throughout)

$$i\frac{\partial}{\partial t}\Psi = \left(-\frac{1}{2\mu}\nabla_R^2 + H_{\text{ad}} - \boldsymbol{\mathcal{E}}(t) \cdot \mathbf{d}\right)\Psi \tag{3.3}$$

with μ the reduced mass of the nuclei, $\mathbf{d}$ the system's dipole moment operator, and $\boldsymbol{\mathcal{E}}$ the

laser's electric field. Explicitly,

$$\boldsymbol{\mathcal{E}}(t) = \mathcal{E}_0 e^{-t^2/\tau^2} \cos(\omega t + \varphi)\,\hat{\mathbf{z}} \tag{3.4}$$

in which ω is the carrier frequency, φ is the CEP, and $\mathcal{E}_0$ is the peak electric field. The pulse length τ is related to the full-width-half-maximum of the pulse intensity τ_{FWHM} by $\tau = \tau_{\text{FWHM}}/\sqrt{2\log 2}$. We will use this analytical form to characterize the laser pulse in the calculations throughout this dissertation unless stated otherwise explicitly.

Substituting Ψ from Eq. (3.2) into Eq. (3.3) and integrating out the electronic and angular coordinates yields the coupled nuclear equations that we propagate:

$$i\frac{\partial}{\partial t}F_{\beta JM} = \left(-\frac{1}{2\mu}\frac{\partial^2}{\partial R^2} + \frac{J(J+1) - \Lambda^2}{2\mu R^2} + U_\beta\right)F_{\beta JM}$$
$$-\sum_{\beta' J'}\langle\Phi_\beta\Omega_{M\Lambda}^{J\pi}|\boldsymbol{\mathcal{E}}(t)\cdot\mathbf{d}|\Phi_{\beta'}\Omega_{M\Lambda'}^{J'\pi'}\rangle F_{\beta' J' M} \tag{3.5}$$

We take the initial condition in all cases presented here to be $J{=}0$ and $M{=}0$, although we consider various initial vibrational states. Since the laser field is linearly polarized and M is initially zero, we simplified the notation in Eq. (3.5) to exclude a sum over M. Additionally, we have neglected both the Coriolis and non-Born-Oppenheimer coupling terms. However, since we purposefully limit the maximum intensity to keep the excitation of the $n{=}2$ manifold—and thus hopefully ionization as well—small, including only the $1s\sigma_g$ and $2p\sigma_u$ channels is a very good approximation. With only these two channels, both the Coriolis and non-Born-Oppenheimer coupling are zero, making our treatment essentially exact within this electronic subspace. The remainder of our analysis and discussion will thus be limited to this subspace unless explicitly mentioned otherwise.

3.2   Numerical details

The R-dependence in Eq. (3.5) is discretized using a generalized finite difference method [101, 105, 106] with the distribution of points in R chosen according to the local wavelength in the lowest electronic channel $1s\sigma_g$. We choose the highest energy to be 0.15 a.u. above the

thresholds so that the oscillation of the wave function below this energy should be well represented in our radial grid. The choice of convergence parameters such as grid density, time step and box size vary according to the goals of the projects. We refer to these numerical details in Appendix B.

We use a split-operator scheme to evaluate the short-time propagator, separating the R- and J-dependent terms in the exponential [102]. The propagation is thus effected by successive applications of one-dimensional propagators in R and J, respectively. These propagators are evaluated using the Crank-Nicolson method (a Padé approximation to the exponential short-time evolution operator).

Since we inherently neglect ionization in our formalism, we have to try to ensure this process is not important in our calculations. For example, in all calculations presented in Chapters 4 and 5, we believe ionization to be negligibly small at the given intensities ($\leq 10^{14}$ W/cm^2) because a calculation including the $n = 2$ manifold of states showed that their contribution to dissociation was never more than 2% at any time during the pulse for $v = 6$; the final dissociation probability is typically much smaller. For higher initial vibrational states, the $n = 2$ population may reach up to 5%, but these contributions will be suppressed when the initial Franck-Condon vibrational distribution is considered in Sec. 5.1.3. Based on the argument that ionization should be smaller than excitation, we thus believe that we can reasonably neglect ionization. While the excited manifolds are not a perfect surrogate for ionization, they provide the best indication of ionization available. As a consequence of the small $n = 2$ population, we can further restrict our calculation to the lowest two channels to a very good approximation at all but the highest intensities, simplifying the calculations considerably. This approximation was used in the calculations presented in Chapters 4 and 5 since the intensity used is below 10^{14} W/cm^2, while we included the $n = 2$ manifold in the calculations shown in Chapters 6 and 7 as a way to gauge the errors from neglecting ionization at very high intensities.

As required by Maxwell's equations, the DC component of the pulse has to be zero, we

therefore must choose the starting and ending point of the time propagation to satisfy this condition. For example, for the calculations using the Gaussian pulse described by Eq. (3.4), the times were chosen such that the intensity of the envelope reaches 10^7 W/cm² . This choice for $t_{\min}$ and $t_{\max}$ produces a DC impulse—i.e., $\int_{t_{\min}}^{t_{\max}} \mathcal{E}(t)dt$—ranging from 0.00044 a.u. to 0.0012 a.u. across the intensities and frequencies considered in Chapters 4 and 5.

We must also verify that a sufficient number of partial waves have been included to achieve convergence. To be more specific, a 2000-nm calculation for $I = 10^{14}$ W/cm² and $\tau_{\text{FWHM}} = 3$ cycles populates up to 74 partial waves with the probability of highest partial wave being 10^{-7} during the propagation.

We have chosen all of these parameters such that the total dissociation probabilities are converged to 3 digits within the $1s\sigma_g$-$2p\sigma_u$ subspace (recall that the higher n contribute at most in the second digit). We thus expect the differential quantities discussed below to be converged to be at least 2 digits in the region we are interested.

3.3   Extracting observables

The most differential observable we can calculate in the present case is the relative momentum distribution of the nuclei. Every other observable of interest can be calculated from it. The momentum distribution is obtained by projecting the final wave function onto the energy-normalized, incoming-wave scattering state $\Psi_{\mathbf{K},1s}^{(-)}$ with the H atom in the $1s$ state [69, 107]:

$$\frac{\partial^2 P}{\partial E \partial \theta_K} = \int \left| \langle \mathbf{K}, 1s | \Psi(t_f) \rangle \right|^2 d\phi_K$$
$$= 2\pi \left| \sum_{J \text{ even}} C_{Jg} Y_{J0}(\theta_K) + \sum_{J \text{ odd}} C_{Ju} Y_{J0}(\theta_K) \right|^2 . \tag{3.6}$$

In this expression,

$$C_{Jp} = (-i)^J e^{-i\delta_{Jp}} \langle EJp | F_{pJ}(t_f) \rangle \tag{3.7}$$

with $(p = g, u)$ since β reduces to p when restricted to the $n{=}1$ manifold; $\mathbf{K}$ represents the relative momentum between H and p; and θ_K is the angle between $\mathbf{K}$ and the polarization

21

direction $\hat{\mathbf{z}}$. The state $|EJp\rangle$ is the energy-normalized scattering state with standing-wave boundary conditions. Asymptotically, $\Psi_{\mathbf{K},1s}^{(-)}$ reduces to a direct product of a plane wave for the nuclei and a $1s$ atomic orbital for the electron on one of the nuclei (which nucleus cannot be determined since they are identical).

To characterize the CEP effects, we will use what has become the standard parameter—the normalized asymmetry:

$$\mathcal{A}(E) = \left(\frac{dP_{\text{up}}}{dE} - \frac{dP_{\text{down}}}{dE} \right) \bigg/ \left(\frac{dP_{\text{up}}}{dE} + \frac{dP_{\text{down}}}{dE} + \Delta \right) \tag{3.8}$$

where Δ is a cut-off parameter that prevents uninteresting enhancement of $\mathcal{A}(E)$ by small yields. We will set Δ to be 1% of the maximum yield evaluated from the individual initial states, reflecting, in part, the numerical accuracy we expect (see Sec. 3.2). The up and down probabilities are obtained by integrating over the upper and lower hemispheres (in the lab frame),

$$\begin{aligned}
\frac{dP_{\text{up}}}{dE} &= \int_0^{\pi/2} \frac{\partial^2 P}{\partial E \partial \theta_K} \sin \theta_K d\theta_K, \\
\frac{dP_{\text{down}}}{dE} &= \int_{\pi/2}^{\pi} \frac{\partial^2 P}{\partial E \partial \theta_K} \sin \theta_K d\theta_K.
\end{aligned} \tag{3.9}$$

The details of the derivation can be found in Ref. [107].

3.4   Interpreting the results

To understand the observables we calculate, we will employ the photon-phase representation we introduced in Chapter. 2. This exact representation takes advantage of the fact that the Hamiltonian—and thus Ψ—depends periodically on φ. One may thus write Ψ as a Fourier series

$$\Psi(\varphi; t) = \sum_{m=-\infty}^{\infty} e^{im\varphi} \psi_m(t) \tag{3.10}$$

where the index m is interpreted as the *net* number of photons exchanged with the field [64, 93].

Combining Eq. (3.10) with $\psi_m = e^{im\omega t}\phi_m$, Eq. (3.2), and Eq. (3.5)—i.e., replacing $F_{\beta JM}$ from Eq. (3.2) by $\sum F_{m\beta JM}e^{im\omega t}$—gives

$$
i\frac{\partial}{\partial t}F_{m\beta J} = \left(-\frac{1}{2\mu}\frac{\partial^2}{\partial R^2} + \frac{J(J+1)}{2\mu R^2} + U_\beta + m\omega\right)F_{m\beta J}
$$
$$
-\frac{1}{2}\sum_{\beta' J'}\langle\Phi_\beta\Omega_{00}^{J\pi}|\boldsymbol{\mathcal{E}}_0(t)\cdot\mathbf{d}|\Phi_{\beta'}\Omega_{00}^{J'\pi'}\rangle\left(F_{m-1\beta'J'} + F_{m+1\beta'J'}\right) \quad (3.11)
$$

where $\boldsymbol{\mathcal{E}}_0(t)$ is the pulse envelope from Eq. (3.4) and we have dropped the M label since $M = 0$ in all of our calculations. Being coupled equations in m, however, the computational demands of original problem get multiplied by the number of photon blocks needed for convergence. Although the calculation needs only to be done once, its increased demand is usually prohibitive. As we introduced in Chapter 2, we can solve the original TDSE for Ψ at several φ and Fourier transform the results to obtain ψ_m for interpretation.

In the photon-phase representation, Eq. (3.6) becomes

$$
\frac{\partial^2 P}{\partial E \partial\theta_K} = 2\pi\Bigg|\sum_{Jm\text{ even}} C_{mJg}Y_{J0}(\theta_K)e^{im\varphi}
$$
$$
+ \sum_{Jm\text{ odd}} C_{mJu}Y_{J0}(\theta_K)e^{im\varphi}\Bigg|^2. \quad (3.12)
$$

with

$$
C_{mJp} = (-i)^J e^{-i\delta_{Jp}}\langle EJp|F_{mpJ}(t_f)\rangle. \quad (3.13)
$$

In Eq. (3.12), we have used the fact that the initial $J = 0$ state has even parity to limit the sums over m according to the dipole selection rules. The quantities needed for the normalized spatial asymmetry $\mathcal{A}$ are then the differential asymmetry

$$
\left.\frac{\partial^2 P}{\partial E \partial\theta_K}\right|_{\text{up}} - \left.\frac{\partial^2 P}{\partial E \partial\theta_K}\right|_{\text{down}} = 8\pi\text{Re}\sum_{\substack{Jm\text{ even}\\J'm'\text{ odd}}} C^*_{m'J'u}C_{mJg}Y_{J'0}(\theta_K)Y_{J0}(\theta_K)e^{i(m-m')\varphi} \quad (3.14)
$$

and the differential total yield

$$
\left.\frac{\partial^2 P}{\partial E \partial\theta_K}\right|_{\text{up}} + \left.\frac{\partial^2 P}{\partial E \partial\theta_K}\right|_{\text{down}} = 4\pi\text{Re}\sum_{\substack{Jm\text{ even}\\J'm'\text{ even}}} C^*_{m'J'g}C_{mJg}Y_{J'0}(\theta_K)Y_{J0}(\theta_K)e^{i(m-m')\varphi}
$$
$$
+ 4\pi\text{Re}\sum_{\substack{Jm\text{ odd}\\J'm'\text{ odd}}} C^*_{m'J'u}C_{mJu}Y_{J'0}(\theta_K)Y_{J0}(\theta_K)e^{i(m-m')\varphi}. \quad (3.15)
$$

23

"Up" and "down" in these expressions refer to angles θ_K and $\pi - \theta_K$, respectively, with the consequence that the expressions should only be evaluated over one hemisphere or the other. Moreover, from Eqs. (3.14) and (3.15), we can see, for instance, that the asymmetry involves only $m - m' = $ odd; and the yield, only $m - m' = $ even. The allowed frequencies in φ are thus determined.

The total KER spectrum can be obtained from Eq. (3.12) by integrating over angles, giving

$$\frac{dP}{dE} = \text{Re} \sum_{Jmm' \text{ even}} C^*_{m'Jg} C_{mJg} e^{i(m-m')\varphi}$$
$$+ \text{Re} \sum_{Jmm' \text{ odd}} C^*_{m'Ju} C_{mJu} e^{i(m-m')\varphi}. \tag{3.16}$$

Like the angle-differential expression in Eq. (3.15), only even frequencies in φ are possible in the total KER spectrum.

3.5 Summary

In this section, we described the mathematical formulation used to solve the full-dimensional H_2^+ in a linearly polarized pulse within the BO representation. Observables such as differential momentum distribution, KER spectra and spatial asymmetry were written explicitly in this chapter. Additionally, we applied our photon-phase formalism introduced in Chapter 2 and separated the carrier-envelope phase dependence of these observables analytically in terms of the *net* photon channels.

Chapter 4

Rovibrational motion in the strong field

4.1 Importance of the nuclear rotation

Nuclear rotation can be treated in a fairly straightforward manner if the system is vibrationally cold. In this case, rotational phenomena, such as laser-induced alignment and orientation [19, 20, 104, 108–116], can be described by the well-known rigid-rotor model [117]. In this model, it is common to consider nuclear rotation as the interference of different rotational states. The splitting between the neighboring rotational states is typically on the order of 10^{-4} eV, which gives rise to a characteristic time-scale of picosecond. As for dissociative processes in the intense laser field, the radial kinetic energy is usually on the order of eV. Given the four order of magnitude difference in nuclear rotational energy and the radial kinetic energy, nuclear rotation is commonly neglected.

However, such argument based on time-scale does not always hold in the laser-induced dissociation processes. Even though a typical rotational period is on the order of picosecond, this time scales inversely with nuclear mass, which makes rotation much more significant for small molecules such as H_2^+. More importantly, the rotational energy grows quadratically with the total angular momentum J. Given an intense field, the system can be promoted to very high rotational states such that rotational energy is no longer negligible compared to radial kinetic energy. Despite that many studies pointed out that the rotation of this system
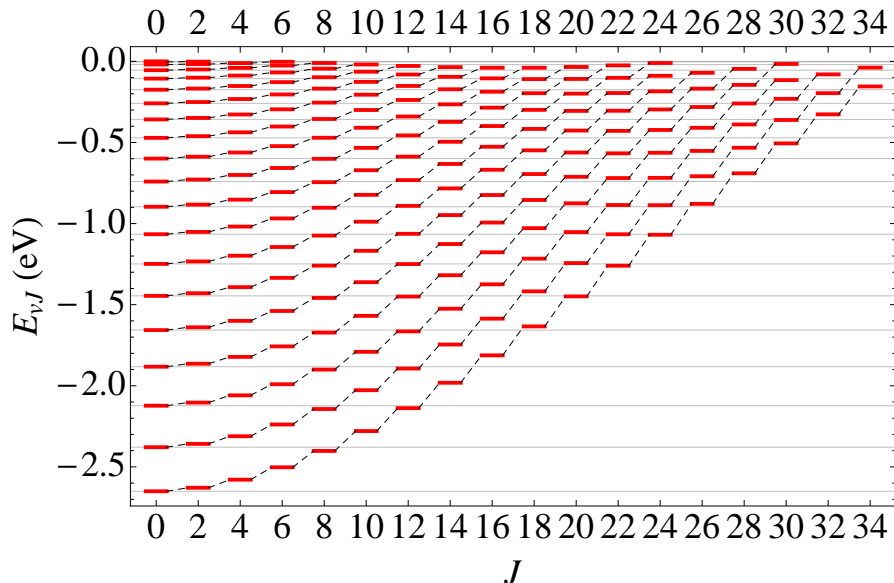
Figure 4.1: *The rovibrational energy levels diagram of the H_2^+ lowest electronic state, $1s\sigma_g$. The dashed lines link the rovibrational states associated to the same vibration index in different rotational states.*

may lead to below-threshold-dissociation [118, 119], zero-photon-dissociation [119, 120] and alignment of fragmentation [102, 118, 121–123], treating H_2^+ in restricted dimension [124, 125] is still a favorable approach due to its simplicity.

4.2 Raman transition in photodissociation of the H_2^+

Raman transition ubiquitously exists and play a very important role in the dissociation of the H_2^+ by an intense laser field. The external field exchanges angular momenta with the system and promote rotational states. It is very intuitive to consider these transitions in terms of the field-free rovibrational states of H_2^+ as illustrated in Fig. 4.1. Given the small mass of H_2^+, the energy levels of bound states are lifted significantly as J progresses due to the rising centrifugal barrier. The system makes a transition in between these states by absorbing and emitting one photon. In the presence of a linearly polarized light, this Raman transition takes place according the selection rule $J \to J, J \pm 2$. Due to the two-photon nature of the Raman process, the system can make transitions by exchanging photons with

the field inelastically. This energy difference is limited by the finite bandwidth of a laser pulse. Therefore, even though the selection rules have no restriction on the vibrational index, the system makes transitions much more efficiently in between the rovibrational states that are energetically close. Sequences of Raman transitions can produce a widespread rotational distribution, which consequently contributes to the rotation.

An example is given in Fig. 4.2 where the rovibrational distributions after the pulse are shown. Three pulses with identical pulse envelopes but different center wavelengths — 800 nm, 1200 nm and 1600 nm—are chosen to interact with an initial state $v = 6$ at $J = 0$. The rovibrational distribution of the bound states show very similar features in Fig. 4.2(a), (c) and (e). The wave functions for three cases are mostly localized in $v = 6$ of the first few rotational states, $J = 0, 2$ and 4. Given the bandwidth of these three pulses are 0.16 eV, while the vibrational spacings near $v = 6$ is about 0.2 eV, the pulse does not promote transitions between different v very efficiently. However, as J increases, the $E_{vJ} \rightarrow E_{v,J\pm2}$ are not longer energetically the closest, hence Raman transitions tend to populate states with different vibrational indices. As a result, the vibrational distributions in higher Js spread out.

The physical processes become more complicated when dissociation is also involved. Figure 4.2 (b) (d) and (f) show much stronger wavelength dependence in the continuum states. For 800 nm, the dissociation occurs mostly via *net* one photon, therefore the odd Js are occupied. On the other hand, 1200 nm dissociates mostly via *net* two photons hence the even J channels are occupied. For even longer wavelength, both even and odd J states are populated in Fig. 4.2(c). Even though H_2^+ does not require many photons to dissociate energetically, the dissociative wave functions usually exhibit wide distribution in J, indicating multiphoton processes. At this point, Fig. 4.2 demonstrates how significant the Raman transitions are in the study of H_2^+ interacting with a few-cycle pulse. We will discuss the consequences of such Raman transitions in the rest of this chapter.
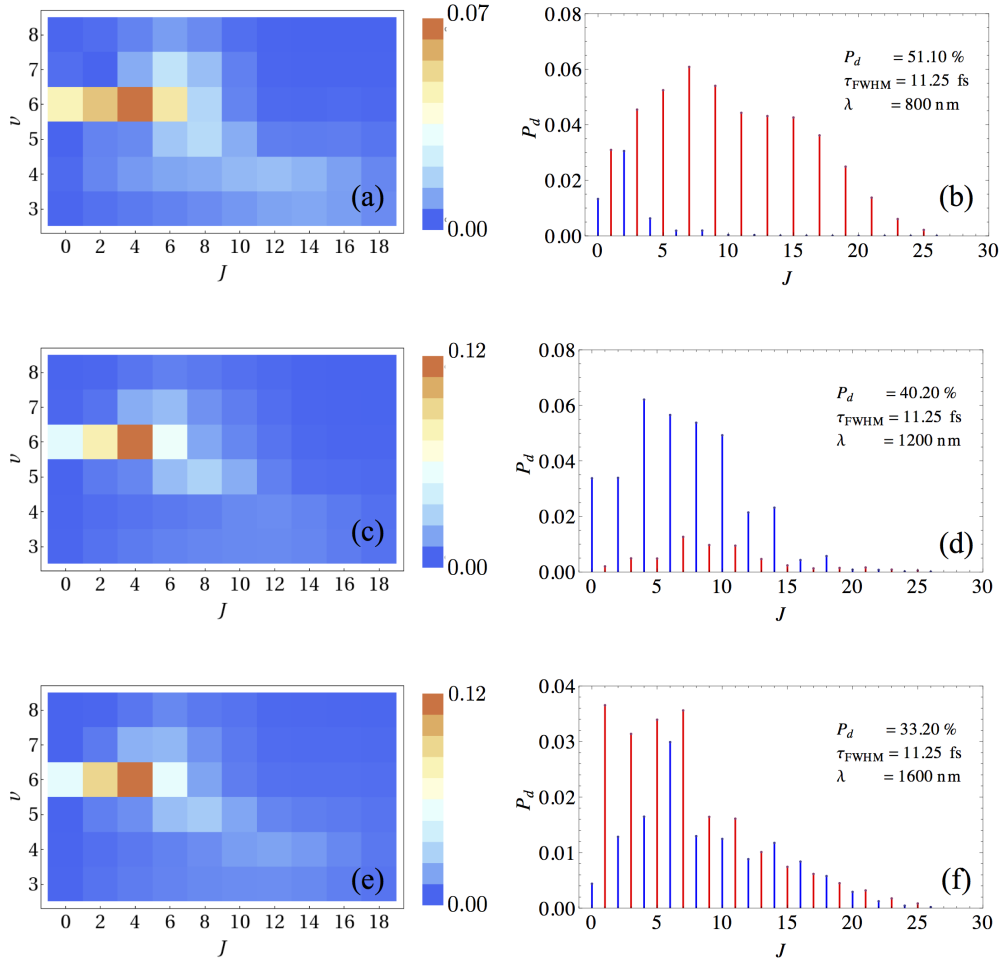
Figure 4.2: *(a)(c)(e)The rovibrational distribution of the bound states and (b)(e)(f) the J distribution for the continuum states. The blue and red lines in (b)(e)(f) indicate the electronic states $1s\sigma_g$ and $2p\sigma_u$, respectively. Three sets of calculations start from the same vibrational states $v = 6$ with a 11.25 fs pulse of (a)–(b) 800 nm; (c)–(d) 1200 nm; (e)(f) 1600 nm. The peak intensity is 1×10^{14} W/cm^2.*

4.3 Rovibrational dynamics in the photon-phase picture

It is curious to see how photons come into play among the significant rovibrational transitions in the intense field. We can visualize the rovibrational transitions in time within our photon-phase formalism. To do that, one can view the dynamical process in the diabatic or adiabatic representation where the adiabaticity is defined by the variation of the field in time.

The diabatic representation is the one where the numerical calculation is performed and each individual channel is formed from the field-free basis as shown in Eq. (3.11). The matrix form of Eq. (3.11) from discretizing R is,

$$i\frac{\partial}{\partial t}\mathbf{F}^{\mathrm{D}} = \Big[-\frac{1}{2\mu}\frac{\partial^2}{\partial R^2} + \mathbf{U}^{\mathrm{D}} + \mathbf{V}(t)\Big]\mathbf{F}^{\mathrm{D}}. \tag{4.1}$$

The diabatic potentials $\mathbf{U}^{\mathrm{D}}$, including both centrifugal potential and the electronic potential, are the diagonal elements in this representation, while the dipole couplings $\mathbf{V}(t)$ are off-diagonal between different channels. Note that in Eq. (4.1), the time dependence come from the variation of the field envelope. One can perform an unitary transformation at each R,

$$\mathbf{C}\mathbf{F}^{\mathrm{D}} = \mathbf{F}^{\mathrm{A}},$$

$$\mathbf{C}^{\mathrm{T}}\Big[\mathbf{U}^{\mathrm{D}} + \mathbf{V}(t)\Big]\mathbf{C} = \mathbf{F}^{\mathrm{A}}, \tag{4.2}$$

so that the adiabatic potential $\mathbf{F}^{\mathrm{A}}$ is diagonal. The correspondent TDSE in the adiabatic representation becomes,

$$i\frac{\partial}{\partial t}\mathbf{F}^{\mathrm{A}} = -\frac{1}{2\mu}\mathbf{C}^{\mathrm{T}}\frac{\partial^2}{\partial R^2}\mathbf{C}\mathbf{F}^{\mathrm{A}} + \mathbf{U}^{\mathrm{A}}\mathbf{F}^{\mathrm{A}} - \Big[\mathbf{C}^{\mathrm{T}}i\frac{\partial}{\partial t}\mathbf{C}\Big]\mathbf{F}^{\mathrm{A}}. \tag{4.3}$$

In this case, new potentials $\mathbf{U}^{\mathrm{A}}$ becomes time dependent as required from Eq. (4.2). In the field-free limit, the adiabatic curves $\mathbf{U}^{\mathrm{A}}$ will reduce to the piecewise combination of diabatic curves $\mathbf{U}^{\mathrm{D}}$ because adiabatic potential curves do not cross each other. This crossing points in $\mathbf{U}^{\mathrm{A}}$ become avoided-crossings as the field increases. The wavepackets tends to follow the adiabatic curve when the crossing is avoided when coupling is strong and make transitions at

the real-crossings otherwise. The adiabatic representation, however, introduces non-diagonal kinetic energy operator $-\frac{1}{2\mu}\mathbf{C}^{\mathrm{T}}\frac{\partial^2}{\partial R^2}\mathbf{C}$ and non-adiabatic coupling $\mathbf{C}^{\mathrm{T}}i\frac{\partial}{\partial t}\mathbf{C}$.

Both representations are mathematically exact and observables calculated in either representation should be identical, yet the preference is given to the one with the most benefits to help identify physical processes. The diabatic representation treats kinetic energy and field-free potentials as diagonals. When the transitions between different channels are not strong, this is the natural choice. However, when an intense field arrives, the wavepackets make transitions between the field-free electronic, rotational or photon channels. The magnitude of transition dipole in the field is indicated by the size of the gap of the avoided crossings in the adiabatic potential. In our problem, the energy separation of the gap and the nuclear kinetic energy are usually comparable. Guided by the calculation, we consider that the adiabatic representation be more suitable which will be seen in the following subsection.

I will show the evolution of wavepackets during a 20 fs long pulse of 2000 nm wavelength at the intensity 5×10^{13} W/cm^2 as an example in both representations. Two pictures gives different perspectives of the physical motions and transitions.

4.3.1 Diabatic representation

The probability density $\left|\mathbf{F}^{\mathrm{D}}\right|^2$ as a function of R for the individual channel is plotted in Fig. 4.3 on top of the correspondent potential curves. In the diabatic representation, the initial wave function starts with a single $J = 0$ state as displayed in Fig. 4.3(a). As the field progresses, wavepackets propagate towards higher photon-states as well as the higher partial waves. Restricted by the dipole selection rule in a linearly polarized light, the wavepacket can only make transitions from (m, J) to $(m \pm 1, J \pm 1)$ states sequentially. After passing the peak field of the pulse, significant portion of the wavepackets are visible up to 5ω in Fig. 4.3(d). However, the wavepackets on 4ω and 5ω channels fade away as the field drops and slowly merge into the lower photon channels. In the end, most dissociative wavepackets locate in 3ω channel in Fig. 4.3(f). At the same time, the bound part of the wave function
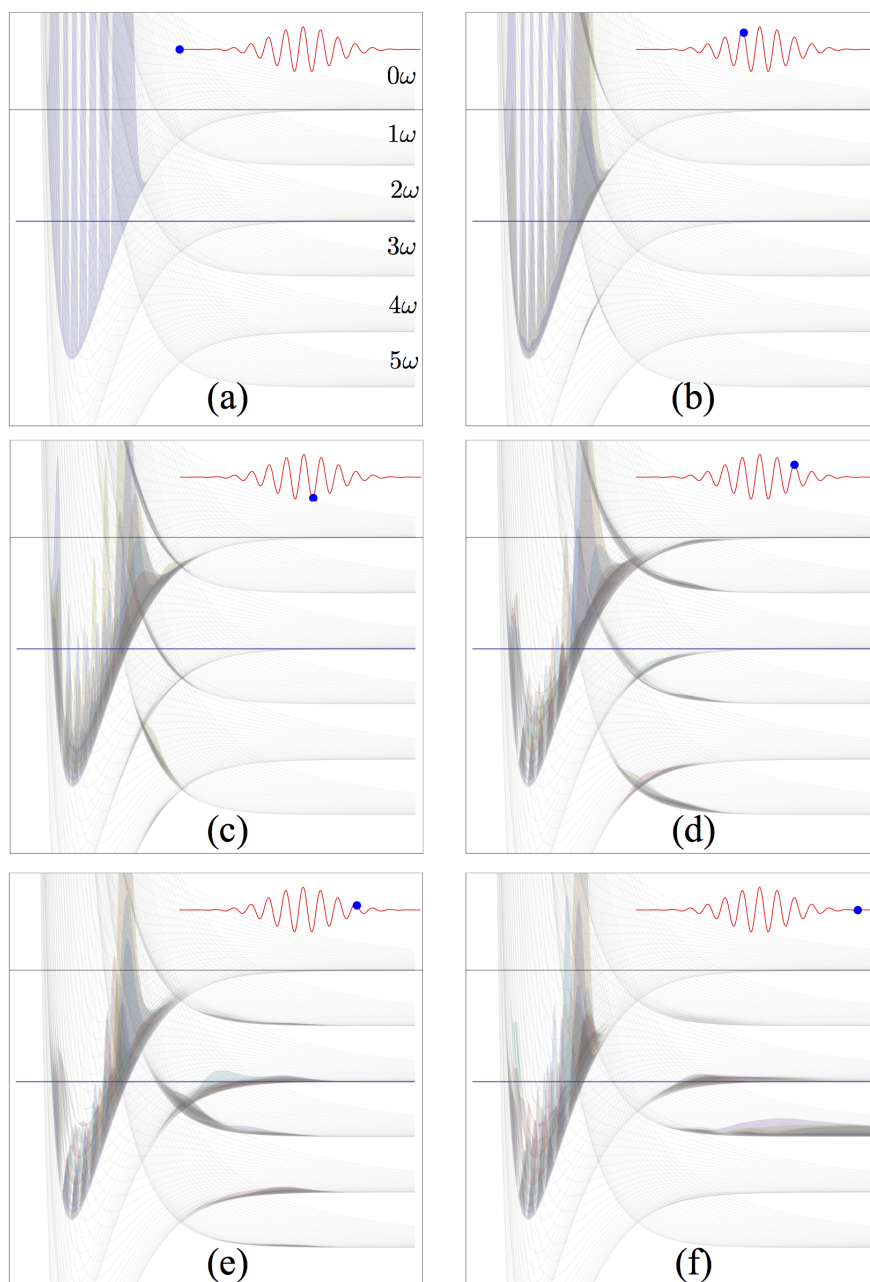
Figure 4.3: *The snapshots of the evolution of the wave function in the diabatic representation. The probability density of individual channel is plotted on top of the correspondent potentials. The blue spot show the instance during the pulse. The plot is based on a calculation with a 20 fs pulse of 2000 nm wavelength at the intensity 5×10^{13} W/cm^2. The energy of the initial state $v = 6$ is marked by the blue solid line.*

spreads out in the many partial waves of 0ω channel. The rotations energy gained from the pulse become significant enough to compare with the vibrational motion of the molecule.

In this representation, we can clearly visualize the transitions strictly guided by the selection rules. However, the locality of the dissociative wavepacket is obscure due to the transitions between different diabatic channels, and the populated intermediate states may not directly contribute to the final observables. This is not very helpful for identifying major physical pathways or predicting observables.

4.3.2 Adiabatic representation

The observables calculated in the adiabatic representation is identical to the diabatic representation because the former is simply an unitary transformation from the latter. Nevertheless, the adiabatic one provides an alternative perspective in terms of the wavepacket and its pathways. In Fig. 4.4, the $\left|\mathbf{F}^{A}\right|^{2}$ is plotted on top of the correspondent adiabatic potential curves. In the beginning of the pulse, the initial state is obviously not well represented because an adiabatic channels constantly switch characteristics at each sharp crossing so that the field-free state can only be in plotted in a piece-wise manner. However, when the field turns on, the infinitely sharp crossings become smooth avoided crossings due to the field distortion. Unlike the evolution in the diabatic representation in Fig. 4.3, the wavepackets do not hop in between different photon channels but follow the distorted potentials smoothly. In comparing to the correspondent figures in diabatic representation, the Fig. 4.4(c-e) show a large portion of the wavepacket tunnels out of the initially bounded potentials and move outwards. Because the wavepackets are localized in fewer channels in the adiabatic representation, it is more convenient to consider the dynamics of wavepacket on the potentials and the major dissociation pathways can be identified.
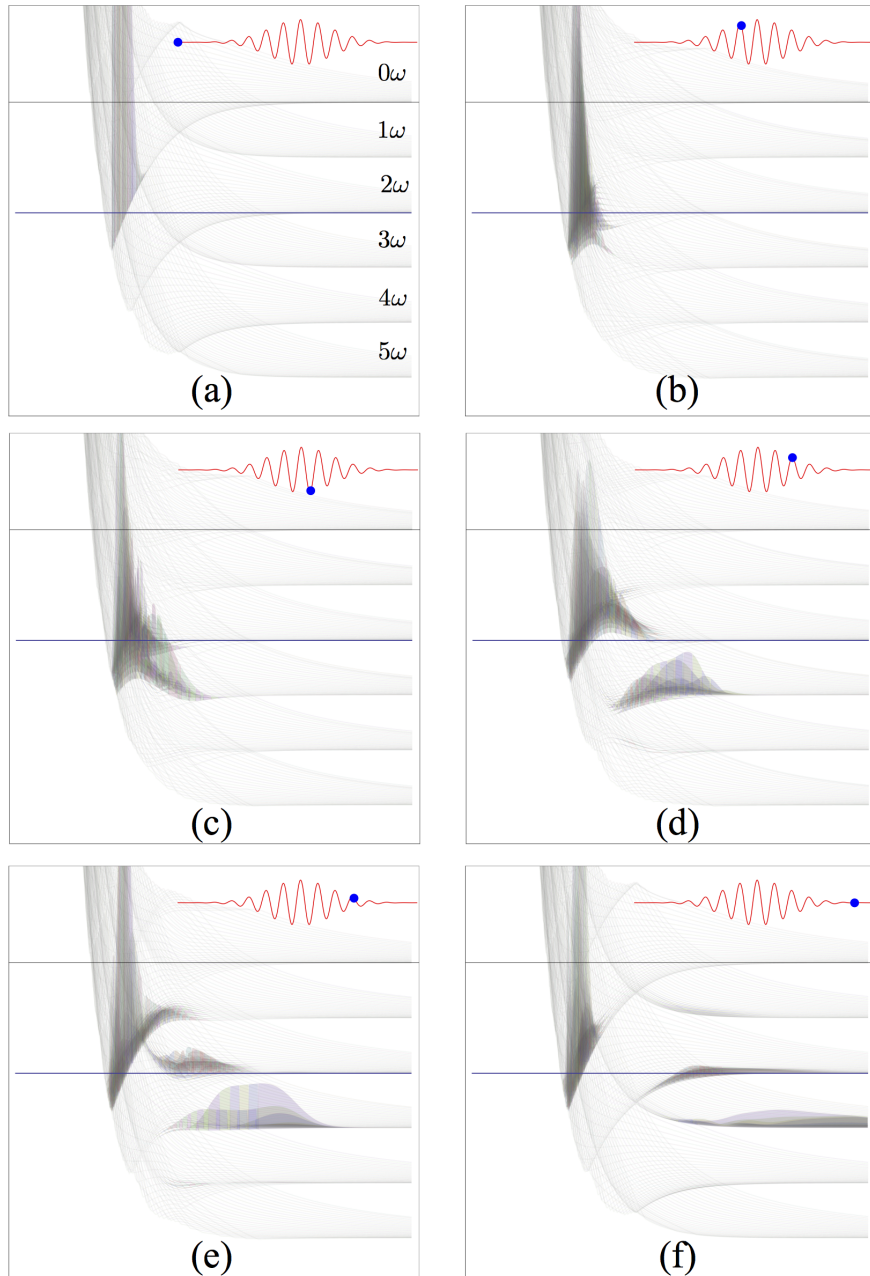
Figure 4.4: *The same plot as Fig. 4.3 but in the adiabatic representation. The left side of the adiabatic channels are chopped off because there are too many avoided crossings to visualize clearly.*

4.4 Post-pulse alignment

Molecules can exchange substantial angular momenta with the field even though the duration of the pulse can be much shorter than the molecular rotational timescale as shown in Fig. 4.2. The superposition of these rotational states of bound molecules can lead to rotational revivals [19, 20], which is also referred to as the impulsive alignment. Meanwhile, this may also lead to a strong angular dependence of dissociative fragments and the possibility of post-pulse rotations. However, this possible rotational dynamics is often ignored in the axial recoil approximation (ARA) [126] where the rotational motion is assumed to be frozen during dissociation. This approximation is more valid for fast electron impact ionization and XUV photodissociations, where typically the recoil energy is significantly higher than the rotational energy. However, using an intense infrared laser pulse to dissociate a molecule may give rise to a much lower kinetic energy release (KER) and high rotational energy, in which case, the condition required by ARA may not be satisfied.

Multiple cases have indicated the breakdown of ARA. Anis et $al.$ calculated the angular distribution of the H_2^+ and showed that fragments tend to align towards the polarization direction after a femtosecond pulse [121]. Tong et $al.$ pointed out that post-pulse rotation must be taken into account in O_2 double-ionization [127] in order to reach agreement between the measured angular distribution [128] and the one predicted by MO-ADK [129]. Wrede et $al.$ discussed the breakdown of ARA in the photodissociation of Br_2 and IBr near the threshold energy in a semi-classical model [130]. Similar questions were raised in studies of dissociative electron attachment [131, 132]. Clearly, the limits of ARA have been highlighted and the treatment beyond ARA becomes a necessity.

In this work, we are specifically interested in the response of individual initial states to an intense few-cycle pulse. For this case, two factors need to be considered from the very beginning. First, the carrier-envelope phase (CEP) dependence of the alignment needs to be considered first because CEP effects are proved to be general for few-cycle pulses [93]. Second, given wide spectral bandwidth and high intensity of a pulse, most initial states are

able to dissociate through multiple pathways, and they may overlap at the same energies. Therefore, the traditional treatment to distinguish different dissociation processes by their characteristic kinetic energy, such as bond softening [16], above threshold dissociation [17], is no longer feasible. In order to cope with these issues, we apply our photon-phase formalism to separate photon channels in the solution of the TDSE using the periodicity of the CEP. We are able to categorize pathways in terms of photon channels without relying on photon features in observables.

To quantify the overall influence of the post-pulse rotation of dissociating fragments, we compare two quantities: the expectation value of $\cos^2 \theta$ of the continuum wavefunction at the end of the laser pulse $\langle \cos^2 \theta \rangle_{t_f}$ and its asymptotic limit $\langle \cos^2 \theta \rangle_\infty$. We define t_f as the time when the intensity drops to 10^6 W/cm^2 and $\langle \cos^2 \theta \rangle_{t_f}$ is evaluated directly from integrating the continuum wavefunction. The asymptotic alignment parameter $\langle \cos^2 \theta \rangle_\infty$ is evaluated by integrating the angular distribution,

$$\langle \cos^2 \theta \rangle_\infty = \int \frac{\partial^2 P}{\partial \theta_K \partial E} \cos^2 \theta_K \sin \theta_K d\theta_K dE. \tag{4.4}$$

The alignment parameter $\langle \cos^2 \theta \rangle$ is properly normalized by dissociation probability. A deviation between these two quantities reflects the failure of ARA.

4.4.1 Carrier-envelope phase dependence

With the radial amplitudes $F_{m\beta J}$ in Eq. (3.11), the expectation value of $\cos^2 \theta$ is written with photon channels expansions explicitly,

$$\langle \cos^2 \theta \rangle = \sum_{\beta J} \langle Y_{J0}| \cos^2 \theta |Y_{J0}\rangle \sum_{m,m'} \langle F_{m\beta J}|F_{m'\beta J}\rangle e^{i(m-m')\varphi}$$
$$+ 2\mathrm{Re}\left[\sum_{\beta J} \langle Y_{J0}| \cos^2 \theta |Y_{J+2,0}\rangle \sum_{m,m'} \langle F_{m\beta J}|F_{m'\beta,J+2}\rangle e^{i(m-m')\varphi} \right] \tag{4.5}$$

The leading order φ dependence comes from the interference of photon channels m and $m\pm2$, because the dipole selection rule forbids the photon channels m and $m \pm 1$ share the same spatial symmetry. For a strong field with a large bandwidth, photon channels may overlap,
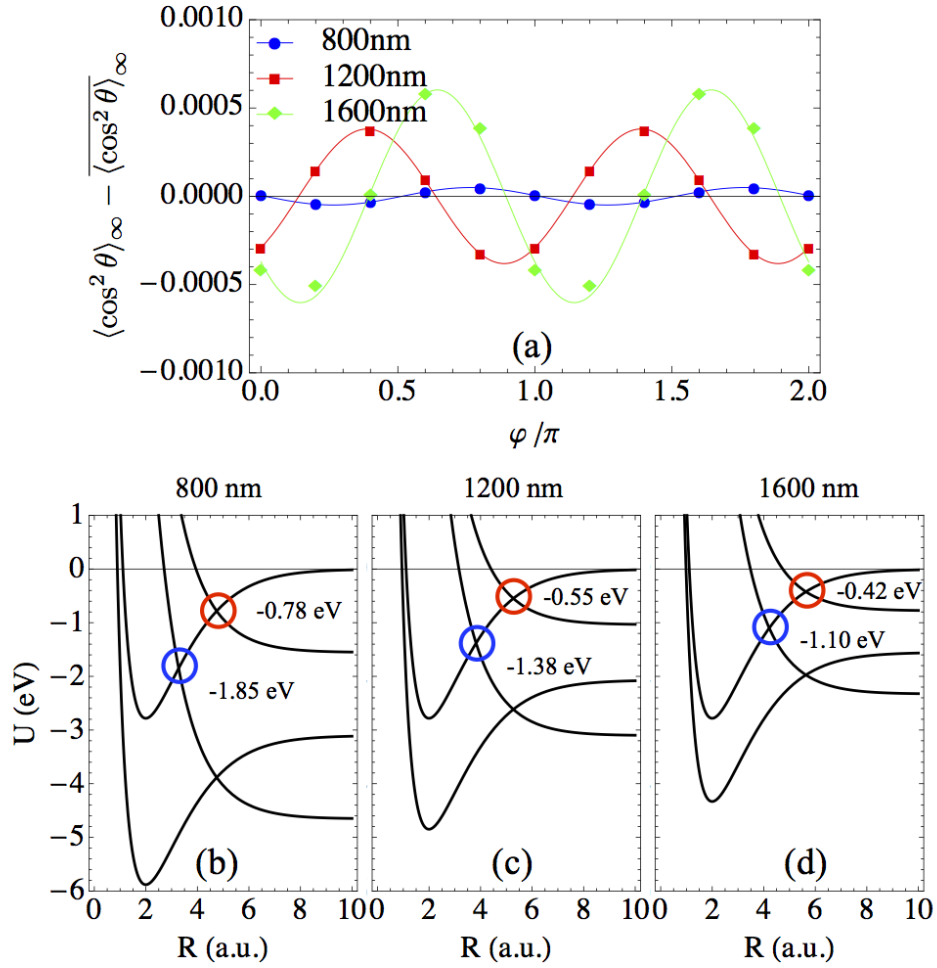
Figure 4.5: *(a) Carrier-envelope phase φ dependence of $\langle \cos^2 \theta \rangle_\infty$ for $v = 10$ state of H_2^+. Laser parameters are 5×10^{13} W/cm^2 and $\tau_{\text{FWHM}} = 3$ cycles. (b)(c)(d) are the diabatic Floquet curves. The red circle marks 0ω–1ω crossing and the blue one marks 0–3ω crossing.*

but the magnitudes of photon channels with $m - m' = 2$ at the overlap are expected to be very small. Therefore, we anticipate very weak CEP dependence of alignment. This statement is confirmed by Fig. 4.5(a). The calculated $\langle \cos^2 \theta \rangle_\infty$ is modulated by CEP with π-periodicity on top of the mean value of $\langle \cos^2 \theta \rangle_\infty(\varphi)$. The amplitude of the modulations is significantly smaller than the unity, consistent with our expectation of two photon interferences. Hence

we will leave CEP dependence out of the discussion in the current Chapter. Furthermore, we can neglect such cross terms and define the alignment characters of individual photon channels below,

$$\langle \cos^2 \theta \rangle^{(m)} = \sum_{\beta J} \langle Y_{J0} | \cos^2 \theta | Y_{J0} \rangle \langle F_{m\beta J} | F_{m\beta J} \rangle$$
$$+ 2\text{Re} \sum_{\beta J} \langle Y_{J0} | \cos^2 \theta | Y_{J+2,0} \rangle \langle F_{m\beta J} | F_{m\beta,J+2} \rangle, \tag{4.6}$$

so that

$$\langle \cos^2 \theta \rangle \approx \sum_m \langle \cos^2 \theta \rangle^{(m)}. \tag{4.7}$$

However, this decomposed alignment parameter $\langle \cos^2 \theta \rangle^{(m)}$ relies on the fact that there is no significant interference terms in the observables. As a counterexample, the orientation parameter $\langle \cos \theta \rangle$ can be strongly affected by CEP in a heteronuclear molecular dissociation [133], in which case the leading term of CEP dependence is the interference between m and $m \pm 1$ channels. The neighboring channels are more likely to overlap comparing to the channels m differed by 2. Then the decomposition will no longer be valid without the interference terms. For a homonuclear system, however, the orientation is irrelevant, allowing us to identify individual photon channel contribution in Eq. (4.5).

4.4.2 Dissociation probability, alignment parameter and angular momentum distribution

We find the post-pulse behavior is closely related to the dissociation pathways. To substantiate this statement, we show the dissociation probability and alignment parameters of individual initial states under various wavelengths.

The overall features of the post-pulse rotation of the H_2^+ photodissociation fragments is captured in Fig. 4.6(i-l), where more than 10% deviation between $\langle \cos^2 \theta \rangle_{t_f}$ and $\langle \cos^2 \theta \rangle_\infty$ is found and depicted by the shade. This alerts us the break-down of the ARA and indicates the fragments are most likely further align towards the polarization direction in the field-free
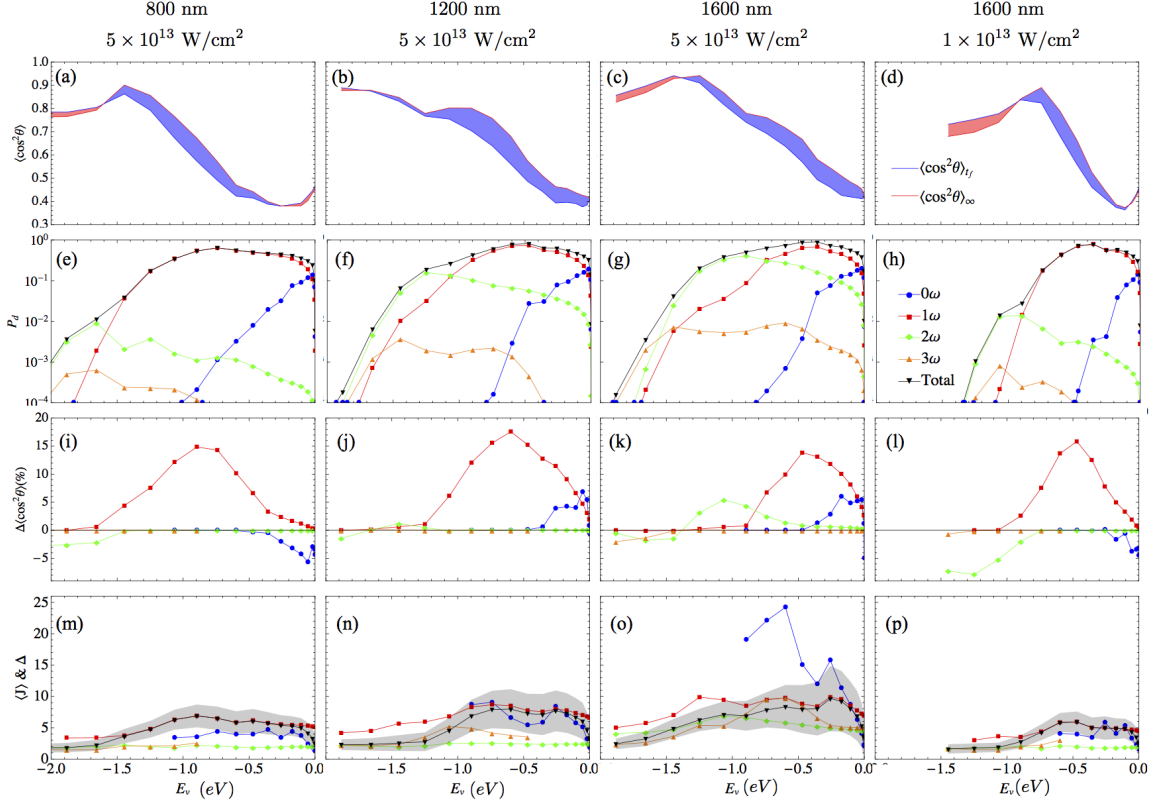
Figure 4.6: *Row 1: overall alignment parameters $\langle \cos^2 \theta \rangle_{t_f}$, $\langle \cos^2 \theta \rangle_\infty$. The color of the shades in between the alignment parameters indicates the trend of the post-pulse rotation. Blue represents fragments further align and red represents anti-alignment. Row 2: dissociation probability P_d. Row 3 : $\Delta\langle\cos^2\theta\rangle$ of individual photon channels as the percentage of $\langle \cos^2 \theta \rangle_\infty$. Row 4: J-distribution of individual photon channels described by $\langle J \rangle$ and σ_J (see the definition in the text). the gray strips represent the width σ_J of the total angular momentum distribution. Row 2–4 share the same legend. All quantities above are plotted as a function of the initial state energy E_v. The numerical results are propagated through a three cycles Gaussian pulse.*

propagation [121]. However, exceptions can be found among the initial states on the edges of the plots where pink shades suggest the post-pulse anti-alignment of the fragments. Clearly the response of the fragments after the impact of a short pulse depends on the initial states and laser parameters. Our photon-phase formalism allow us to distinguish different physical processes in terms of photons and help identify the dependence of individual dissociation pathways extracted using approach from Sec. 2.

The dissociation probabilities of individual photon channels along with the total dissociation are plotted in Fig. 4.6(e-h). For many initial states among four cases shown in the figure, 1ω channel is the dominant one and imparts the dissociation probability curve a characteristic peak near the 0ω–1ω crossing as marked in Fig. 4.5. This peak shifts towards the dissociation threshold as the wavelength increases. The net zero photon dissociation [120, 134] takes place near the threshold and the dissociation probability curves drop quickly as moving towards the lower bound states. As the Raman transitions takes place, the wavepackets are promoted to higher rotational states and pushed out of $1s\sigma_g$ attractive well due to the centrifugal barrier, leading to the dissociation without absorbing net photons. For this reason, radial wavepackets from this channel with very low kinetic energy (< 0.1 eV) allow dissociating wavepacket from this channel to rotate in a longer timescale compared to the other photon channels. The multiphoton processes are relatively weak for 800 nm case and become more noticeable as the wavelength increases. Meanwhile, due to the multiphoton nature, the dissociation probability drops quickly in the case of the lower intensity as shown in Fig. 4.6 (h).

Similarly, we are able to study the post-pulse rotation of individual photon channels behavior. To exemplify the contribution of them, we plot $\Delta\langle\cos^2\theta\rangle^{(m)} = \langle\cos^2\theta\rangle^{(m)}_\infty - \langle\cos^2\theta\rangle^{(m)}_{t_f}$ in Fig. 4.6(i-l). As we expected from the dominant 1ω-dissociation in Fig. 4.6(e-h), 1ω channel is mostly responsible for the significant post-pulse rotation. More importantly, the red curves in Fig. 4.6(i-l) indicates the most significant 1ω PPA occurs near energies at the 0ω–1ω crossings as marked in Fig. 4.5(b-d). This observation is consistent

across all wavelengths and intensities as shown in our figures.

This pathway dependent alignment behavior can be interpreted in terms of the photon-dressed potentials. Since angular motion is the focus of the study, we plot out the adiabatic photon-dressed potential surfaces, with respect to both radial and angular coordinates, for the three wavelengths at two different intensities in Fig. 4.7. Clearly, different photon channels show very distinct characters. For example, Fig. 4.7(a)(c) show that, in the 800 nm cases at both intensities, 1ω surface is slanted down towards $\theta = 0°$, whereas 0ω and 2ω surface is slanted down towards $\theta = 90°$. While the field is on, the potential surface forms slope in the θ-direction so that the wavepacket is pushed towards the polarization direction or the perpendicular direction. This explains why 1ω-channel show alignment while 2ω-channel and 0ω-channel show anti-alignment in Fig. 4.6(i).

The multiphoton effects reveal themselves more clearly in the cases of longer wavelengths. In Fig. 4.7(c) for the 1600 nm at the intensity of 5×10^{13} W/cm^2, the surfaces show the convoluted shape for all photon channels. Given the fact that multiphoton dissociations require high intensity to initiate, the dissociating wavepackets are most likely to be released from the potential well as the avoided-crossings are widely open. In the example of Fig. 4.7(c), the 2ω surface at the wide open 0ω–3ω avoided crossing show downward slope to the $0°$ angle, forcing the wavepacket to align along the polarization direction. Therefore, the 2ω-channel dissociation exhibit fairly notable post-pulse alignment in Fig. 4.6(k). On the contrast, in the calculation at the lower intensity 1×10^{13} W/cm^2 for the same wavelength, the dissociating wavepacket never sees a downward slope to the $\theta = 0°$ even at its peak intensity as shown in Fig. 4.7(f), the 2ω dissociating fragments align to the orthogonal direction in Fig. 4.6(l). In general, we expect complex evolution of wavepackets on the varied shape of potential surfaces due to the high intensity. However, because these higher order effects modify the surfaces in fairly nonlinear manner and the wavepackets from these higher-photon channels typically have large kinetic energy, we do not expect significant post-pulse rotation from such processes compared to the 1ω channel. It is true that even for the
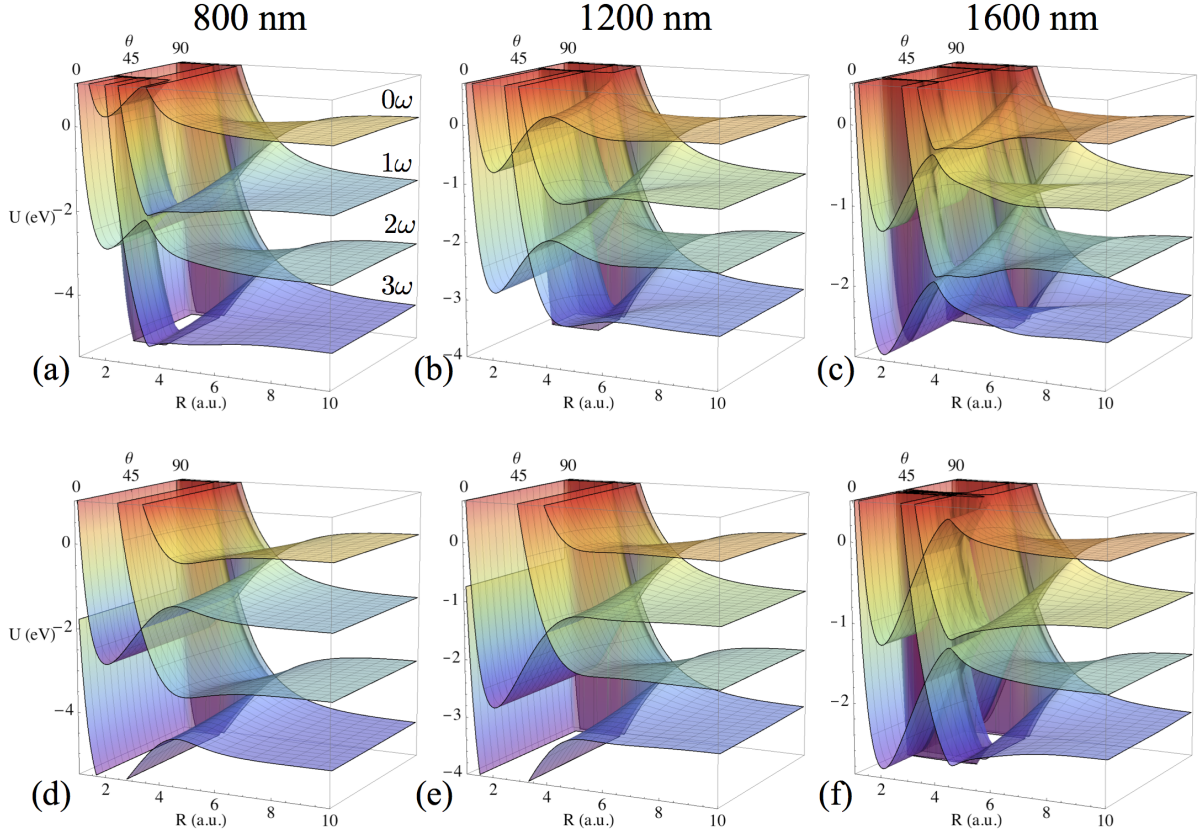
Figure 4.7: *Photon-dressed adiabatic potential surfaces as a function of R and θ for three wavelengths: (a)(d) 800 nm, (b)(e) 1200 nm and (c)(f) 1600 nm. The adiabatic potentials (a)(b)(c) are generated at the intensity 5×10^{13} W/cm², while (d)(e)(f) are generated at 1×10^{13} W/cm². The sharp crossings in such surfaces, where the wavepackets are expected to follow the diabatic potentials, are smoothened so that only a handful of surfaces are needed to describe the dynamics.*

1ω channel, the surface has concave structure when intensity is sufficiently high, as shown in Fig. 4.7(c). However, in our calculations, the 1ω channel shows consistently pronounced post-pulse alignment. We consider that is because the 0ω–1ω avoided crossing opens at very early stage of the pulse (at below 10^{12} W/cm²) and imparts a substantial impulse to align the fragments through the descending slope towards $0°$ in the θ-direction. Although this adiabatic photon-dressed potential surfaces provide an intuitive picture to understand the nuclear rotation in the strong field, the non-adiabatic effects by $\mathbf{C}^{\mathrm{T}} i \frac{\partial}{\partial t} \mathbf{C}$ may also modify

the observables when the pulse is sufficiently short.

To obtain more insights and support pervious explanations, it is useful to look at the angular momentum distribution at the end of the pulse, in which case the observables are gauge-independent. We plot out the mean value $\langle J \rangle$ of individual photon channels and the width $\sigma_J = \sqrt{\langle J^2 \rangle - \langle J \rangle^2}$ of the total distribution in Fig. 4.6(m-p).

As expected from the significant post-pulse alignment of 1ω-channel in Fig 4.6(i-l), the $\langle J \rangle$ of this channel is high compared to the other channels for the most cases in Fig. 4.6(m-p). One explaination is that the wavepacket dissociated from this channel is most likely to go through 0ω–1ω avoided crossing. At the crossing point, the Raman-transition is enhanced due to the existing intermediate state $2p\sigma_u$ that can be reached by one-photon. This resonance-like condition facilitates Raman transitions effectively compared to the traditional Raman transitions through intermediate virtual states [19, 114]. Therefore, we expect the initial states near the 0ω–1ω crossing will be more likely to produce a broad rotational wavepacket thus facilitating PPA.

However, due to the radial motion of the wavepacket, it is not obvious to see a very broad J distribution from the initial states near the 0ω–1ω crossing in Fig. 4.6(m–p). For H_2^+, a wavepacket can move 1 a.u. radial distance given 1 eV kinetic energy within one optical cycle at 800 nm. In this case, a created wavepacket near the 0ω–1ω crossing can quickly move away from the crossing due to the repulsive potential $2p\sigma_u$. Consequently, the rotational transitions gradually diminish. From our calculations, even with the radial motion, the states near the 0ω–1ω crossing still possess very high rotation levels compared to the multiphoton dissociation. For example, among all cases shown in Fig. 4.6(m-p), the 1ω channel angular momentum distribution marked by the red curves, lies above 2ω and 3ω curves, representing a relatively broader rotational wavepacket. The exception is at $E_v \approx -0.6$ eV in Fig. 4.6(o), which is closer to the 0ω–1ω crossing. The states near this crossing access very high rotational states, yet a small portion of the wavepacket could dissociate through 3ω process given a sufficient intensity. As a result, 1ω and 3ω end up with

a similar J-distribution. Nevertheless, the broad J distribution is not an essential condition for the post-pulse alignment. Comparing $\Delta\langle\cos^2\theta\rangle$ and Js distribution in Fig. 4.6, the highest angular momentum distributions do not always reflect the most significant post-pulse rotation. The relative phases of individual rotational states also have a crucial impact on the post-pulse behavior. Yet due to the convoluted radial and rotational motions, these phases are difficult to predict except performing the calculations.

4.4.3 Isotopes and heavier molecules

From our calculation, the post-pulse alignment in the 1ω dissociation of H_2^+ is found to be significant. Naturally, the following question is if it is also true for heavier systems. A simple argument to support ARA is that, for a given rotational state and kinetic energy, the classical recoil angle scale with $1/\sqrt{\mu}$ [127], which implies the post-pulse rotation of heavy molecules is less dramatic. However, the mass not only exhibits itself in the field free evolution, but also serves as an important factor in determining the initial angular momentum for free evolution. To show how extensive the post-pulse alignment is in the few-photon dissociation, we calculate the photodissociations with 3-cycle 1600 nm laser the same as Fig. 4.6(c) for heavier model systems. We assume the model systems share the identical electronic structures as H_2^+ so that the role of various electronic transitions will be removed from the discussion.

With identical electronic structure and pulse parameters, we focus on the mass dependence in order to test if heavy systems will be immune to the PPA. For this purpose, three heavier model systems whose mass is equivalent to N_2, Cl_2 and I_2 are also adopted in the calculations.

Our calculations show that the post-pulse alignment is present even for the systems much heavier than H_2^+, despite the fact that PPA diminishes as the mass significantly increases. This decreasing trend of PPA to some point advocates neglecting rotation, however even for the heaviest system we tested, ARA is still fairly crude approximation to use. Furthermore,
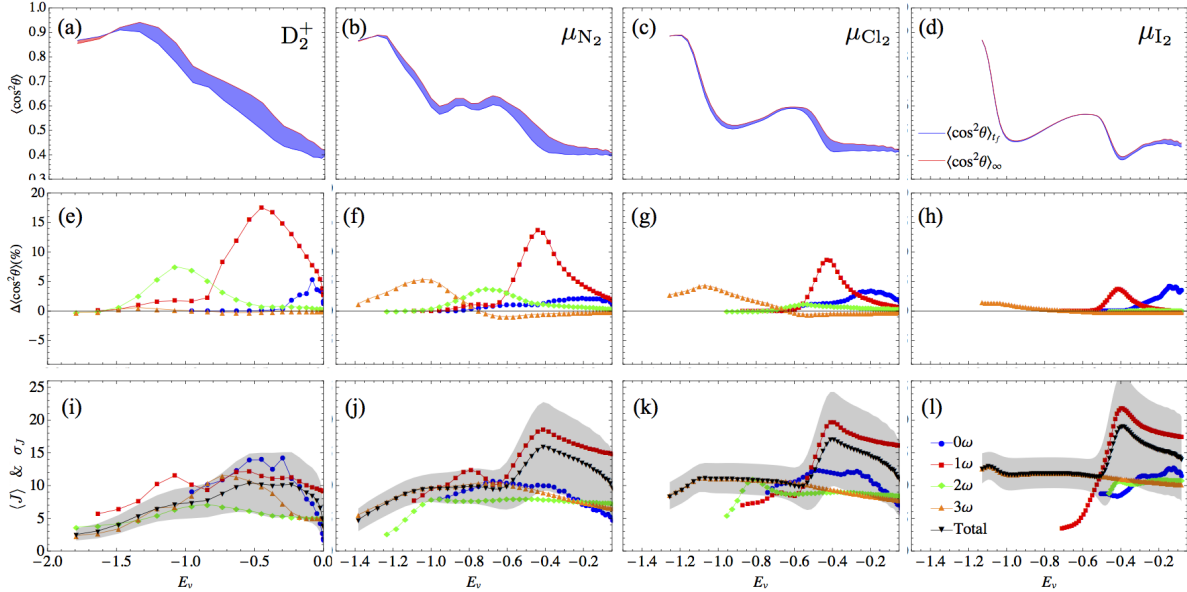
Figure 4.8: *The same plots as Fig. 4.6 with heavy isotopes and model system. All cases are calculated with a $\tau_{\text{FWHM}} = 15.0$ fs pulse of 1600 nm at the intensity 5×10^{13} W/cm^2, same as Fig. 4.6(c).*

compared to H_2^+, D_2^+ shows larger magnitude of PPA in Table 4.1. Even though the heavier mass reduces the magnitude of the field free rotation, it may promote broad J distribution. At a fixed nuclear distance R, rotational transition occurs most effectively when two electronic states coupled resonantly. Compared with H_2^+, radial motion of heavier systems is slower in that it can be better described by a rigid-rotor, but still not accurate enough. With 1 eV kinetic energy, a system as heavy as I_2 can move 0.1 a.u. within an optical cycle of a 1600 nm laser, while this displacement in radial dimension can cause 0.1 eV change as a significant detuning for the rotational transition. Consequently, light molecules, due to its fast radial motion, typically move away from the crossing quickly and promote limited partial waves during the pulse. On the contrary, N_2-like, Cl_2-like and I_2-like systems show higher J distribution in 1ω channel as shown in Fig. 4.8 (j-l). For the same reason, heavier systems show more conspicuous peaks in J distribution near the crossings, which is opaque

in the H_2^+ and its isotopes. In conclusion, heavier mass reduces the post pulse rotation and at the same time promotes rotational transition during the pulse, the result of which does not rule out the possibility of significant post-pulse rotation for heavy molecules.

The change of the expectation value of $\cos^2\theta$ after the pulse is a good measurement of the overall trend of post-pulse rotation, but it does not capture the complete picture. To demonstrate the influence of the post-pulse rotation to structure changes, we plot out the angular distribution,

$$\rho(\theta_K)_\infty = \int \frac{\partial^2 P}{\partial E \partial \theta_K} dE$$
$$\rho(\theta)_{t_f} = \int |\Psi(R,\theta,t_f)|^2 dR \tag{4.8}$$

in Fig. 4.9, comparing both H_2^+ and Cl_2-like system in 800nm and 1600nm wavelengths. We choose the initial states closest to the crossing positions, which is affirmed to undergoes the strongest PPA, to illustrate its effects on angular distribution. All four cases show comparable $\Delta\langle\cos^2\theta\rangle$, however, the actual modification of the angular distribution differs. Comparing Fig. 4.9(a,c), we find similar $\Delta\langle\cos^2\theta\rangle$ in numbers, yet the angular distribution indicates a more noticeable change in (c), likewise in comparing (b) and (d). To quantify the structure modification of angular distribution, we define a metric η as below

$$\eta^2 = \frac{1}{2} \int_0^\pi \left(\frac{\rho_{t_f} - \rho_\infty}{\rho_{t_f} + \delta}\right)^2 \sin\theta d\theta, \tag{4.9}$$

Table 4.1: *Mass dependance for post-pulse alignment of the initial state closest to the 0ω–1ω crossing -0.423 eV.*

Elements	E_v(eV)	P_d(%)	$\langle\cos^2\theta\rangle_\infty$	$\Delta\langle\cos^2\theta\rangle$
H_2^+	-0.470	87.7	0.668	0.098(14.7%)
D_2^+	-0.450	77.5	0.612	0.112(18.3%)
μ_{N_2}	-0.411	44.3	0.496	0.076(15.3%)
μ_{Cl_2}	-0.430	32.5	0.479	0.048(10.0%)
μ_{I_2}	-0.419	21.0	0.406	0.015(3.6%)
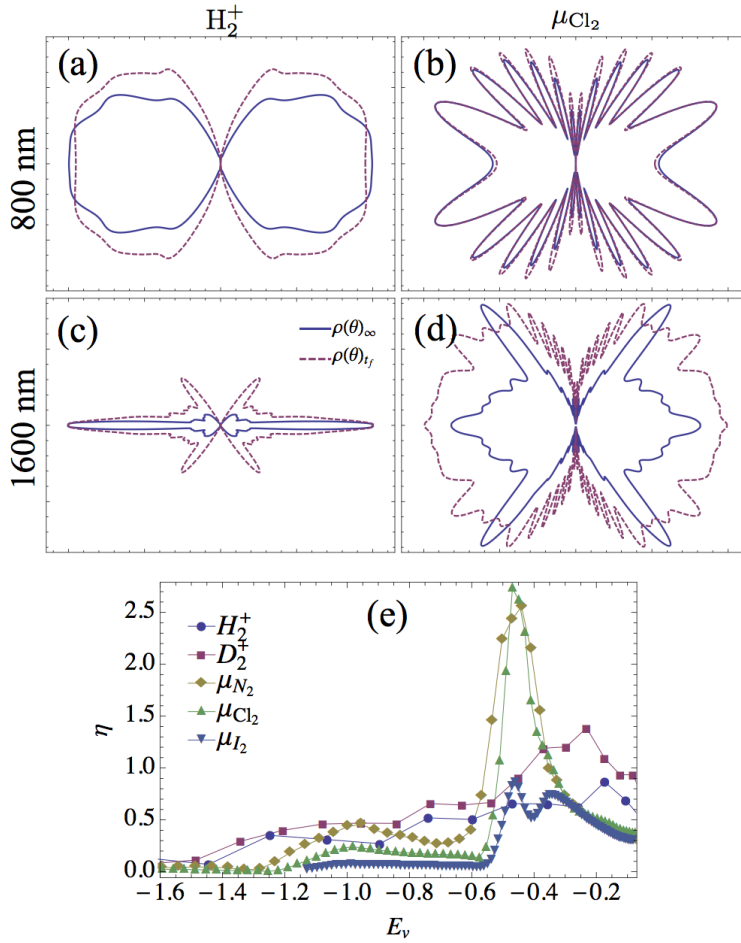
Figure 4.9: *Angular distribution of the fragments $\rho(\theta)$ dissociated by a three cycle pulse of the wavelengths 800 nm and 1600 nm at the intensity 5.0×10^{13} W/cm^2. The initial states are chosen to be the one closest to the 1ω crossing. The alignment parameter deviation $\Delta\langle\cos^2\theta\rangle$ of each cases are (a) $+0.081(14.2\%)$, (b) $+0.027(6.1\%)$, (c) $+0.098(14.7\%)$, (d) $+0.048(10.0\%)$. Angular distribution deviation η is plotted for all masses in the case of 1600 nm in (e).*

where δ is a cut-off value chosen to be 1% of the maximum of ρ_{t_f}. This structure deviation η for various masses is shown in Fig. 4.9(e). To make ARA valid, η value should be reasonably close to zero to accurately describe the angular structure, while Fig. 4.9(e) shows in general it is significantly higher than zero. Moreover, η can reach even above 1 for intermediate sized molecule such as Cl_2 and N_2 near the crossing, which means ARA even fails to describe the qualitative feature of the angular distribution.

4.5 Summary

Full dimensional calculations for homonuclear diatomic molecules in various laser pulses of mid-infrared wavelengths are presented in this article. We compare the post-pulse rotation of individual initial vibrational states and categorize them in terms of net photons within our photon-phase formalism. Depending on the dissociation pathways, nuclear fragments can align or anti-align to the laser polarization direction during the post-pulse propagation. In either case, the axial recoil approximation is inappropriate, especially in longer wavelengths region. The most significant post-pulse alignment occurs in the 1ω channel, which is facilitated by rotational transitions due to the near resonant condition. In addition, the post-pulse rotation of large mass model systems are tested and found to be non-negligible even for a system as heavy as I_2 in the long wavelength case.

Chapter 5

Carrier-envelope phase controlled photodissociation of H_2^+

In this chapter, we focus on the control capability of CEP over dissociation fragments under the influence of a few-cycle intense laser pulse. Depending on the structure of the system and the laser parameters, the target system may undergo several pathways to dissociate. By manipulating the phase of pathways with CEP, we are able to control the outcomes due to the interference effects of pathways. This control impact may be exhibited as modulation in the observables such as dissociation probabilities, total KER spectra and momentum distribution, as we already established in Chapter 2 and Chapter 3.

Several experiments using the CEP to control the dynamics of simple diatomic molecules have already been carried out [1, 2, 75, 78, 80, 91]. Although most studies to date have used an 800-nm central wavelength, some studies suggest that moving towards mid-infrared wavelengths may enhance the CEP control over molecular dynamics [67, 68, 86, 87]. Therefore, we aim here to explore this possibility, and at the same time understand the underlying physical mechanisms within our photon-phase picture.

Many theoretical works have disscussed the role of CEP in photodissociation [63, 69, 71, 72, 135]. It is not uncommon, however, to find that the degree of CEP control is overestimated in theory compared to experiment. One reason is that calculations are commonly performed within a reduced-dimensional model that constrains the motion to lie along the

polarization direction. Another reason that CEP effects are exaggerated in theory is that the intensity dependence within the laser focus is usually neglected—even though it can change an observable qualitatively. Its significant impact arises from the variation of the laser intensity within the experimental reaction volume, and the incoherent average of the theoretical results tends to wash out any CEP effect.

5.1 CEP effects of longer wavelengths

Carrier-envelope phase effects on dissociation are commonly understood in the literature using a picture based on following the electric field. Specifically, the electron is driven back and forth between the nuclei by the field, weakening the bond until the nuclei begin to dissociate. The electron continues to oscillate between the nuclei as they fall apart, eventually localizing on one of them when it can no longer pass to the other. With this picture, one may envision that longer wavelengths slow the electronic motion to a scale more comparable to the timescale of the nuclear motion, implying fewer oscillations of the electron and thus allowing greater control over the electron localization. There have been several studies advocating such an approach, reasoning that matching the timescale of the chemical reaction to the laser period is responsible for the enhancement of CEP effects in the mid-infrared regime [67, 86, 136].

This picture, however, has been applied almost exclusively to the dissociative ionization process in, for instance, H_2 [86], whereby a coherent vibrational wavepacket is produced in the ground ionic channel by ionization near a field maximum. This wavepacket then travels from the Franck-Condon region to the outer turning point where it couples more efficiently to the excited channel with opposite (ungerade) symmetry via bond softening. Thus, this process has a clearly defined nuclear timescale that is not always present in strong-field molecular processes. Moreover, by using the language of bond softening and making a transition to the ungerade electronic state, this picture mixes a field-following picture with a photon-based picture—*i.e.*, Floquet (see Ref. [96]). Finally, describing CEP effects as

due to mixing of gerade/ungerade states is distinctly homonuclear-centric, thus requiring a different explanation for heteronuclear systems.

In contrast, our photon-phase representation, presented in Sec. 3.4, is completely general, describing all CEP effects—whether for atoms or molecules—within a single, consistent picture. Specifically, from Eqs. (3.14) and (3.15), all CEP-dependent modulation in the observables can be understood as the interference of different photon channels, which fundamentally requires multiple photon pathways to overlap in energy. We can thus maximize the likelihood of strong CEP effects by considering laser wavelengths for which H_2^+ requires multiple photons for dissociation. This requirement immediately suggests wavelengths longer than 800 nm since most of the H_2^+ vibrational states need only a single photon for dissociation in this case. We will therefore consider wavelengths in the 800–2000-nm range.

Equations (3.14) and (3.15) also show that the likelihood of CEP effects can be increased by increasing the energy overlap of the different photon channels. If we performed our wavelength study with a fixed pulse length, this is precisely what would happen since the relative bandwidth $\Delta\omega/\omega$ would increase. This follows from the fact that the widths of the individual photon peaks [the $m = m'$ terms in Eq. (3.16)] scale with the bandwidth of the laser pulse—at least in a lowest-order perturbation theory (LOPT) sense. To avoid this rather trivial CEP effect enhancement, we have fixed the relative bandwidths of the pulses by choosing τ_{FWHM} to be three cycles of the carrier. One consequence of this approach is that for a given fixed peak intensity, the pulse energy grows with wavelength. With additional energy pumped into the system, one may expect a greater CEP effect. We will show, however, that CEP effects do not grow monotonically with intensity. Therefore, we will present a range of intensities and focus on the intensity dependence and its structure.

For concreteness, our discussion below will focus on the case of an H_2^+ ion beam target [1, 2, 137, 138]. The H_2^+, produced in an ion source long before interacting with the laser, is in an incoherent distribution of vibrational states approximately described by the $H_2 \rightarrow H_2^+$ Franck-Condon distribution [139]. Given this scenario, when we discuss a single vibrational
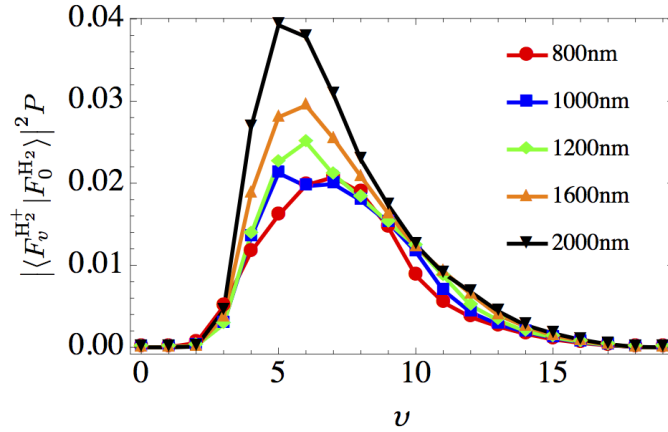
Figure 5.1: *Dissociation probability P as a function of initial vibrational state at $I = 10^{14}$ W/cm^2, weighted by the Franck-Condon factor.*

state, we will choose $v = 6$ since it lies at or near the peak of the Franck-Condon-weighted dissociation probabilities for all wavelengths (as shown in Fig. 5.1) and is thus a major contributor to the measurable signal.

5.1.1 Asymmetry and total yield for $v = 6$

In Fig. 5.2, we show the normalized asymmetry defined in Eq. (6.2) for $v = 6$ as well as the total yield. The figure shows that with the trivial wavelength effect removed, the magnitudes of asymmetry for different wavelengths are comparable. In particular, the asymmetry for 800 nm and 1200 nm are shown in Figs. 5.2(a)–(d). In the top row, where the intensity is fixed at 10^{14} W/cm^2, the magnitude of the maximal asymmetry for both wavelengths reaches about 0.6. We also show the asymmetry at a lower intensity, 3×10^{13} W/cm^2, for both wavelengths in the second row. Since the magnitude of the asymmetry reaches 0.7 for 1200 nm at this intensity, this figure disproves the notion that asymmetry simply grows with intensity. Other wavelengths also show non-trivial dependence on intensity.

One complicating factor is that the CEP dependence of the normalized asymmetry $\mathcal{A}(E)$ from Eq. (6.2) is due not just to the difference in the numerator, but also to the yield in the denominator [64]. To demonstrate the potential for CEP-dependent yields, we plot the
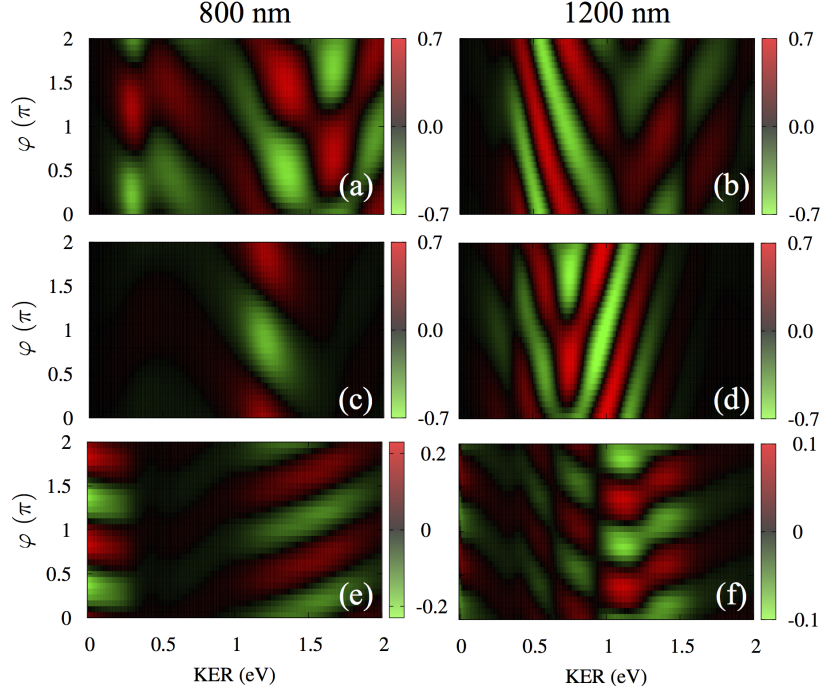
Figure 5.2: *Normalized asymmetry $\mathcal{A}$ as a function of CEP and KER for $v = 6$ for (a) 800 nm, 10^{14} W/cm^2; (b) 1200 nm, 10^{14} W/cm^2; (c) 800 nm, 3×10^{13} W/cm^2; and (d) 1200 nm, 3×10^{13} W/cm^2. The normalized modulation of the total yield $\mathcal{Y}$ for (e) 800 nm, 10^{14} W/cm^2 and (f) 1200 nm, 10^{14} W/cm^2.*

normalized modulation of the yield,

$$\mathcal{Y} = \left(\frac{dP}{dE} - \left\langle\frac{dP}{dE}\right\rangle_\varphi\right) \Big/ \left\langle\frac{dP}{dE}\right\rangle_\varphi, \qquad (5.1)$$

(where the angle brackets and φ label indicate an average over φ) for both wavelengths at 10^{14} W/cm^2 in Figs. 5.2(e) and 5.2(f). This modulation is negligible for the lower intensity case. These figures show that the CEP dependence in the yield can indeed be significant. As this CEP dependence cannot modify the directional control over the fragments, we have argued [64] that $\mathcal{A}(E)$ should be normalized by the CEP-averaged yield instead.

The impact of the intensity on the asymmetry goes beyond the magnitude of the effect. It also modifies the asymmetry patterns. In particular, for a given φ and KER in Figs. 5.2(a) and 5.2(c) or in Figs. 5.2(b) and 5.2(d), the sign of the asymmetry may change with intensity, which can lead to cancellation when the incoherent intensity average is carried out.
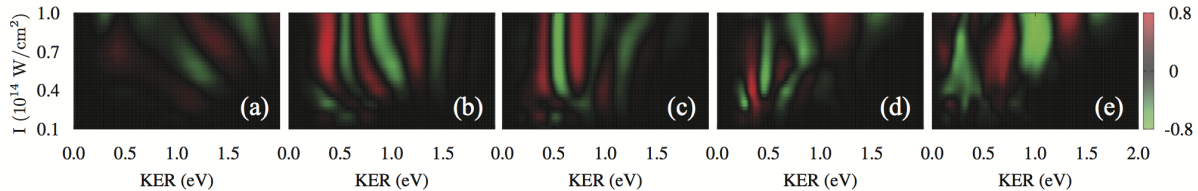
Figure 5.3: *Normalized asymmetry $\mathcal{A}$ as a function of KER and intensity. The initial state is $v = 6$, and all pulses have $\tau_{\mathrm{FWHM}}=3$ cycles and $\varphi = 0$: (a) 800 nm, 7.5 fs; (b) 1000 nm, 9.4 fs; (c) 1200 nm, 11.2 fs; (d) 1600 nm, 15.0 fs; and (e) 2000 nm, 18.8 fs.*

Depending on the geometry of the experiment, the outcome could be drastically different from the result at a fixed intensity.

The intensity dependence must thus be properly taken into account in order to make any kind of realistic prediction or interpretation of experiment. In most calculations to date, however, this has not been the case and only qualitative agreement was sought. Figure 5.2 shows, however, that the only commonality between the intensities is that the CEP dependence has periods of 2π and π for the asymmetry and yield, respectively—e.g., $\mathcal{A}(E) = \mathcal{A}_1 \cos{(\varphi + \varphi_1)}$ and $\mathcal{Y}(E) = \mathcal{Y}_2 \cos{(2\varphi + \varphi_2)}$ to lowest order, where the amplitudes and phase offset are energy dependent. From our photon-phase formalism, Eqs. (3.14) and (3.15) specifically, we see, though, that this periodicity is a completely general result and requires only that an initial parity eigenstate absorbed photons according to the dipole selection rules. It follows that reproducing or predicting this aspect of an experiment says very little useful about the theory in question. Moreover, given Eqs. (3.14) and (3.15), there is no reason to do further theory at this level. Theory should instead be carried out with the important averages performed in order to be scientifically useful. Therefore, we will take intensity into account in the following sections, while we explore any potential advantages of longer wavelengths for CEP control.
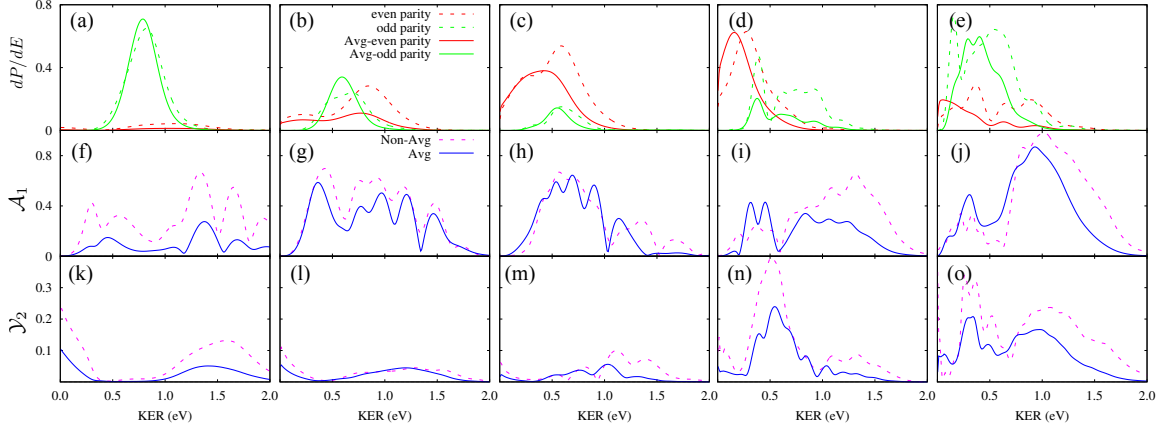
Figure 5.4: *Comparison of intensity-averaged and non-averaged KER spectra, asymmetry amplitude $\mathcal{A}_1$ and yield modulation amplitude $\mathcal{Y}_2$. The peak intensity is $I_0 = 10^{14}$ W/cm^2, and the pulses have $\tau_{\mathrm{FWHM}}=3$ cycles. (a) 800 nm, 7.5 fs; (b) 1000 nm, 9.4 fs; (c) 1200 nm, 11.2 fs; (d) 1600 nm, 15.0 fs; and (e) 2000 nm, 18.8 fs. For all cases, $\varphi = 0$.*

5.1.2 Intensity dependence and intensity averaging

The maximum asymmetry will occur if the phases η_{mJp} of the complex amplitudes C_{mJp} are independent of intensity. In this case, the asymmetry maxima and minima will not shift with intensity, thus minimizing cancellation in the average over intensities in the focal volume. To identify this behavior, we plot the asymmetry for $\varphi = 0$ as a function of KER and peak intensity in Fig. 5.3. From Eq. (3.14), we can see that the behavior at $\varphi = 0$ is representative of all φ since the φ dependence in the phase governing the interference can be separated from the intensity and energy dependence.

The patterns visible in Fig. 5.3 will thus remain at other φ but will be shifted. Plotting $\varphi = 0$ has the added benefit of isolating the phase contribution η_{mJp} of the system-dependent amplitudes C_{mJp}. It is clear from the 800-nm results in Fig. 5.3(a) that the asymmetry structure tilts, whereas for longer wavelengths in Figs. 5.3(b)–5.3(e) they tend to lie more vertically. This vertical structure is ideal for preventing the cancellation due to the variation with intensity.

To demonstrate the impact of this intensity dependence on the experimental outcome, we

apply the intensity-averaging procedure to take into account the variation of intensity in the reaction volume. The exact form of this intensity-averaging depends on the particular geometry of the interaction volume in the experiment which can be characterized as one-, two-, or three-dimensional [137]. Intensity-averaging effects are maximal in the three-dimensional geometries since they have the largest volume of the target exposed to low intensities. By a similar argument, intensity-averaging effects are minimal in one-dimensional geometries. We will consider the intermediate case of a two-dimensional interaction volume as appropriate for the experiment in Ref. [137]. In this experiment, the laser crosses the molecular ion beam at a right angle and has a transverse size much smaller than the ion beam where they intersect. At the same time, the transverse dimension of the ion beam is much smaller than the Rayleigh range of the laser so that the spatial variation of the laser intensity across the width of the ion beam (i.e. the laser propagation direction) can be neglected. For the purposes of intensity-averaging, the interaction volume is effectively two-dimensional, lying in the plane transverse to the laser propagation direction.

We thus assume the intensity in the transverse direction obeys $I(\rho) = I_0 e^{-(\rho/\Delta\rho)^2}$, where ρ designates the radial distance from the axis of the beam and $\Delta\rho$ is the characteristic radius of the beam where it intersects the ion beam. Since we assume $\Delta\rho$ is much smaller than the dimension of the ion beam, its specific value is unimportant as it will contribute only an overall factor to the final averaged quantity. In the normalized asymmetry, it would thus cancel out. Moreover, since most measurements are not absolute, $\Delta\rho$ is not important for the yield either.

But, to compare the intensity-averaged theoretical observables with the unaveraged ones, we normalize by $\pi\Delta\rho^2$ to make the two quantities comparable. Explicitly, the intensity average of some observable $S(I)$ is carried out with the following integral:

$$\begin{aligned}\bar{S}(I_0) &= \frac{1}{\pi\Delta\rho^2}\int_0^\infty S\big[I(\rho)\big]2\pi\rho d\rho \\ &= \int_0^{I_0} S(I)\frac{dI}{I}.\end{aligned} \tag{5.2}$$

In particular, we numerically integrate Eq. (5.2) from a lower limit of 10^{10} W/cm^2 to I_0 with up to 41 points on an exponential intensity grid to obtain convergence to two digits.

Guided by the picture embodied in Eq. (3.14) that mixing even- and odd-parity nuclear partial waves with the same final nuclear kinetic energy gives rise to asymmetric dissociation, we show the even- and odd-parity spectra explicitly in Fig. 5.4 for the cases shown in Fig. 5.3. We compare these observables with the intensity-averaged ones in order to show how significant the averaging effect is. To quantitatively aid this comparison, we also show the amplitude of the asymmetry $\mathcal{A}_1$. Figure 5.4(f), for instance, shows that $\mathcal{A}_1$ at 800 nm decreases by a factor of two to three upon intensity-averaging, just as we anticipated from Fig. 5.3(a). In contrast, the asymmetry for longer wavelengths survives the intensity-averaging with minimal modification as shown in Figs. 5.4(g)–5.4(j) due to the weak dependence of the asymmetry pattern on intensity as shown in Fig. 5.3. At 1200 nm in particular [Fig. 5.4(h)], we found that the maximum magnitude of the asymmetry is essentially unchanged.

Figure 5.4 shows another advantage of longer wavelengths: they tend to permit control at KER where the dissociation probability is large. For example, in Fig. 5.4(h), the strongest asymmetry appears at about 0.5 eV near where the dissociation yield also peaks. Meanwhile, the asymmetry nearly vanishes at the dissociation peak for 800 nm in Fig. 5.4(f). Like Fig. 5.4(h), Fig. 5.4(g) shows relatively strong control near the dissociation peak as do Figs. 5.4(i) and 5.4(j) to some extent. These results are consistent with our photon-phase picture since the $v = 6$ initial state lies 1.25 eV below the dissociation threshold, requiring at least two photons to dissociate for the wavelengths longer than 1000 nm. Therefore, one-photon dissociation is suppressed while multiphoton pathways become more prominent, which leads to stronger interference. This transition from one-photon-dominated dissociation at 800 nm is visible in the KER spectra in Fig. 5.4, keeping in mind that dissociation to even-parity states can only occur with an even number of photons and to odd-parity states with an odd number. Thus, the almost complete lack of dissociation to even-parity states at

800 nm guarantees that the strongest asymmetry lies in the wings of the odd-parity states distribution where the dissociation to both symmetries is comparable. Because multiphoton pathways become more likely for longer wavelengths, the population of the two symmetries becomes more comparable, leading to greater asymmetry.

Intensity-averaging also affects the CEP dependence of the yield, examples of which are shown in Figs. 5.2(e) and 5.2(f). Given the rather large effect it has on the KER spectrum in the first row of Fig. 5.4, especially for longer wavelengths, this is understandable. We show in the last row of Fig. 5.4 the magnitude of the normalized CEP-dependent yield modulation, $\mathcal{Y}_2(E)$, before and after averaging. Like the asymmetry, CEP control over the yield at 800 nm occurs primarily where there is essentially no yield, but shifts towards KER with substantial yield for longer wavelengths. The degree of control also tends to grow with wavelength, approaching 20% modulation even after intensity-averaging. That there is significant yield modulation indicates that pathways differing by two photons (net) must be interfering per Eq. (3.15).

5.1.3 Franck-Condon averaging

From the results so far, it would seem that using longer wavelengths provides a simple way to increase CEP control. These results, however, have been for a single initial vibrational state. Unless one can prepare the ionic target in a particular vibrational level experimentally, the initial vibrational distribution must be taken into account [140]. Hence, we average a given observable S over the initial vibrational states using

$$\langle S \rangle_{\mathrm{FC}} = \sum_v S_v \mathcal{F}_v, \tag{5.3}$$

with $\mathcal{F}_v$ the Franck-Condon factor

$$\mathcal{F}_v = \left| \langle F_v^{\mathrm{H}_2^+} | F_0^{\mathrm{H}_2} \rangle \right|^2, \tag{5.4}$$

in addition to intensity-averaging. The asymmetry is typically reduced by an order of magnitude after both averaging procedures.
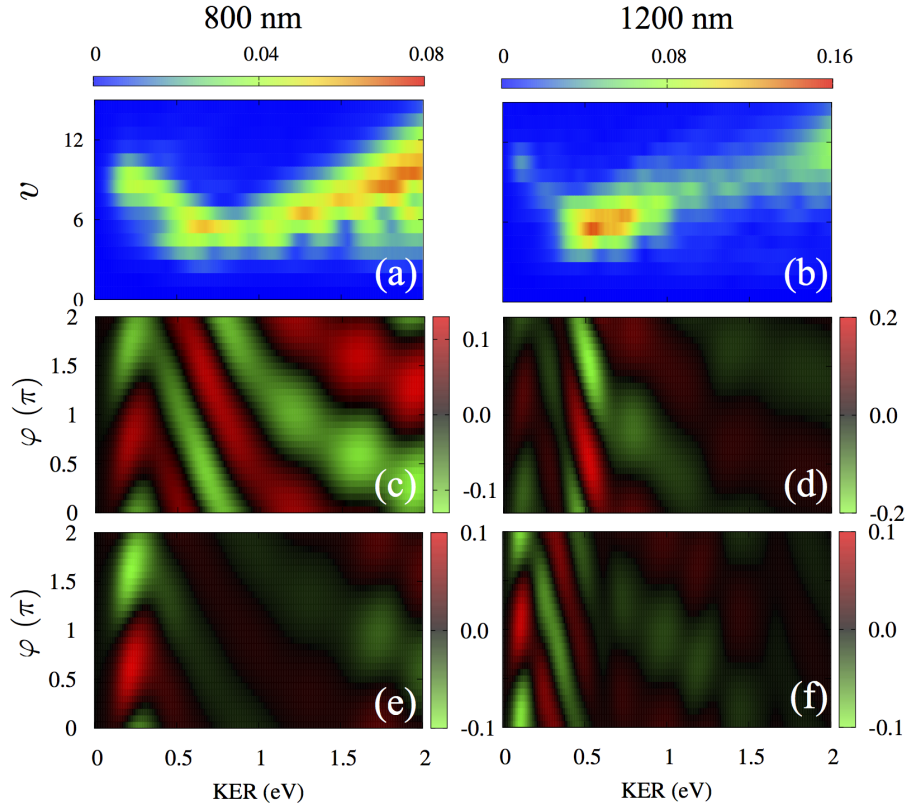
Figure 5.5: *The contribution $\mathcal{C}_v(E)$ of individual vibrational states to $\mathcal{A}$ at 10^{14} W/cm² for (a) 800 nm and (b) 1200 nm. The normalized asymmetry $\mathcal{A}$ including different experimentally important averages for: (c) 800 nm, 7.5 fs, Franck-Condon averaged; (d) 1200 nm, 11.2 fs, Franck-Condon averaged; (e) 800 nm, 7.5 fs, Franck-Condon and intensity averaged; and (f) same as (d) plus intensity average.*

We demonstrate the impact of these averages in Fig. 5.5. The first row quantifies the contribution of each initial vibrational state to the Franck-Condon-averaged $\mathcal{A}(E)$ through the CEP-independent quantity

$$\mathcal{C}_v(E) = \mathcal{F}_v \text{max}\left[\frac{dP_{\text{up}}}{dE} - \frac{dP_{\text{down}}}{dE}\right] \bigg/ \left\langle\frac{dP}{dE}\right\rangle_{\text{FC},\varphi}, \tag{5.5}$$

where $\left\langle\frac{dP}{dE}\right\rangle_{\text{FC},\varphi}$ is the Franck-Condon-averaged and CEP-averaged total yield. These figures show that each vibrational state contributes only over a limited range of kinetic energy. Remarkably, even relatively high vibrational states contribute significantly to the asymmetry for 800 nm, despite their small Franck-Condon factor. Moreover, the asymmetry at 800 nm is due to a wide range of vibrational states. In contrast, the asymmetry for 1200 nm arises nearly entirely from $v = 5$ and 6. Figures 5.5(c) and 5.5(d) show the Franck-Condon-averaged normalized asymmetry. Its magnitude is smaller by about a factor of 3 than $v = 6$ alone (see Fig. 5.2). In addition, the asymmetry patterns change drastically from the $v = 6$ results shown in Figs. 5.2(a) and 5.2(b). The Franck-Condon average is thus on par with the intensity average as a barrier to controlling the spatial asymmetry with CEP. The advantage of longer wavelengths to avoid strong intensity dependence is diluted due to this factor.

5.1.4 Individual photon channels

To gain a deeper understanding of the physics underlying CEP control, we apply the photon-phase representation discussed in Sec. 3.4 more rigorously to the present case. To apply this representation for laser parameters beyond the LOPT regime for more than qualitative understanding requires quantitative knowledge of the photon channels Ψ_m. And, since we have chosen to keep the relative bandwidth fixed in the present study, the pulse energy increases with wavelength at a fixed intensity, taking the system further out of the LOPT regime. For instance, Fig. 5.4(a) shows a clear, single peak in the odd-parity channel corresponding to a net-one-photon transition. As previously noted, however, Figs. 5.4(b)–5.4(e) show that higher-order processes play an increasingly larger role as the even-parity channel grows and even becomes dominant—as expected given that the number of photons

required to dissociate grows. Figures 5.4(b)–5.4(e) also show, though, that there are no clear m-photon KER peaks as might be expected from a simple LOPT picture. Fortunately, Eq. (3.10) gives an exact prescription for extracting the photon channels even well beyond the LOPT regime. One simply needs the final wave function at several CEPs from which ψ_m can be obtained by a Fourier transform.

In Fig. 5.6, the intensity dependence of the individual photon channels is shown, corresponding to the cases of Figs. 5.3(a), 5.3(c), and 5.3(e). Explicitly, we show the quantity

$$\frac{dP_m}{dE} = \sum_J \left| C_{mJp}(E) \right|^2, \tag{5.6}$$

where J is even and $p = g$ if m is even (J is odd and $p = u$ if m is odd).

As expected, one-photon absorption dominates over a wide range of intensities for 800 nm, hence very weak interference arises within 0.5 eV $< E < 1.0$ eV in Fig. 5.3(a). Most of the asymmetry is due to 1ω and 2ω channel interference. Three-photon absorption is significantly weaker since the dissociating wavepacket primarily follows the adiabatic path through the 2ω–3ω crossing to the 2ω channel. This is consistent with the fact that it takes roughly 4.7 fs to travel from the 0ω–3ω crossing to the 2ω–3ω crossing and the pulse is 7.5 fs long. There is thus still sufficient intensity to drive the wavepacket to the adiabatic path.

Meanwhile, the 1200-nm case shows a much weaker one-photon channel since $v = 6$ is below the 1ω channel threshold. Instead, as a consequence of its positioning at the 0ω–3ω channel crossing, the 3ω channel is populated relatively efficiently. Since it takes $\sim$5.9 fs for this wavepacket to reach the 2ω–3ω crossing—and the pulse is 11.2 fs long—it tends to follow the adiabatic path to the 2ω channel. This understanding is consistent with Figs. 5.6(g) and 5.6(h), with the latter showing that only a limited portion of the wavepacket makes it to the 3ω channel. As a result, the strongest interference is between 1ω and 2ω processes as they overlap over a large range of KER for a wide span of intensity.

From Eq. (3.14), we see that the contribution of each pair of photon pathways to the asymmetry can be separately investigated once the photon-phase decomposition of the wave function is known. Accordingly, we decompose the wave function for 1200 nm and plot the
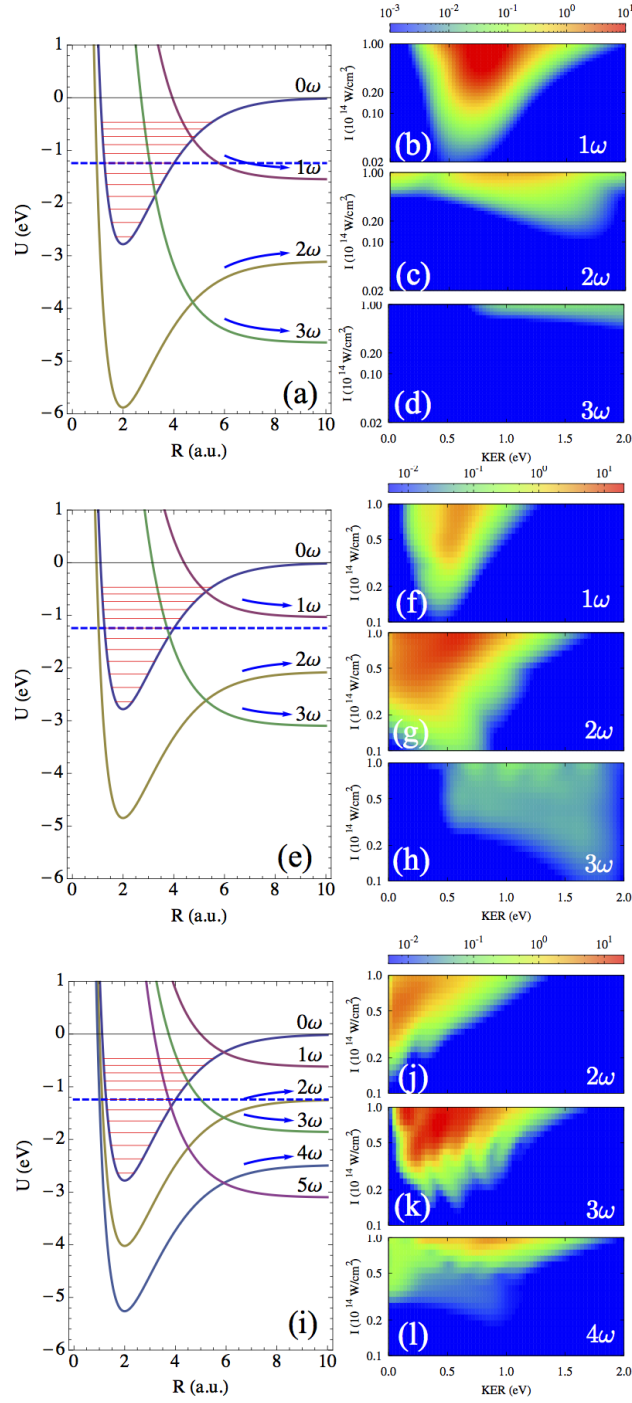
Figure 5.6: *The intensity-dependent KER spectra of individual photon channels dP_m/dE from $v = 6$ (energy marked by the dashed blue line), and the diabatic dressed potentials from Eq. (3.11) for three wavelengths: (a)–(d) 800 nm, (e)–(h) 1200 nm, and (i)–(l) 2000 nm. The most populated channels are indicated with arrows. The corresponding KER spectra follow the same order as the main channels from top to bottom.*

61
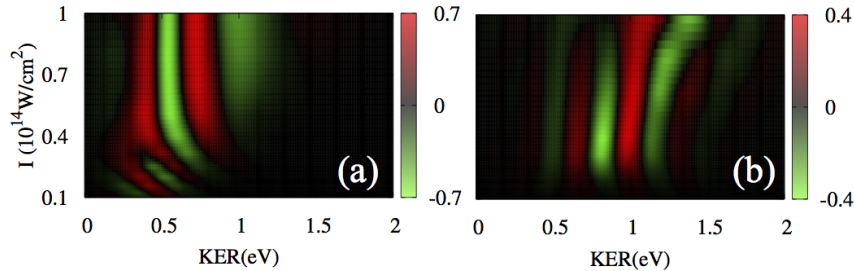
Figure 5.7: *Intensity dependence of the asymmetry constructed from the photon channels explicitly: (a) 1ω–2ω and (b) 2ω–3ω. The laser parameters are the same as Fig. 5.3(c): 1200 nm, 11.2 fs, and $\varphi = 0$.*

interference of 1ω and 2ω pathways in Fig. 5.7(a). We also show the 2ω and 3ω pathway interference in Fig. 5.7(b). These two pathways, however, interfere where the total yield is very small, which makes it a much less significant control effect. Upon comparison with Fig. 5.6, it is clear that the asymmetry patterns in Fig. 5.7 only occur where both channels overlap. Further, the asymmetry in Fig. 5.7(a) is almost a factor of two larger than in Fig. 5.7(b)—which, in turn, is consistent with the total $\mathcal{A}(E)$ in Fig. 5.3(c). Figure 5.7 also shows more detailed information about the phases η_{mJp} than was visible in Fig. 5.3 since it isolates the photon channels. In particular, the oscillation with energy is completely controlled by these phases. Even so, Fig. 5.7 still contains a sum over J that prevents directly seeing this phase.

From the photon-phase picture, one would expect the 2000-nm case to be a good candidate for strong CEP effects since its dissociation automatically involves many photons. Indeed, Figs. 5.6(j)–5.6(l) show that there is substantial dissociation to 2ω, 3ω, and 4ω channels at the highest intensities and that they have a large overlap in energy. The figure also shows that 3ω—the channel populated by the adiabatic pathway—dominates.

While more channels overlapping is generally a plus for CEP effects, when multiple pairs of pathways interfere, the effect can actually be reduced since these pairs need not add constructively. In the 2000-nm case, 2ω and 3ω interfere for KER up to about 1 eV; 3ω

and 4ω interfere for KER in the same range. Although both produce asymmetry with $\cos\varphi$ behavior according to Eq. (3.14), they are not necessarily in phase. Figure 5.3 would seem to suggest that they are, in fact, not in phase since the asymmetry is reduced near 0.5 eV and 10^{14} W/cm^2 where the 2ω and 4ω overlap is greatest. On the other hand, for KER above about 1 eV, where primarily only 3ω and 4ω are involved, the asymmetry is large. Figure 5.7 demonstrates this destructive interference for 1200 nm clearly. At 1 eV, the 1ω–2ω contribution is negative while the 2ω–3ω is positive. Of course, the latter is half the magnitude of the former so that the destruction is not complete.

5.2 Electronic motion in the molecular frame

To visualize the electronic dynamics within the molecule, we can calculate the electron density $\rho(\mathbf{r},t)$ from the total wave function, Eq. (3.2), as

$$\rho(\mathbf{r},t) = \int d^3R \, |\Psi(\mathbf{R},\mathbf{r},t)|^2$$
$$= \int d^3R \left| \sum_{\beta,J} F_{\beta J}(R,t) Y_{J0}(\theta,\phi) \Phi_\beta(R;\mathbf{r}) \right|^2. \tag{5.7}$$

Note that with the restriction to only $\beta{=}1s\sigma_g$ and $2p\sigma_u$ and with $J=0$ initially, $\Omega^{J\pi}_{\Lambda M}$ reduces to a spherical harmonic. Expanding the square and evaluating the integral gives

$$\rho(\mathbf{r},t) = \sum_{\beta,J} \int dR \, |F_{\beta J}(R,t)|^2 |\Phi_\beta(R;\mathbf{r})|^2. \tag{5.8}$$

Recalling that $\mathbf{r}$ is the molecular-frame electronic coordinate, the asymmetry we seek should appear as a function of $\tilde{z}$ where the tilde indicates a molecular-frame coordinate. Given that $|\Phi_{1s\sigma_g}|^2$ and $|\Phi_{2p\sigma_u}|^2$ are even under $\tilde{z} \to -\tilde{z}$, we see that $\rho(\mathbf{r},t)$ displays no asymmetry.

To observe any asymmetry in the electronic density, then, we must also consider the nuclear degrees of freedom. In particular, the integral in Eq. (5.7) must be restricted to a range of θ asymmetric about $\theta{=}\pi/2$. A natural choice is to integrate over the range $0 \le \theta \le \frac{\pi}{2}$, corresponding physically to proton B lying in the upper hemisphere in the laboratory frame whether it is bound or free. The electron may or may not be bound

63

to this proton, so such a quantity does not correspond to the physically observable $p+$H momentum distribution in which an H leaves into the upper hemisphere and a p leaves into the lower hemisphere. Explicitly, the electron density as a function of the molecular-frame $\tilde{z}$ coordinate given that proton B lies in the upper hemisphere in the laboratory frame is ($g \equiv 1s\sigma_g$ and $u \equiv 2p\sigma_u$)

$$\rho(\tilde{z},t) = \frac{1}{2}\int_0^\infty dR \int d\tilde{x}d\tilde{y} \left[\sum_{J \text{ even}} |F_{gJ}(R,t)|^2\,|\Phi_g(R;\mathbf{r})|^2 + \sum_{J \text{ odd}} |F_{uJ}(R,t)|^2\,|\Phi_u(R;\mathbf{r})|^2\right]$$
$$+ \frac{1}{2}\operatorname{Re}\int_0^\infty dR \int d\tilde{x}d\tilde{y}\,\Phi_g(R;\mathbf{r})\Phi_u(R;\mathbf{r})\sum_{\substack{J' \text{ even}\\ J \text{ odd}}} f_{J'J}F_{gJ'}^*(R,t)F_{uJ}(R,t) \quad (5.9)$$

where [1]

$$f_{J'J} = \int_0^{\pi/2} d\theta \int_0^{2\pi} Y_{J'0}^*(\theta,\phi)Y_{J0}(\theta,\phi)d\phi$$
$$= \frac{(-1)^{(J'+J+1)/2}J!J'!\sqrt{2J'+1}\sqrt{2J+1}}{2^{J'+J-1}(J'-J)(J'+J+1)[(\frac{1}{2}J')!]^2\left\{[\frac{1}{2}(J-1)]!\right\}^2}. \quad (5.10)$$

The time-dependent behavior of the electron in the field is revealed by plotting Eq. (5.9) in Fig. 5.8. Before the pulse hits the molecule, the electron is distributed in the molecular frame evenly as required by the symmetry of the bound eigenstate. As the field strength rises, the field drives the electron towards the opposite direction. Because the electron becomes localized in one of the nuclei, the molecular bond is softened and molecule starts to dissociate. The localization of the electron gradually fades away as the field declines. Eventually the probability density splits into two branches, corresponding to dissociative and bound parts. In either part, the distribution appears to be fairly symmetric. This should not be surprising because the majority of the wavepacket dissociates through a single photon transition and ends in the $2p\sigma_u$ channel. The asymmetry comes from a small fraction of the

---

[1]The factorials for high J are fairly inconvenient to evaluate numerically. It is better to rearrange the expression as

$$f_{J',J} = \frac{\sqrt{2J'+1}\sqrt{2J+1}(-1)^{(J'+J+1)/2}J}{(J'-J)(J'+J+1)}\prod_{i=1}^{\frac{1}{2}J'}\left(\frac{J'+2i}{8i}\right)\prod_{j=1}^{\frac{J-1}{2}}\left(\frac{J-1+2j}{8j}\right)$$
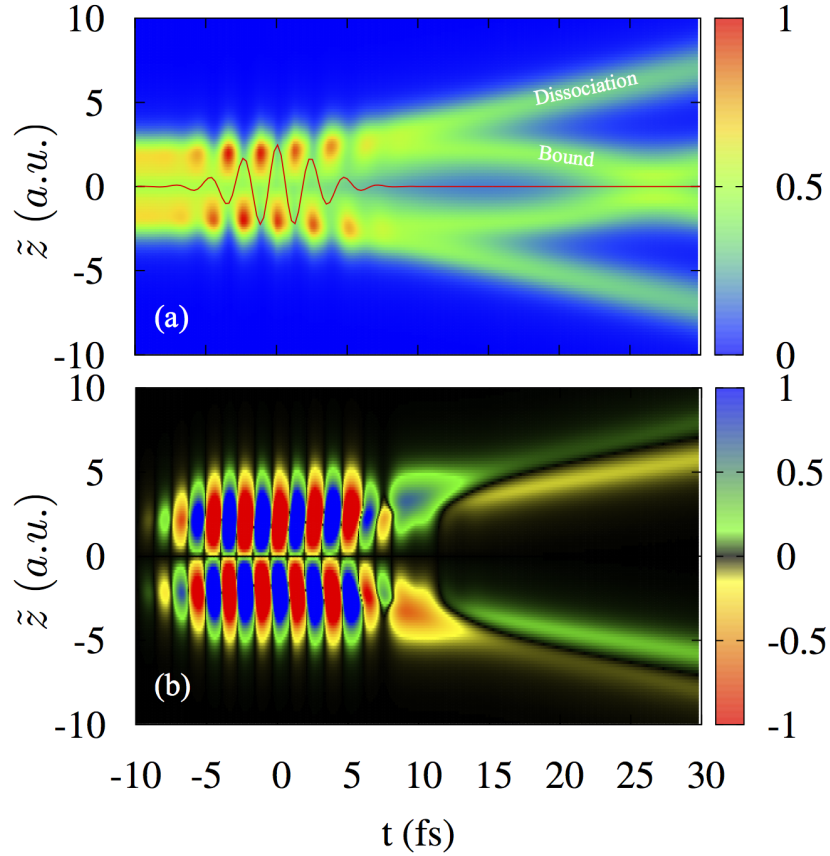
Figure 5.8: *(a) An electronic probability density plot in the molecular frame $\rho(\tilde{z}, t)$ retrieved from the TDSE calculation for a 4.5 fs Gaussian pulse of 800 nm wavelength at the intensity $1 \times 10^{14} \text{W/cm}^2$ (inset: red curve) interacting with the initial state $v = 8$, $\varphi = 0$. For simplicity, we use the linear combination of atomic orbitals to represent the adiabatic electronic wave functions (see Appendix. A). (b) is the same plot but shows only the asymmetric term in Eq. (5.9). The probability density in both plots is renormalized.*

dissociative wavepacket, which corresponds to the second term in Eq. (5.9). We therefore plot this term separately to emphasize its contribution. In Fig. 5.8(b), the asymmetric yield oscillates with the laser frequency during the presence of the field. The non-oscillating asymmetric yield takes place at about $t = 15$ fs, where the field essentially vanishes. From then on, the asymmetry near the center becomes absent since there is no overlap of $1s\sigma_g$ and $2p\sigma_u$ in the bound wavefunction.

5.3 Summary

To summarize, we carried out full-dimensional calculations for H_2^+ interacting with few-cycle laser pulses of various wavelengths in the mid-infrared regime. With the numerical examples and their photon-phase analysis, we explicitly show CEP effects as an interference of multiple photon channels overlapped in the same energy range, which permits a deeper understanding of the CEP control—both at a quantitative and qualitative level.

Comparing with Ti:Sapphire laser wavelengths, longer wavelengths tend to suppress the single-photon absorption and enable higher-order pathways to interfere with large magnitudes. The weak intensity dependence of these long-wavelength, high-order channels helps preserve the CEP-dependent asymmetry when the intensity average over the interaction volume is taken into account.

Long wavelengths are not, however, immune to the reduction in control resulting from Franck-Condon averaging. Where such averaging is appropriate, control over asymmetry can be substantially reduced. Our results thus reinforce the fact that any nontrivial comparison with experiment should include all averages inherent to the experiment. Of these, intensity and Franck-Condon are the most significant, but could also include thermal averaging as well as averages over uncertainties or drifts in the laser parameters. Since weak intensity dependence of the photon channels cannot be expected for a general system, the surest route to greater CEP control is to eliminate or limit all of the averages we have discussed. Moreover, if specific pairs of photon channels could somehow be selected, then their generally destructive interference could be avoided.

Chapter 6

Quantitative comparison with experiments

6.1 Introduction

Carrier-envelope phase effects have been proposed as a general control mechanism theoretically [93] and a multitude of experiments have successfully demonstrated its control capabilities and universality. These include modulating the photoelectron spectra of gaseous atoms and molecules [36–39, 47] as well as nanoparticles [49, 50], and the spatial asymmetry of dissociation fragments in diatomic [1, 2, 75–81, 86, 91] and polyatomic molecules [48, 83]. The carrier-envelope phase is also found to be effective in manipulating high-order harmonic generation spectra [55–61]. Given the potential of CEP control, a good agreement in a quantitative comparison between theory and experiment for a benchmark system is important for confirming our understanding of the underlying physics. Moreover, such agreement would indicate the mastery over laser pulse generation and characterization needed to realize the promise of CEP control. Importantly, measurements of CEP effects in the theoretically accessible H_2^+ molecule have recently been carried out [1, 2], permitting precisely these kinds of comparisons.

Even for the simplest system, however, a quantitative side-by-side comparison of theory and experiment is lacking in the literature to date. Such a comparison needs to take a multitude of aspects into consideration. First, a direct comparison to measurements,

which is mostly based on the momentum distribution of the fragments, requires theory to be evaluated in full dimensions. In spite of this , reduced-dimension models seem to be the norm for such comparison. Second, measurements collect fragments from throughout the whole volume of the laser-target overlap. Since the intensity of the laser varies over this volume, intensity averaging of the theory is crucial for comparison to experiments. Third, all theoretical calculations for strong-field processes have errors of various sorts. Yet, careful assessment of such errors—and identifying the resulting theoretical error bars—are very rarely presented in the literature. Any quantitative comparison between theory and experiment, must, however, include these errors. Fourth, accurate measurement of the laser pulse itself is very difficult. especially for the few-cycle pulses needed for CEP experiments. Consequently, theory often has no choice but to see a simple approximation to the pulse such as a Gaussian. Few-cycle pulses are rarely Gaussian, and the deviations from Gaussian can have non-trivial impacts. These are just some of the issues that affect comparison of theory with experiment.

In this collaborative work, we will address these concerns for photodissociation of H_2^+ by a few-cycle pulse, and provide a quantitative comparison between our theory and experiments, following up on the work reported in Refs. [1, 2] and providing further details and analysis. The two experiments used similar laser parameters: a peak intensity of about 4×10^{14} W/cm^2, a pulse duration of about 4–5 fs, and a central wavelength of about 700 nm. The CEP was measured shot-by-shot with a phase-tagging technique [27, 141].

The crucial aspect of both experiments that make them suitable for benchmark comparisons with theory is that the target is H_2^+ provided as a beam from an ion source. In contrast to similar experiments with H_2—having an ion beam target removes the need to model the strong-field ionization step. Consequently, it also removes a major source of uncertainty since an accurate treatment of this step is not available. At the same time, H_2^+ can be treated very accurately theoretically [102]. Together, these factors provide a ideal opportunity to achieve our goal of quantitative agreement between theory and experiment. Admittedly, we

treat electronic dynamics within the Born-Oppenheimer representation, where ionization is ignored. However, given full-dimensional simultaneous treatment for electron and nuclei are not available, we consider worthwhile to adopt the Born-Oppenheimer approach towards its limits.

While the vast majority of theoretical and model treatments of CEP effects in H_2^+ dissociation (or H_2 dissociative ionization) include only the lowest two electronic states, the excited states and ionization play an increasingly larger role as the intensity increases. This result is, of course, easy to understand, but must be taken into account for any quantitative comparison with experiments at intensities higher than roughly 10^{14} W/cm^2 for few-cycle pulses at 800 nm. In fact, we find that ionization—which we neglect [102, 107]—provides the largest contribution to our theoretical error bars at the highest intensities we consider. We also find that using a pulse that more closely resembles the experiment changes the theoretical asymmetry significantly. Overall however, we do not find satisfactorily good quantitative agreement given the relative simplicity of this system. We thus devote some discussion to possible explanations of the discrepancies.

6.2   Observables for comparison with experiment

We evaluate the momentum distribution from Eq. (3.6). In such expression, we include only the $1s$ fragments, because the contribution of $n \geq 2$ is only a small correction over a significant range of laser parameters. Consequently, as we discuss below, we will use the $n \geq 2$ channels to help estimate our theoretical error bars. While we can readily include $n \geq 2$ channels in the TDSE, evaluating $\langle \mathbf{K}, nlm|$ for $n \geq 2$ poses some technical challenges (see Ref. [142] for the discussion of the induced-dipole states in the asymptotically degenerate H($n \geq 2$) manifolds). Given their generally small contributions, we chose not to implement the analysis for these states at this time. We can, however, estimate the total kinetic energy release (KER) spectra for these channels since the exact $\langle \mathbf{K}, nlm|$ is not then
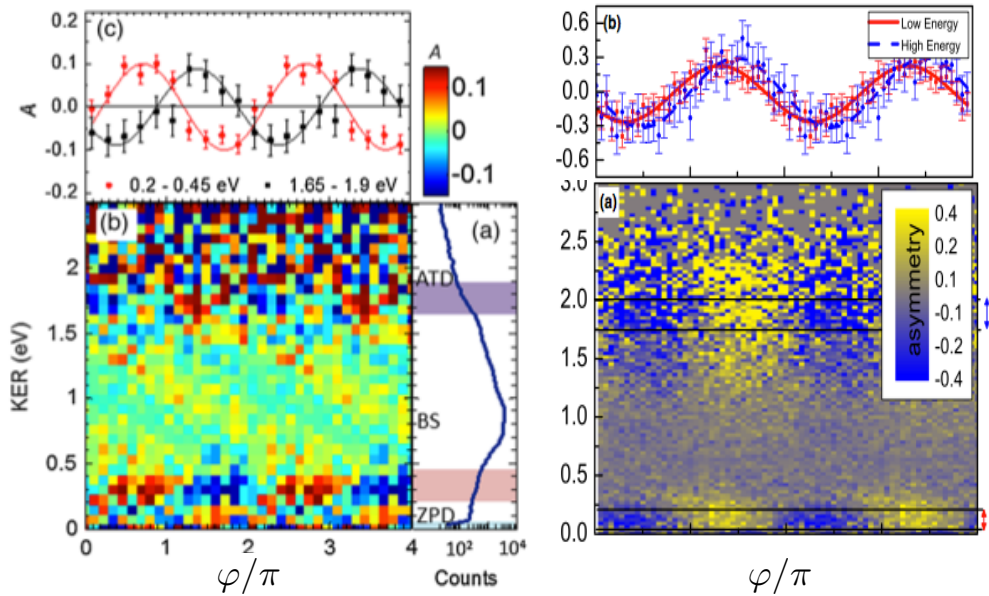
Figure 6.1: *Measured asymmetry as a function of KER and CEP adapted from Refs. [1, 2]. are shown in left (EXP1) and right panels (EXP2), respectively. The top panels are the integrated asymmetry in the high and low KER region as a function of CEP. The low and high KER regions is defined as LE (0.2–0.45 eV) and HE (1.65–1.90 eV) in EXP1, LE (0–0.20 eV) and HE (1.75–2.0 eV) in EXP2, respectively.*

needed. Specifically, since the KER spectrum for a particular electronic channel β is

$$\frac{dP_\beta}{dE} = \sum_J |C_{J\beta}|^2. \tag{6.1}$$

We do not need an accurate scattering phase shift $\delta_{J\beta}$. All that we need is a properly energy-normalized state $\langle EJ\beta|$ which can be obtained by matching a numerical solution to any pair of linearly independent, energy-normalized functions—we used spherical Bessel functions. Since this approach does not use the correct asymptotic functions for matching, it cannot give the correct $\delta_{J\beta}$. Moreover, our $\langle EJ\beta|$ calculated neglecting the non-Born-Oppenheimer present for $n \geq 2$, thus providing approximate KER spectra for these channels. We expect this to be a rather good approximation, however, and more than adequate for estimating our errors—which is their primary use. We will return to this point below.

As already mentioned, the key parametrization of CEP effects in our measurement is

the normalized spatial asymmetry,

$$\mathcal{A}(E) = \left(\frac{dP_{\text{up}}}{dE} - \frac{dP_{\text{down}}}{dE} \right) \bigg/ \left(\frac{dP_{\text{up}}}{dE} + \frac{dP_{\text{down}}}{dE} \right). \tag{6.2}$$

In this expression, the up and down KER spectra are defined within a cone of θ_0 around the polarization direction:

$$\frac{dP_{\text{up}}}{dE} = \int_0^{\theta_0} \frac{\partial^2 P}{\partial E \partial \theta_K} \sin \theta_K d\theta_K,$$
$$\frac{dP_{\text{down}}}{dE} = \int_\pi^{\pi-\theta_0} \frac{\partial^2 P}{\partial E \partial \theta_K} \sin \theta_K d\theta_K. \tag{6.3}$$

The values of θ_0 were chosen in each experiment to improve data quality, and the same θ_0 were used for the theoretical comparison.

Given the $n \geq 2$ contribution as well as ionization are absent from the analysis $dP_{\text{up/down}}/dE$, We consider there exists an uncertainty $dP_{n=2}/dE$ in $dP_{\text{up/down}}/dE$. Then the propagated error in $\mathcal{A}$ is

$$\Delta_{\mathcal{A}} = 2\frac{dP_{n=2}}{dE} \frac{\sqrt{\left(\frac{dP_{\text{up}}}{dE}\right)^2 + \left(\frac{dP_{\text{down}}}{dE}\right)^2}}{\left(\frac{dP_{\text{up}}}{dE} + \frac{dP_{\text{down}}}{dE}\right)^2}. \tag{6.4}$$

In Eq. (6.4), we do not expect the value of $\Delta_{\mathcal{A}}$ critically depends on θ_0, then $dP_{\text{up/down}}/dE$ can be evaluated for $\theta_0 = \pi/2$ so that they count the total probability from the both hemispheres. In this case, the uncertainty in $dP_{\text{up/down}}/dE$ should be reasonably captured by the $n = 2$ contribution. By monitoring this error, we can quantify the accuracy of our method. Note that all the absolute quantities, such as $dP_{\text{up/down}}/dE$, are Franck-Condon averaged by Eq. (5.3) and intensity averaged by Eq. (5.2) in order to compare to the experiments.

6.3 Results and discussion

The goal of performing the experiment on the simplest molecule H_2^+ is that we have some confidence that accurate theoretical calculations can be carried out, at least for dissociation [102]. Given this expectation, the agreement between theory and experiment in

Refs. [1, 2] was rather disappointing. Among the various possible sources of disagreement, we consider here the two that we expect to have the largest impact.

6.3.1   High intensity

One of the largest sources of disagreement between theory and experiment in Refs. [1, 2] is the fact that the maximum intensity in the theory was limited to 1×10^{14} W/cm^2 while the experiments were carried out at mid-10^{14} W/cm^2 intensities. The reason for this limitation was already mentioned, the neglect of ionization in the calculation. Although the ionization fraction was measured to be about 0.3% in EXP1 and less than 3% in EXP2, the impact on the theory is almost certainly much larger. Aside from the fact that these fractions in the intensity averaging, they are the fraction that remained in the ionization channels after the pulse was gone. During the pulse, however, the population of the ionization channels in the wave function expansion Eq. (3.2) could be 10 times bigger—and thus could have a significant effect on the dynamics, even in the dissociation channels.

Although no one has yet performed a full-dimensional calculation for H$_2^+$ in a strong field including vibration, rotation, and ionization, we can estimate the ionization by extending our own calculations to excited electronic manifolds and using their population as a proxy for ionization as described in detail in Sec. 6.2. To give a sense of the impact of the excited manifolds, we show in Fig. 6.2 the normalized spatial asymmetry $\mathcal{A}(E)$ calculated with $n_{\max} = 1$ and $n_{\max} = 2$. In the latter case, both manifolds were included in the TDSE, but only $n = 1$ was included in the analysis (see Sec. 6.2). A Gaussian pulse was used with the parameters determined from a fit to the experimental pulses, and the asymmetries include both Franck-Condon and intensity averages. The peak intensities are well into regime where the ionization channels should play an important role. Indeed, we will show below that the error bars for Fig. 6.2 are large.

While the calculations with $n_{\max} = 1$ and $n_{\max} = 2$ show similar patterns, there are clear differences—notably, the asymmetry is generally larger for $n_{\max} = 2$. With or without
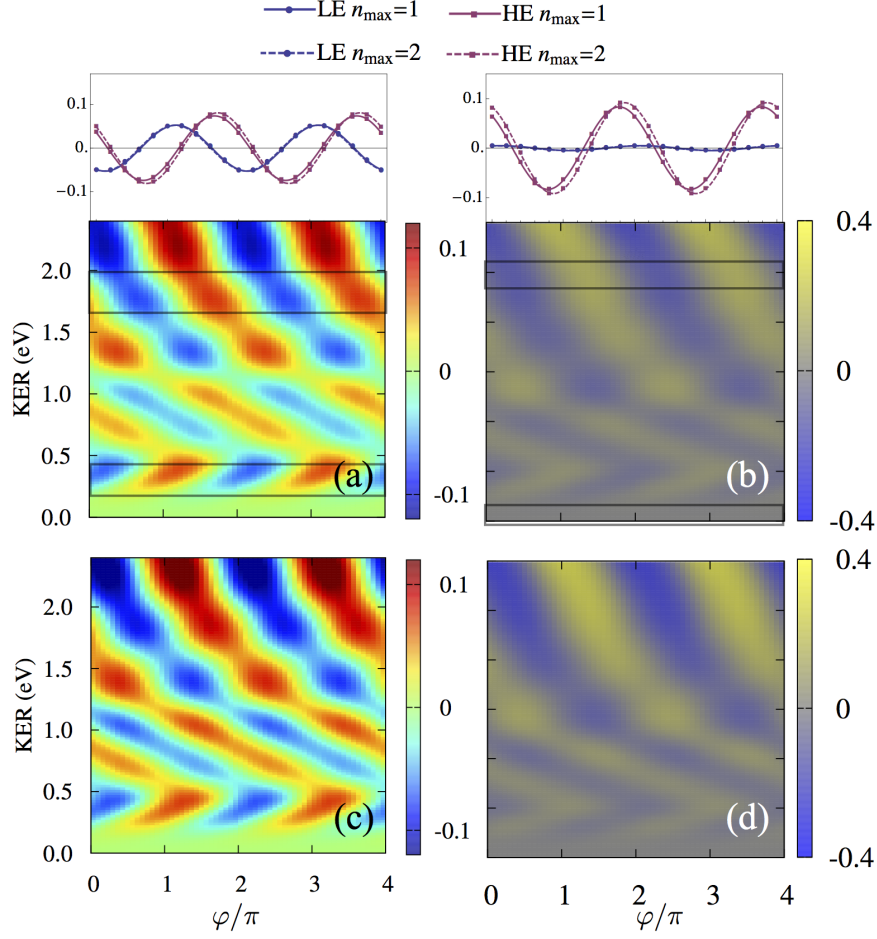
Figure 6.2: *FC-averaged intensity-averaged asymmetry map calculated based on a Gaussian pulse for both EXP1(left column) and EXP2(right column). The laser parameters are $I_0 = 4 \times 10^{14}$ W/cm^2, $\tau_{\text{FWHM}} = 5$ fs, $\lambda = 730$ nm for EXP1 and $I_0 = 4 \times 10^{14}$ W/cm^2, $\tau_{\text{FWHM}} = 4.5$ fs, $\lambda = 700$ nm for EXP2. The first row are the calculation with $n_{\text{max}} = 1$ and the second row are the ones with $n_{\text{max}} = 2$. The sub-panels on top of the asymmetry plots are the integrated asymmetry in the ranges defined in Fig. 6.1.*

$n = 2$, however, the asymmetry oscillates in the CEP with a period of 2π, as it must. As proven in general in Refs. [64, 93], stemming from the interference of even and odd-parity states required to break spatial symmetry. This periodicity would thus apply no matter how many manifolds—features of $\mathcal{A}(E)$ are thus the amplitude and phase in Fig. 6.2 are similar suggests the corresponding amplitudes and phase offsets are not dramatically altered by the inclusion of $n = 2$ for these laser parameters. However, since the momentum analysis of
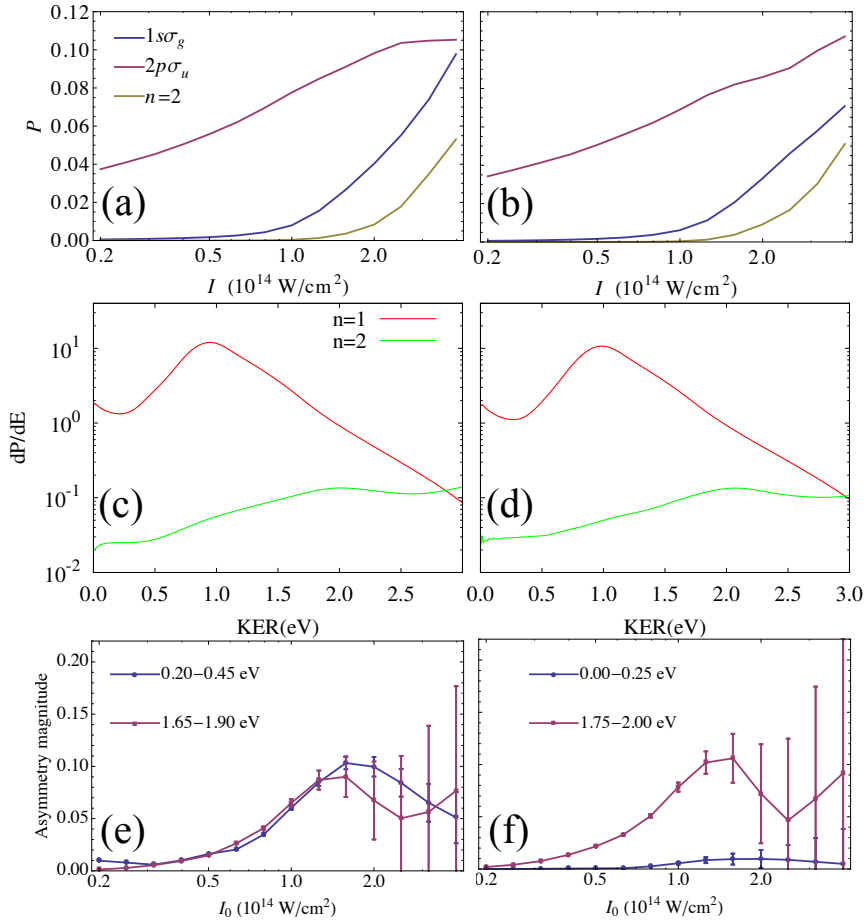
Figure 6.3: *(a)–(b) is the dissociation probability as a function of intensity I; (c)–(d) are the KER spectra at the intensity of $I_0 = 4 \times 10^{14}$ W/cm^2; (e)–(f) Amplitude of the integrated asymmetry as a function of peak intensity I_0 (intensity-averaged) in the low and high KER region with error bars defined in Eq. (6.4). Left and right column are for EXP1 and EXP2, respectively.*

$n = 2$ is absent in our study, the full effects of $n = 2$ on $\mathcal{A}(E)$ cannot be assessed.

To better understand the impact of the $n = 2$ manifold, we investigate other observables. In particular, the population of $n = 2$ grows considerably at high intensities as shown in Figs. 6.3(a)-(b). Note that these figures do not include intensity averaging. At the highest intensity, 4×10^{14} W/cm^2, the $n = 2$ channels account for 20.7% and 22.3% of the total yields for EXP1 and EXP2, respectively, which is clearly not negligible. Moreover, it strongly

suggests that $n_{\text{max}} = 2$ is insufficient at these intensities. After intensity averaging, the fraction of dissociation to $n = 2$ drops to 5.6% and 5.8% for EXP1 and EXP2, respectively. Although much smaller, dissociation to $n = 2$ is still not negligible, but it will drop quickly with decreasing intensity as suggested by Figs. 6.3(a) and 6.3(b).

Dissociation via n=2 typically leads to higher KER than from $n = 1$ as shown in Figs. 6.3(c) and 6.3(d). These figures show the intensity- and FC-averaged KER spectra of each manifold at the peak intensity $I_0 = 4 \times 10^{14}$ W/cm^2. For most KER, $n = 2$ contributes only a negligible fraction to dissociation. Only at energies beyond about 2.5 eV does $n = 2$ contribute comparably to $n = 1$. As Fig. 6.2 shows, however, the inclusion of $n = 2$ influences the $n = 1$ wave function even at low energies. Therefore, it is not necessary for the final populations to be large to have an impact on the results, making any estimate of the errors from excluding channels difficult.

In Figs. 6.3(e) and 6.3(f), we show the normalized spatial asymmetry integrated over the KER cuts chosen in the experiments for a range of peak intensities along with the theoretical error bars defined in Sec 6.2. The magnitude of the asymmetry initially grows with peak intensity as expected, but actually decreases in each case for a range of peak intensities. While this behavior is not anticipated by the simple pictures for CEP effects, it should also be noted that the error bars grow with intensity, especially for the high-KER cut. So, whether the non-monotonic behavior in Figs 6.3 is real or due to the limitations of our current calculations remains to be forthcoming without a full-dimensional solution of the TDSE for H$_2^+$ including vibration, rotation, and ionization. Alternatively, the answer could come from an intensity scan in the experiment, but such an experiment still poses non-negligible challenges.

Comparison of the theory from Fig. 6.2 with the experiment in Fig. 6.1 shows some similarities but also clear differences. The notable similarities—aside from the trivial 2π periodicity— are the overall pattern of the asymmetry with the low-energy change in the "tilt" of the pattern at roughly the right energy. The outstanding difference is the de-

pendence of the asymmetry's magnitude on energy. Both experiments show a significant suppression of the asymmetry for the middle range of energies, roughly $0.5 - 1.5$ eV, compared to theory. So, while the comparison with experiment has improved from Refs [1, 2] by increasing the intensity—primarily by increasing the magnitude of the asymmetry— key aspects of the experiment remain unexplained.

6.3.2   Realistic pulses

Since our calculations in Fig. 6.2 miss some significant qualitative features of the experiment, despite increasing the intensity in the theory, we seek the next most likely source of disagreement. After the truncation of the wave function expansion in Eq. (3.2), the biggest approximation in the theory for Fig. 6.2 is treating the laser pulse as Gaussian. The deviation of the pulse from Gaussian was already addressed to some extent in Ref. [2] by using measured properties of the actual experimental laser pulse. We will extend and expand that discussion here.

Essentially all calculations of CEP effects to date have used a simple time-domain definition of the CEP equivalent to ours in Eq. (2.1). In fact, many have not used a pulse as realistic as a Gaussian. But, since many calculations have been for reduced-dimensional models seeking simple qualitative behavior, there has been little incentive to do better. And, even should a more accurate pulse have been sought, measuring a few-cycle pulse accurately is itself a non-trivial task. Yet we know that few-cycle pulses are most likely to deviate from the idealized Gaussian. For the present case, the spectral information measured is shown in Figs. 6.4(c) and 6.4(d) along with the corresponding time-dependent electric fields in Figs. 6.4(a) and 6.4(b). In EXP1, only the power spectrum was measured, so $\mathcal{E}(t)$ was contracted assuming a flat phase; in EXP2, the phase was also measured using spectral-phase interferometry for direct electric-field reconstruction(SPIDER) [45] and thus was used to construct $\mathcal{E}(t)$. Explicitly,

$$\mathcal{E}(t) = \int_{-\infty}^{\infty} \sqrt{I(\omega)} e^{-i[\omega t + \phi(\omega)]} d\omega, \tag{6.5}$$
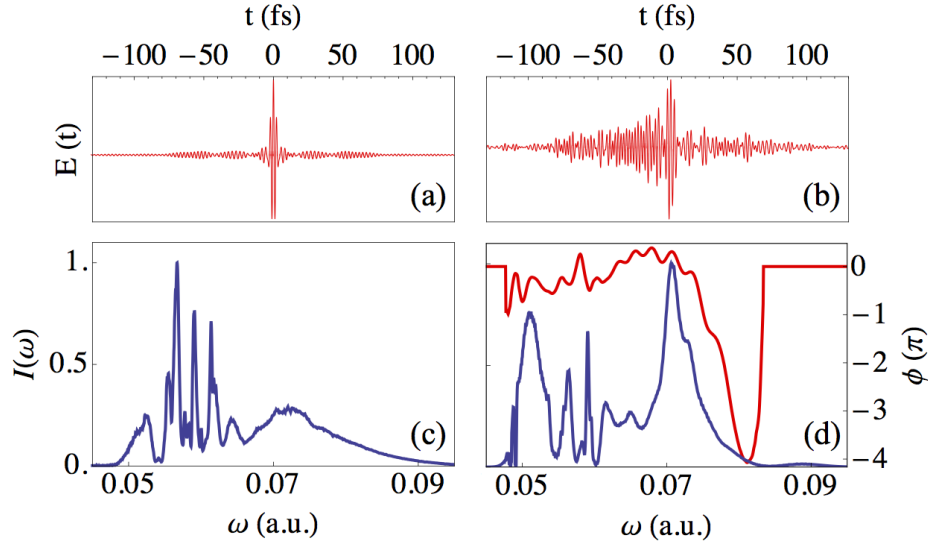
Figure 6.4: *(a) The instantaneous field, (c) the measured pulse spectrum for EXP1; (b) and (d) are the same quantities for EXP2;.*

where the power spectrum $I(\omega)$ is mirrored to negative frequencies with the spectral phase $\phi(-\omega) = -\phi(\omega)$ to ensure that the instantaneous field is real.

The real spectrum noticeably deviates from a commonly presumed smooth Gaussian, which appears to undermine the features of a few-cycle pulse and sabotage the CEP control effects. However, in Fig. 6.5, the calculations with realistic pulse spectra are shown and display no less asymmetry compared to the ones shown in Fig. 6.2. This is exactly what Ref. [143] pointed out, that it is the relative bandwidth of the pulse that determines the observability of CEP effects, not the temporal length of the pulse. Therefore, the noise-like long pulse does not necessarily have a negative impact on CEP control. As long as the relative bandwidth of the pulse is reasonably large, allowing the system to absorb multiple photons from the wide range of the spectrum and end up in the same energies, the CEP effects should remain. On the other hand, given the fact that a Gaussian pulse mathematically possesses the minimum uncertainty under the transformation between the temporal and frequency domain, any form that deviates from a Gaussian but with a similar temporal envelope must have a wider range in the frequency domain to compensate. In other words,
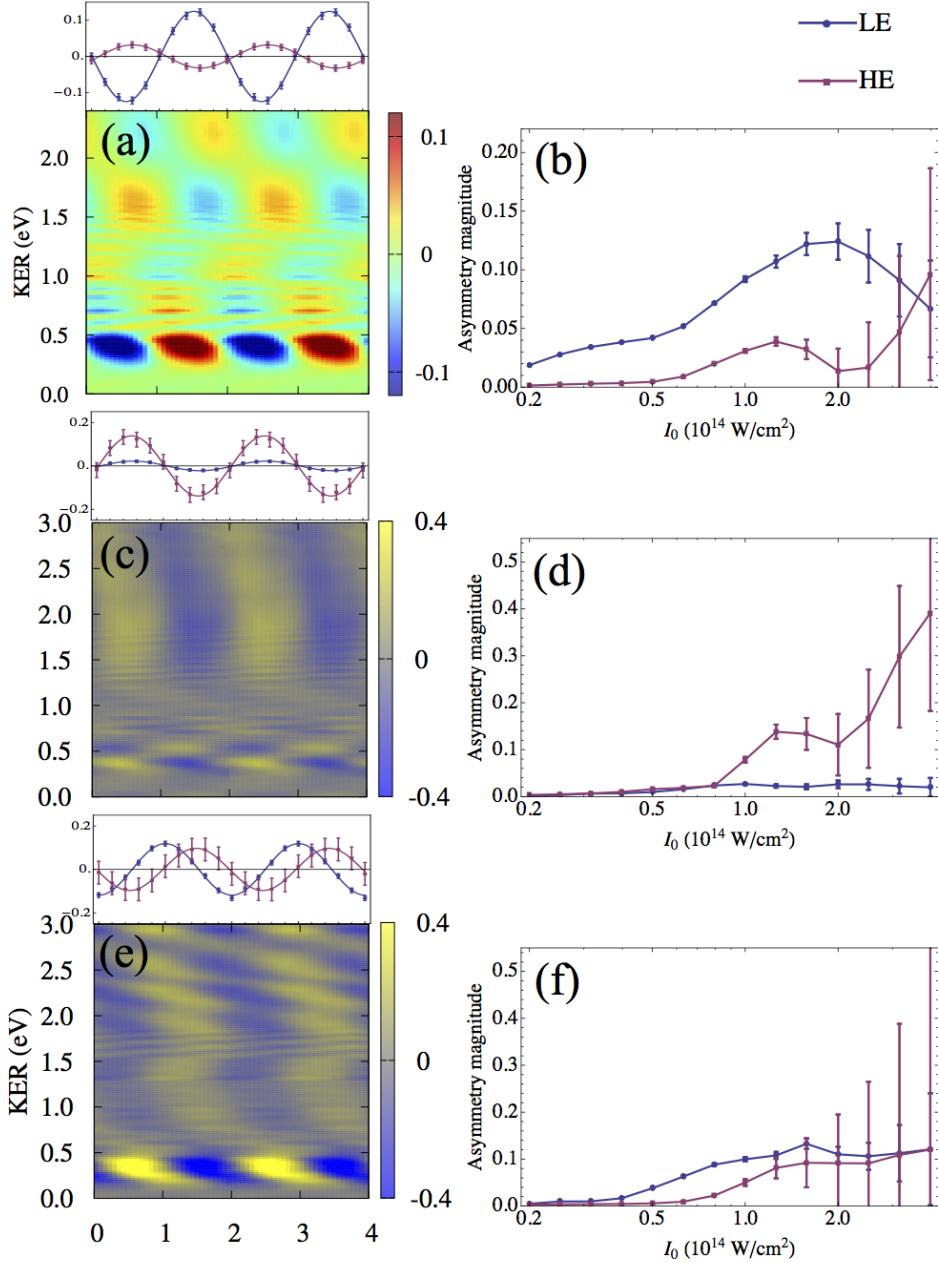
Figure 6.5: *(a),(c) and (e) are the asymmetry map calculated with the spectral information provided at $I_0 = 1.6 \times 10^{14}$ W/cm². On their right side are the amplitude of the integrated asymmetry in the low and high KER region as a function of I_0. (a)–(b) are for EXP1 calculated with a pulse Fourier-transformed from the spectrum in Fig. 6.6(a); (c)–(d) are for EXP2 calculated from a pulse Fourier-transformed from the spectrum in Fig. 6.6(b) without the spectral phase, (e)–(f) with the spectral phase.*

the effective bandwidth of these realistic pulses must be larger than the Gaussian pulses with similar temporal profiles, which typically means it is more advantageous for CEP effects. For either comparison, Gaussian vs. realistic pulse or transform-limited vs. full spectral pulse in Fig. 6.2 and Fig. 6.5, we know that the asymmetry patterns are sensitive to both the power spectrum and the spectral phase, although it is difficult to characterize this sensitive dependence. Empirically, the pulse with a spiky spectrum tends to straighten the asymmetry stripes, compared to the Gaussian calculation, which seems to be a poorer representation of the measurements.

As seen in Fig. 6.4, the Gaussian approximation fails to capture salient features of each measured pulse-namely, the significant pre-pulses, post-pulses, or pedestals. These features result, of course, from the combination of the sharp structures in the pulse spectrum and the spectral phase.

The effect of the pre-pulses and pedestal can be understood in part by using the results from Ref. [69]. There, it was shown that using a pump pulse to prepare H_2^+ before exposing it to a few-cycle pulse could greatly enhance the CEP-induced spatial asymmetry. The enhancement was understood to be a consequence of depleting the higher-lying vibrational states and aligning the lower-lying vibrational states with the pump pulse. We have found that the pedestal and pre-pulse fulfill a similar role as the pump pulse from Ref. [69]. To demonstrate, we show the bound-state alignment parameter $\langle \cos^2 \theta \rangle$ in Figs. 6.6(a) and 6.6(b) and the bound-state population P_b in Figs. 6.6(c) and 6.6(d). In these figures, we group the initial states as low-lying ($v = 0$–7) and high-lying ($v = 8$–19) as we expect their behavior to be different per Ref. [69]. The observables are Franck-Condon averaged with each group as

$$\langle P_b \rangle_{\mathrm{FC}} = \frac{\sum\limits_{v} \mathcal{F}_v P_{bv}}{\sum\limits_{v} \mathcal{F}_v},$$

$$\langle \cos^2 \theta \rangle_{\mathrm{FC}} = \frac{\sum\limits_{v} \mathcal{F}_v P_{bv} \langle \cos^2 \theta \rangle_v}{\sum\limits_{v} \mathcal{F}_v P_{bv}}. \tag{6.6}$$

In these expressions, the sum over v only includes those states within each group.

The high-lying group dissociates primarily via net-one-photon transitions while the low-lying group requires more net photons. The high-lying group is thus more likely to be dissociated by the pedestal and pre-pulses, as seen in Figs. 6.6(c) and 6.6(d). In fact, Fig. 6.6(d) with its more significant pre-pulses shows nearly 20% dissociation by about -80 fs nearly 80% dissociation by the nominal beginning of the few-cycle pulse. But, since net-one-photon transitions produce only a single parity, their dissociation is largely symmetric. While the low-lying group is mostly not dissociated by the pedestal and pre-pulses — Figs. 6.6(c) and 6.6(d) show less than 10% dissociation by the nominal beginning of the pulse —, it is aligned by then. As Ref. [69] showed, aligned low v's dissociate more and produce larger asymmetry since they produce both parities. Figure 6.6(b) does indeed show strong alignment with its substantial pre-pulse: $\langle \cos^2 \rangle$ has increased to roughly 0.5 by the beginning of the few-cycle pulse. With its weaker pre-pulse, Fig. 6.6(a) show almost no alignment, however.

This observation can be made more clear by monitoring individual states contribution. Since the initial states obey Franck-Condon distribution and contribute the total asymmetry incoherently, the unnormalized asymmetry can be decomposed to individual component. We therefore use the contrast parameter $\mathcal{C}_v$ given by Eq. (5.5) to quantify the contribution from different initial vibrational states. Given that EXP2 provides more complete characterization of the pulse, we choose it as the showcase to demonstrate spectral effects. In Fig. 6.7(b–d), we compare $\mathcal{C}_v$ in the calculations with three different pulse characterizations: (1) a Gaussian pulse as used in Fig. 6.2(b); a pulse (2) Fourier transformed from only the power spectrum and (3) with both power spectrum and phase. All results are intensity-averaged up to $I_0 = 1.6 \times 10^{14}$ W/cm^2 because the error bars beyond are intolerable. Figure 6.7(b), corresponding to the Gaussian case, shows that the asymmetric yield in the low KER region is mostly attributed to the vibrational states $v = 7$–10, while the asymmetric yield in the high KER region is attributed to $v = 3$–12 fairly evenly. On the
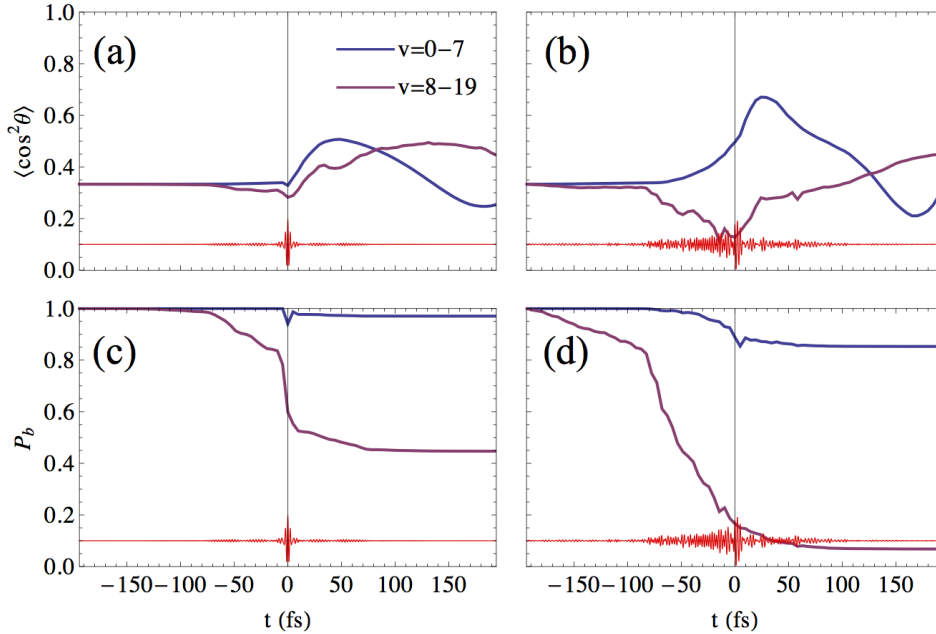
Figure 6.6: *(a) the alignment parameter $\langle \cos^2 \theta \rangle$ and . (c) the bound states population P_b as a function of time during the pulse for hight-lying and low-lying group (See definition in text) initial states calculated for EXP1. (b) and (d) are the same plots for the EXP2; Both calculation is conducted at the highest intensity $I = 1 \times 10^{14}$ W/cm². The red lines are the correspondent laser field.*

contrary, the long tails of the pulse introduced by the sharp structures in the real spectrum removes the high vibrational states ($v > 8$) contribution in the high KER region, and states contribute to the lower KER region becomes lower in Fig. 6.7(c). The third case in Fig. 6.7(d) further enhances this depletion effect and diminishes the asymmetry signal from $v > 6$ as it introduces much stronger pre-pulse.

On the other hand, lower states typically do not dissociate before the main pulse hits. Instead, molecules starting from these states can align towards the polarization direction so that they are exposed to stronger effective coupling, facilitating multiphoton transitions. Comparing Fig. 6.6(a) and (b), the spectra with the spectral phase in EXP2 produce stronger alignment. Similar depletion is also observed in the calculation for EXP1 using realistic pulse. However, given the fact that it is technically difficult to keep spectral phase flat, the
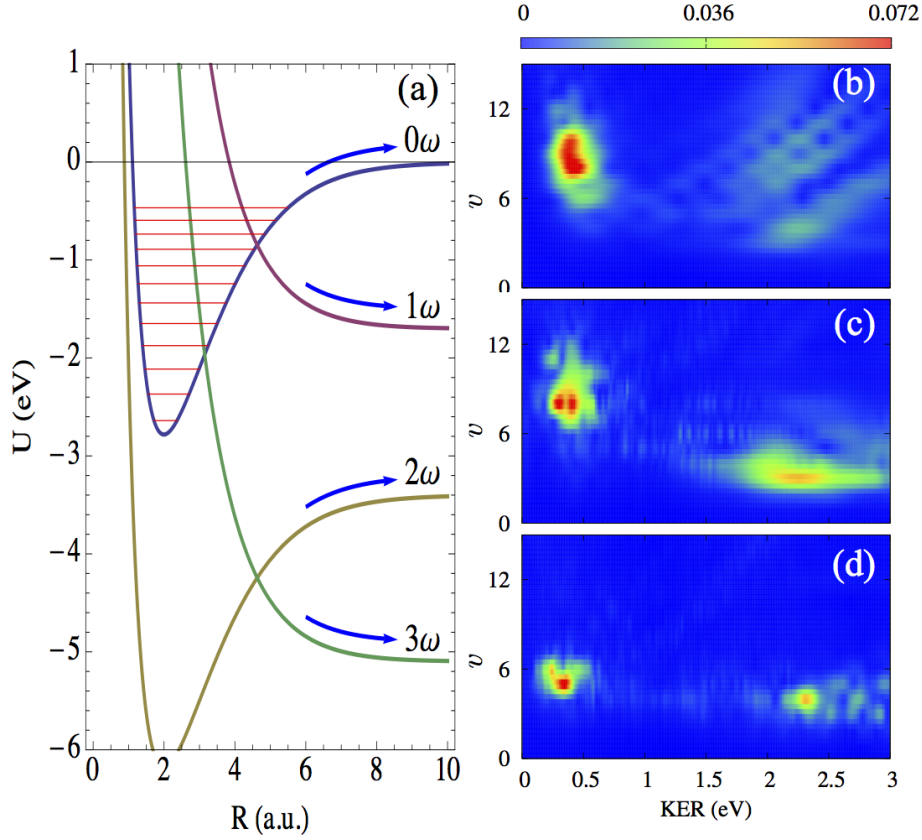
Figure 6.7: *(a) Dressed potential curves for the lowest two electronic states at the center wavelength 700 nm. Contrast parameter C_v of individual vibrational states at different KER for EXP2 at peak intensity $I_0 = 1.6 \times 10^{14}$ W/cm^2 with a (b) Gaussian model pulse (c) pulse Fourier-Transformed from the spectrum without the spectral phase (d) pulse Fourier-Transformed from spectrum with the spectral phase.*

pre- and post- pulse may be more substantial than Fig. 6.4(a) shows, hence stronger long pulse effects may be expected.

6.3.3 Other consideration

Besides the high intensity and the realistic pulse, there are also some other factors that can introduce errors to our calculations. To give a thorough discussion on theoretical errors, we listed all the possibilities based on our current knowledge and experience.

The initial thermal distribution of the ion is ignored in our current theory. The tem-

perature of H_2^+ from an ion source is typically below 400 K [107]. Using $J = M = 0$ as an assumption for the initial rotational states is not an accurate description of the physical conditions in the experiments. However, based on a set of 10 fs calculation at the peak intensity of 1×10^{14} W/cm^2, the comparison between a thermal averaged calculation and one with $J = M = 0$ very limited difference in momentum distribution for the temperature ranging from 200 K to 600 K [107]. We do not expect this result be sensitive to the laser parameter. Therefore, the calculations we showed in this thesis should be reliable in this perspective.

There are assumptions in our mathematical formalism that could potentially introduce errors. As we mentioned in the theoretical background, the non-Born-Oppenheimer coupling and Coriolis effects are ignored. The impact of this is not apparent from the calculation, however, these errors only occur when higher manifolds are included. In the our analysis, the total error are already quantified by the $n = 2$ population. We do not expect that ignoring this coupling would lead to significant change in population. In our analysis, we neglected the electron translation factor [144]. This error is attributed to the asymmetric mass of the fragments in the $p + H$ channel, while the scattering states are the superposition of the symmetric molecular states. however, given the large mass ratio between the electron and proton, and the low KER of the fragments, neglecting this factor should be a fairly good approximation.

It is also important to know the precise geometry of the experimental setup for the cross-beam experiment. The intensity-average in our analysis is based on the assumption of a Gaussian intensity profile of the laser beam. However, it is possible that the actual intensity distribution of the beam in transverse direction follow Bessel distribution or more complicated pattern. Depending on the peak, the Guoy phase may also cause a shift of the CEP in the reaction volume. All of these errors vary with experimental setup. We currently do not have better characterization of the experimental condition but to take the simplest approach to capture the most dominant effects.

6.4 Summary

We carefully conduct a side-by-side comparison between theory and two recently reported experiments on CEP control of asymmetric dissociation of H_2^+. At high intensities ($> 10^{14}$ W/cm^2), the two channel model captures the majority of the dissociation population, yet fails to produce the asymmetry due to higher manifolds. At about $I_0 > 1.6 \times 10^{14}$ W/cm^2, the estimated errors already overwhelm the asymmetry contributed by $1s\sigma_g$ and $2p\sigma_u$. Within this physical limit, the calculation reveals that a realistic pulse, which exhibits long pre-pulse characteristics, produces considerable depletion and alignment effects and alters the asymmetry pattern substantially. The spectral phase turns out to be critical in determining the experimental outcome. The calculations reaffirm that it is the frequency bandwidth that determines the CEP effects instead of the time duration of the pulse.

Unfortunately, we are unable to achieve perfect agreement with the experiments even with the best experimental inputs in the calculation. The mismatch is most likely due to the contribution from the higher manifolds in H_2^+ at higher intensities, and the inaccurate characterization of the laser field. Regardless, the comparisons have been made with meticulous effort, and the uncertainty can be reduced but not completely removed. This raises a general concern that one should be careful in making strong statement by only qualitative agreement in the comparison of theory and experiment in the study of strong fields phenomena.

Chapter 7

Dissociative ionization of H_2

7.1 Overview

Treating dissociative ionization, compared to dissociation only, is a challenging task due to additional degrees of freedom. The existence of unbound electrons introduces immense numerical and conceptual difficulties. The electronic continuum states can not be included with the standard Born-Oppenheimer (BO) approach. Yet, the simultaneous treatment of nuclei and electrons in TDSE requires massive calculations. Compromises have to be made in order to solve this complex problem and they typically can be categorized into two kinds: using a reduced-dimensional model or introducing *ad hoc* treatments to implement a BO approach.

In the first category, the simplest approach is to treat the nuclei and electron both in 1D and study the correlated dynamics on a 2D grid. Many follow this path and choose H_2^+ as the candidate due to its limited degrees of freedom. Numerical studies on such simple system successfully revealed the laser parameter dependence of the competing processes such as excitation, dissociation and ionization in strong fields [67, 145–147], and electron and nuclei energy sharing pattern was also found by such approach [148–150]. Improvement was made by including the electron in full-dimension [63, 151–154]. One crucial issue in solving the multidimensional problem is finding a correct way to analyze the nuclei-electron double continuum. One solution is to propagate the wave function long enough such that

different states can be separated in coordinate space, which allows retrieving the probabilities by the mask projection [67, 147]. The disadvantage of this is that it requires very lengthy propagation to make calculations converge. To overcome this issue, methods such as the energy-resolvant operator [155–157], virtual detector method [152, 158] and scaled-coordinates [153, 154] was used in order to extract the energy spectra without evaluating the continuum eignstates. Alternatively, one can also construct the double-continua as a direct product of the continuum nuclear state and the adiabatic electronic continuum states with fixed nuclei [148]. Despite of the development mentioned above, this multidimensional calculation treating both nuclei and electrons are time-consuming compared to the BO approach, thus a simpler alternative is highly desirable.

In the second category, the core idea is to use a few BO channels to capture the most important physical processes without treating the electrons explicitly. Given the light mass of electrons compared to nuclei, electron is assumed to leave the parent ion instantaneously when ionization takes place. In this case, the nuclear wave function remains unchanged, which yields a Franck-Condon transition. Many studies describe the dissociative ionization of H_2 or its isotopes as an instantaneous ionization followed by dissociation of the ions [70–72, 80, 159–161]. This step usually involves using simple models to acquire ionization probabilities, such as the standard Ammosov–Delone–Krainov theory (ADK) [162] and its variants [129, 163, 164]. In these models, the ionization rate can be approximately derived analytically, which reduces the amount of calculation compared to the TDSE, but the phase information of the wavepackets from different ionization events is lost. Therefore, the wavepackets from different instances are superposed incoherently. Whether or not such coherence plays an important role in the specific observables is still an open question to the field so far. Aside from this question, the rates derived from these ADK-like approaches are very sensitive to the input parameters, such as the field strength and ionization potential. A small changes in the inputs may result in significant modification to the observables in the dissociative ionization. Some studies then focused on examining the accuracy of the

ionization model, especially the radial dependence of the ionization rate in a diatomic problem [165–167]. This R-dependent ionization picture was used to explain the vibrational oscillation observed in the neutral channel [168–170]. Other studies focused on studying the vibrational distribution of the ions after the photoionization. The studies suggest that photoionization yields vibrational distribution more concentrated in the few lower states compared to the Franck-Condon distribution [171–173]. However, this does not directly address whether or not such distribution applies during the middle of a pulse. It should be anticipated that vibrational distribution agrees with FC more if the pulse is significantly shorter than the time scale of the nuclear motion. The further development includes Monte Carlo wavepacket method [174–176], which models the ionization as stochastically process of nuclear wavepackets hopping between different charge states. This simple implementation of BO-like approach, meaning solely treating the nuclei, calculated the KER spectra of the H_2 and D_2 double ionization channel, and reached fairly good agreement with the measurement [177]. These wavepacket approaches provided a simple picture of the dissociative ionization mechanism and pointed out a possibility to simplify the problem.

The current interest to us is to take advantage of our capabilities of performing accurate H_2^+ TDSE calculation in order to explain the phenomena observed in H_2 dissociative ionization. Guided by the wavepacket picture, we consider that electron is tunnel-ionized from H_2 at each half cycle, which creates wavepackets in the ionic states. These wavepackets subsequently evolve on the H_2^+ potentials through the rest of the pulse, as illustrated in Fig. 7.1. If the initial wavepackets are well characterized by the ionization model, the rest of the motion should be well captured by our full-dimensional H_2^+ calculation. Comparing the calculation with experiment may provide insights on the ionization model.

More specifically, we will compare a measurement of spatial asymmetry of $p + H$ fragments from H_2 dissociative ionization using a 6 fs laser pulse [80]. The experiment revealed asymmetry in the low KER region (< 3 eV). The asymmetry in this region is unlikely due to the rescattering process, which results in higher KER of the nuclei. Additionally, the exper-
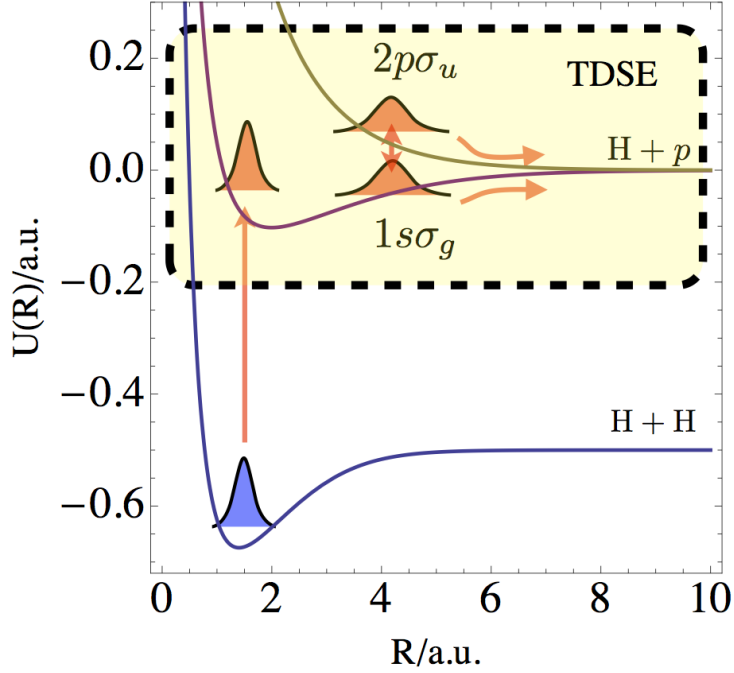
Figure 7.1: *Sketch of the mechanism of dissociative ionization in the wavepacket picture. The curves are the Born-Oppenheimer potentials of* H_2 *and its ion. The wavepackets of* H_2 *ground vibrational state is launched in the FC region. The dominant pathways of the wavepackets are indicated by the orange arrows.*

iment also, for the first time, observed angular dependence of the spatial asymmetry, where our full-dimensional method is natural to incorporate such dependence. We will introduce the details of the modeling step in our calculation below.

7.2 Modeling ionization

We apply the molecular-ADK model [129], which assumes that electronic orbitals in a molecule can be expanded in terms of atomic orbitals in the asymptotic region where the tunneling mechanism can be described by the ADK theory [129]. In a static field picture, the ionization takes place at an approximate constant rate written as below,

$$\omega_{\text{MO-ADK}}(\mathcal{E}) = \frac{B^2(m)}{2^{|m|}|m|!} \frac{1}{\kappa^{(2Z/\kappa)-1}} \left(\frac{2\kappa^3}{\mathcal{E}}\right)^{(2Z/\kappa)-|m|-1} \exp\left[-\frac{2\kappa^3}{3\mathcal{E}}\right], \quad (7.1)$$

and

$$B(m) = \sum_l C_l Q(l, m), \tag{7.2}$$

$$Q(l, m) = (-1)^m \sqrt{\frac{(2l+1)(l+|m|)!}{2(l-|m|)!}}, \tag{7.3}$$

where Z is the Coulomb charge, $\kappa = \sqrt{2I_p}$, I_p is the ionization potential evaluated at the equilibrium distance of H_2 ground channel, l and m are the conventional spherical harmonic indices and the expansion coefficients C_l are provided in Ref. [129]. This rate is very sensitive to the inputs and grows exponentially with the field strength. Figure 7.2 shows the ionization rate as a function of time in a 6 fs long pulse with a center wavelength of 760 nm. The rate shows distinct peaks with a width of 10 a.u. in each half cycle, during which the nuclei are not expect to move substantially. Thus we assume a nuclear wavepacket is "born" at the instant of the individual intensity peak, corresponding to a Franck-Condon wavepacket to be initiated on the $1s\sigma_g$ channel. We do not consider the direct ionization because the ionization probability to those states is much lower according to the tunneling ionization model. Once the wavepackets are born, the following dynamics can be well described by the H_2^+ TDSE calculation. Each event generates one set of observables and eventually is summed incoherently with the weight of its ionization probability.

$$P_\Omega = \sum_i \omega_i \left| \langle \Omega | \Psi(t, t_i) \rangle \right|^2$$

$$\omega_i = \int_{ti-T/4}^{ti+T/4} \omega_{\text{MO-ADK}} \big[\mathcal{E}(t) \big] dt, \tag{7.4}$$

where $\Psi(t, t_i)$ represents the propagated wave function launched at the instance t_i.

Anis showed that starting H_2^+ from $J = 0, M = 0$ state or a thermal distribution yields similar results in a set of calculation with a 10 fs pulse of 800 nm [107]. We assumed the H_2 initially sits in the rotational ground state $J = 0$ and $M = 0$. We do not expect such results to be critically dependent on the laser parameters. Hence, we assume the H_2^+ remains in the rotational ground state and form an coherent Frank-Condon (FC) wavepacket in the
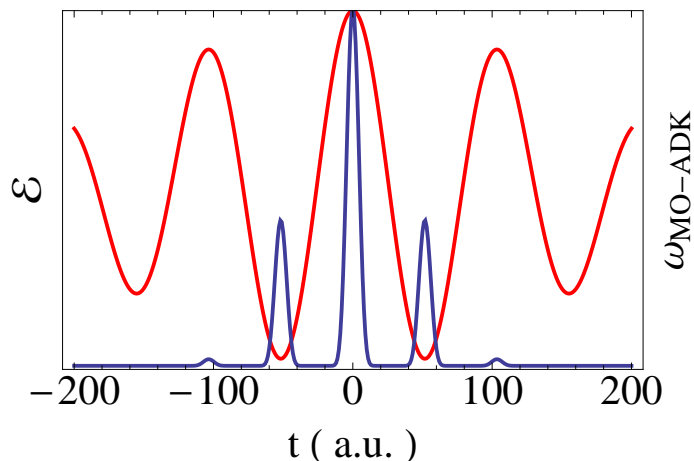
Figure 7.2: *MO-ADK rate as a function of time within a 6 fs pulse with the center wavelength 760 nm at the peak intensity 1×10^{14} W/cm^2.*

radial dimension. Since the equilibrium distance of H$_2$ is 1.6 a.u. while H$_2^+$ is 2 a.u., the initial FC wavepacket will move outwards in the radial direction once launched and couples to the excited channels in the field. To compare with experiments, the intensity-averaging is carried out as described in Eq. (5.2).

7.3 Dissociation of the ion post ionization

The experiment was conducted using a 6 fs long pulse with the center wavelength 760 nm and the peak intensity of 4.4×10^{14} W/cm^2. From Chapter 6, we conclude that performing calculation without ionization is erroneous at such high intensity. However, within this wavepacket ionization model, the evolution of the ions are very different from the previous cases, which can produce a different outcome.

7.3.1 Difference in comparison to dissociation of H$_2^+$

The coherence of the initial vibrational states plays a pivotal role in determining interference pattern of the asymmetry. Unlike starting from a stationary state, a wavepacket will start moving immediately after the ionization. A localized wavepacket is launched at the left

edge of the potential wall of the $1s\sigma_g$ channel as illustrated in Fig. 7.1. In this region, other excited electronic channels of H_2^+ are highly repulsive, where the lowest excited state $2p\sigma_u$ is 18 eV above $1s\sigma_g$ and are not expected to couple with $1s\sigma_g$ efficiently. A classical estimation suggests it takes about 9 fs for a wavepacket to reach the right turning point, which means that the instantaneous intensity falls off considerably when efficient transitions take place. Therefore, even at the very high intensities, a two-channel system is sufficient to capture the dominant physical pathways. This speculation is supported by the KER spectra including the $n = 2$ manifold in Fig. 7.3(a). At the highest intensity 4.4×10^{14} W/cm^2, the total KER spectrum from $n = 2$ is two order of magnitude smaller than the $n = 1$ manifold. This ensures that the our energy analysis is still viable with the assumption that $H_2 \rightarrow H_2^+$ is a vertical transition.

In Fig. 7.3(b), we show the intensity dependence of the asymmetry of H_2 dissociative ionization. The pattern shows similar tilted structures as observed in Fig. 5.3(a), which may result in the cancellation effects due to the intensity variation in the focal volume. However, the ionization model we used suggests that the ionization probability is highly sensitive to changes in the intensity. Consequently, the post-ionization dissociation yield will vary substantially with intensity. Figure 7.3(c) is a plot of the total KER spectra within the intensity range from 1.0×10^{14} W/cm^2 to 4.4×10^{14} W/cm^2. In this range of intensity, the yield decreases more than three orders of magnitude, making the intensity-average in Eq. (5.2) easy to converge with respect to the intensity span. Such intensity-sensitivity makes the results with and without intensity-average surprisingly alike as shown in Fig. 7.4. It is noticeable in the plots that the intensity-averaged one is slightly smaller than unaveraged one, but the qualitative features in both cases are nearly indistinguishable. Even though it appears to suggest that a single intensity calculation is sufficient to predict the experimental outcome qualitatively, it may be an artifact due to the ionization model.
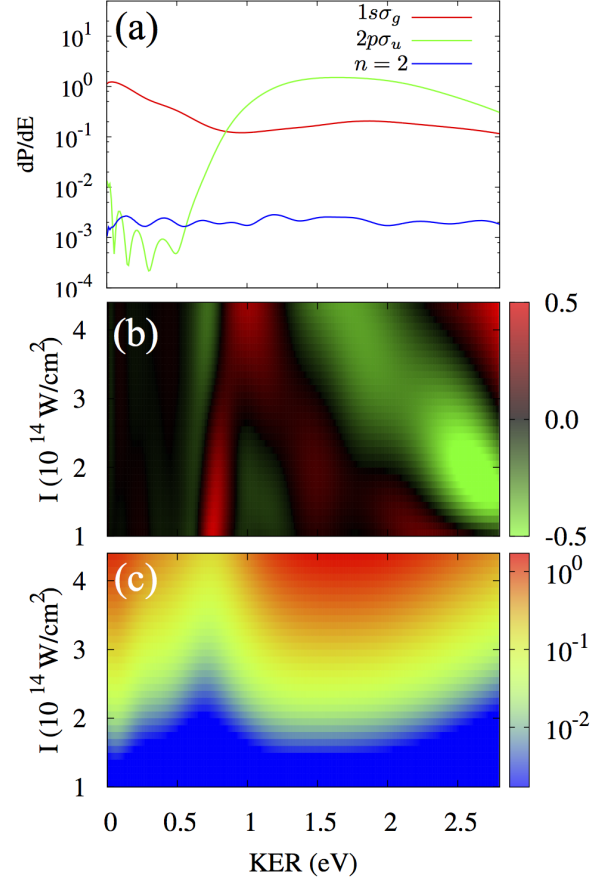
Figure 7.3: *(a) KER spectra of individual electronic channels evaluated at $I = 4.4 \times 10^{14}$ W/cm^2, $\lambda = 760$ nm and $\tau_{\mathrm{FWHM}} = 6$ fs; (b) intensity-dependent asymmetry; (c) intensity-dependent total KER spectra. All three plots assumes $\varphi = 0.0$.*

7.3.2 Comparison with measurements

In Fig. 7.5, we show the intensity averaged asymmetry map integrated within different angles in comparison to the measurement in Ref. [80]. The tilted asymmetry stripe structure is reproduced by our calculation. The similarity exhibits as the slope of the stripes. Even though the experimental results appear to be less contrasty, the qualitative feature is reproduced.

One of the key observation reported in the experiment is the angle-dependent shift
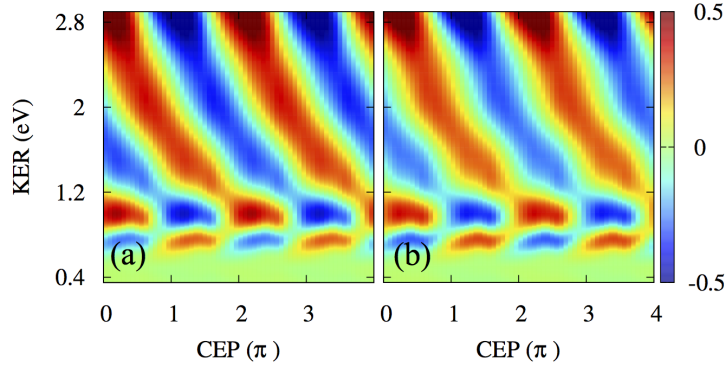
Figure 7.4: *Asymmetry map by integrating over the whole hemisphere at the intensity of* 4.4×10^{14} *W/cm² (a) Non-intensity-averaged (b) intensity-averaged.*

of the asymmetry map, which is quantified by the integrated asymmetry in the energy range 1.4–1.6 eV. Our calculations show the same tendency of the asymmetry shift with angles as shown in Fig. 2 of Ref. [80]. In original paper, 1D H_2^+ calculation based on the same ionization model was used to explain the observed pattern. This reduced-dimension calculation failed to reproduce the angle-dependent shift by simply converting the angle to the effective intensity. If this shift is due to the ionic rotation after the ionization, the angular dependence of asymmetry should be recovered from our full-dimensional calculation. However, the comparison between Fig. 7.5(a) and the measurement is still not so good even though our calculation does produce bigger shift. We also checked calculations at lower intensities, where the shift is even less drastic, therefore, the rotation of the ions is unlikely to be fully responsible for the asymmetry shift. We did not perform calculation at higher intensities because the ionization probability is no longer much smaller than 1, in which case the tunneling ionization rate does not apply any more.

There are several reasons may attribute to the mismatched asymmetry shift. First, the possible inaccurate characterization of the electric field may have ignored the significant pre- and post- pulses. In the current model, the post-pulse can trigger strong post-pulse rotation when the wavepacket reaches the one-photon crossing point as discussed in Chapter 4. Sec-
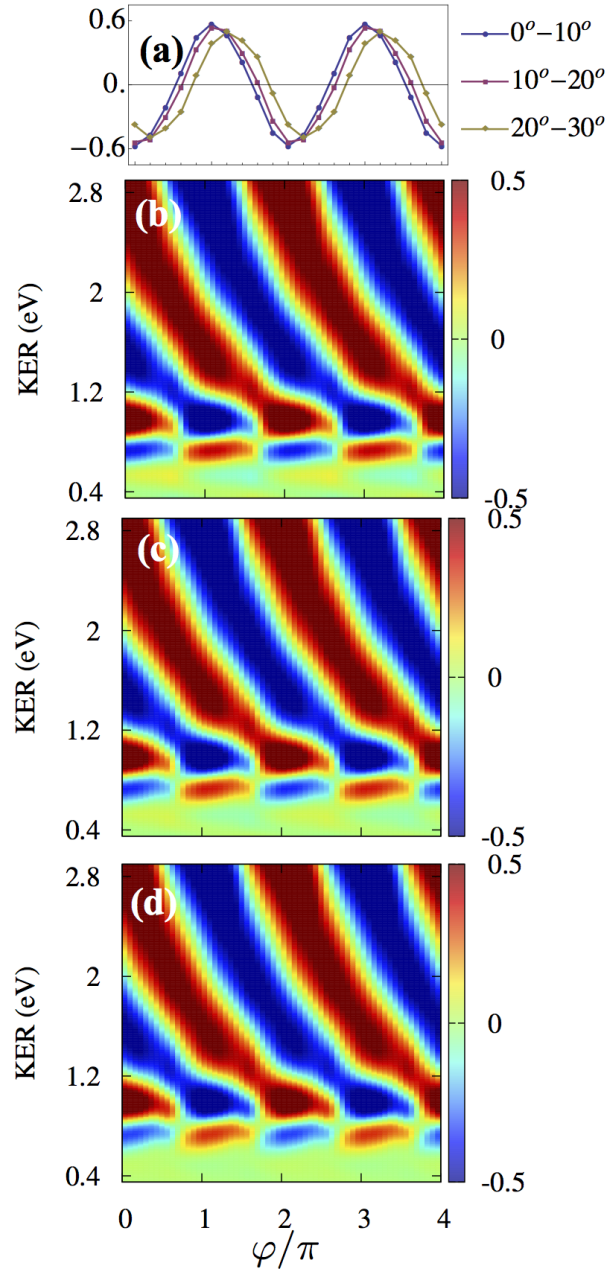
Figure 7.5: *(a) the integrated asymmetry in the energy range 1.4–1.6 eV from the the calculation. (b)(c)(d) are the intensity-averaged spatial asymmetry map from the calculations within the angle 0−10°, 10−20° and 20−30°. The laser parameters are $\lambda = 760$ nm, $I_0 = 4.4 \times 10^{14}$ W/cm² and $\tau_{\mathrm{FWHM}} = 6$ fs.*

ond, we assumed a fairly simple ionization model in our calculation where initial anisotropic distribution and radial dependence of the ionization rate are both ignored. For example, the inclusion of R-dependence of MO-ADK rate is likely to generate initial wavepackets closer to the outer turning point of H_2 because the ionization potential is smaller at larger R. This may lead to more significant transitions between different electronic and rotational channels and dynamics in H_2. Third, the coherence of the initial wavepackets from different ionization times is ignored. To fully recover all detailed features of experiment in theory, it needs further development in modeling the ionization step and better characterization of the field, which will not be covered in this thesis.

7.4 Summary

We transformed the problem of the H_2 dissociative ionization into H_2^+ dissociation by using a standard ionization model. We created multiple Franck-Condon H_2^+ wavepackets at the peaks of the instantaneous intensity. Each of the ionization events is weighted by the ionization probabilities evaluated from MO-ADK theory. We illustrated the difference of the ionic dynamics between dissociative ionization and mere dissociation. The higher manifolds of H_2^+ are unlikely to participate in the process even at very high intensities, because the locality of the wavepacket limits the transition to higher manifolds. Furthermore, due to the intensity-sensitive ionization rate provided by MO-ADK theory, the focal volume effect in dissociative ionization is much less substantial than in dissociation. The final outcome of the calculation resembles the measurement closely, even though the angle-dependent shift of asymmetry is less drastic in theory than the experiment.

Chapter 8

Final remarks

In this dissertation, we studied the dynamical motion of diatomic molecules by an intense few-cycle pulse with H_2^+ as the primary target. We carried out substantial calculations based on the first-principle time-dependent Schrödinger equation. Through numerical calculations, we investigated the post-pulse alignment, carrier-envelope-phase (CEP) controlled spatial asymmetry and total yield of dissociating fragments. In collaboration with experimental groups, we performed quantitative comparison with experiments and pushed beyond seeking for qualitative features. All of these studies are understood within our photon-phase formalism, which allows us to decompose the solution of Schrödinger equation in terms of photons based on the underlying periodicity of CEP. This analysis method not only provides universal picture to understand phenomena in the intense field, but also offers one an simple and robust numerical tool to directly extracting photon information from the time-dependent Schrödinger equation. Even though in many aspects, we succeeded in consolidating our understanding strong field phenomena, the perfect agreement in the theory-experiment comparison is still currently beyond reach.

Combining the efforts of performing accurate numerical calculations and developing systematic physical picture, we made a solid step forward to fully understand and control laser-induced molecular motion. The continuation of this work may lead to the study on more complex physical processes using our photon-phase formalism. For example, the joint energy spectra of nuclei and electron in the dissociative ionization is separated by the photon

energy [148]. It would be interesting to see how individual photon processes participate in the tunneling regime where photon structure is no longer identifiable. We can also extend the CEP study on the high harmonic radiation and possibly provide an alternative picture to the popular three-step model. Besides, given the current experimental conditions and theoretical accuracy, more effort is needed to pin down the least controllable factor in a quantitative theory-experiment comparison.

Bibliography

[1] N. G. Kling, K. J. Betsch, M. Zohrabi, S. Zeng, F. Anis, U. Ablikim, B. Jochim, Z. Wang, M. Kübel, M. F. Kling, K. D. Carnes, B. D. Esry, and I. Ben-Itzhak, Carrier-envelope phase control over pathway interference in strong-field dissociation of H_2^+, Phys. Rev. Lett. **111**, 163004 (2013).

[2] T. Rathje, A. M. Sayler, S. Zeng, P. Wustelt, H. Figger, B. D. Esry, and G. G. Paulus, Coherent control at its most fundamental: Carrier-envelope-phase-dependent electron localization in photodissociation of a H_2^+ molecular ion beam target, Phys. Rev. Lett. **111**, 093002 (2013).

[3] D. Strickland and G. Mourou, Compression of amplified chirped optical pulses, Optics Communications **55**, 447 (1985).

[4] D. E. Spence, P. N. Kean, and W. Sibbett, 60-fsec pulse generation from a self-mode-locked ti:sapphire laser, Opt. Lett. **16**, 42 (1991).

[5] T. Brabec and F. Krausz, Intense few-cycle laser fields: Frontiers of nonlinear optics, Rev. Mod. Phys. **72**, 545 (2000).

[6] J. Posthumus, *Molecules and clusters in intense laser fields*, Cambridge University Press, 2009.

[7] P. Agostini, F. Fabre, G. Mainfray, G. Petite, and N. K. Rahman, Free-free transitions following six-photon ionization of xenon atoms, Phys. Rev. Lett. **42**, 1127 (1979).

[8] D. B. Miloevi, G. G. Paulus, D. Bauer, and W. Becker, Above-threshold ionization by few-cycle pulses, J. Phys. B **39**, R203 (2006).

98

[9] W. Becker, F. Grasbon, R. Kopold, D. Miloevi, G. Paulus, and H. Walther, Above-threshold ionization: From classical features to quantum effects, volume 48 of *Advances In Atomic, Molecular, and Optical Physics*, pages 35 – 98, Academic Press, 2002.

[10] L. Keldysh, Ionization in the field of a strong electromagnetic wave, Sov. Phys. JETP **20**, 1307 (1965).

[11] V. S. Popov, Tunnel and multiphoton ionization of atoms and ions in a strong laser field (keldysh theory), Physics-Uspekhi **47**, 855 (2004).

[12] C. D. Lin, A.-T. Le, Z. Chen, T. Morishita, and R. Lucchese, Strong-field rescattering physicsself-imaging of a molecule by its own electrons, J. Phys. B **43**, 122001 (2010).

[13] F. Krausz and M. Ivanov, Attosecond physics, Rev. Mod. Phys. **81**, 163 (2009).

[14] C. Joachain, M. Dörr, and N. Kylstra, High-intensity laser-atom physics, Adv. At. Mol. Opt. Phys. **42**, 225 (2000).

[15] A. Scrinzi, M. Y. Ivanov, R. Kienberger, and D. M. Villeneuve, Attosecond physics, J. Phys. B **39**, R1.

[16] P. H. Bucksbaum, A. Zavriyev, H. G. Muller, and D. W. Schumacher, Softening of the H_2^+ molecular bond in intense laser fields, Phys. Rev. Lett. **64**, 1883 (1990).

[17] A. Giusti-Suzor, X. He, O. Atabek, and F. H. Mies, Above-threshold dissociation of H_2^+ in intense laser fields, Phys. Rev. Lett. **64**, 515 (1990).

[18] G. Jolicard and O. Atabek, Above-threshold-dissociation dynamics of h_2^+ with short intense laser pulses, Phys. Rev. A **46**, 5845 (1992).

[19] H. Stapelfeldt and T. Seideman, Colloquium: Aligning molecules with strong laser pulses, Rev. Mod. Phys. **75**, 543 (2003).

[20] T. Seideman and E. Hamilton, Nonadiabatic alignment by intense pulses. concepts, theory, and directions, Adv. At. Mol. Opt. Phys. **52**, 289 (2005).

[21] X. Ren, V. Makhija, and V. Kumarappan, Multipulse three-dimensional alignment of asymmetric top molecules, Phys. Rev. Lett. **112**, 173602 (2014).

[22] M. Shapiro and P. Brumer, *Principles of the quantum control of molecular processes*, volume 1, 2003.

[23] M. Shapiro and P. Brumer, Coherent and incoherent laser control of photochemical reactions, International Reviews in Physical Chemistry **13**, 187 (1994).

[24] P. Brumer and M. Shapiro, Laser control of molecular processes, Annu. Rev. Phys. Chem. **43**, 257 (1992).

[25] D. J. Tannor and S. A. Rice, Control of selectivity of chemical reaction via control of wave packet evolution, J. Chem. Phys. **83** (1985).

[26] D. J. Tannor, R. Kosloff, and S. A. Rice, Coherent pulse sequence induced control of selectivity of reactions: Exact quantum mechanical calculations, J. Chem. Phys. **85** (1986).

[27] T. Rathje, N. G. Johnson, M. Mller, F. Smann, D. Adolph, M. Kbel, R. Kienberger, M. F. Kling, G. G. Paulus, and A. M. Sayler, Review of attosecond resolved measurement and control via carrierenvelope phase tagging with above-threshold ionization, J. Phys. B **45**, 074003 (2012).

[28] A. Monmayrant, S. Weber, and B. Chatel, A newcomer's guide to ultrashort pulse shaping and characterization, J. Phys. B **43**, 103001.

[29] C. B. Madsen, L. B. Madsen, S. S. Viftrup, M. P. Johansson, T. B. Poulsen, L. Holmegaard, V. Kumarappan, K. A. Jørgensen, and H. Stapelfeldt, Manipulat-

ing the torsion of molecules by strong laser pulses, Phys. Rev. Lett. **102**, 073007 (2009).

[30] S. M. Parker, M. A. Ratner, and T. Seideman, Coherent control of molecular torsion, J. Chem. Phys. **135**, (2011).

[31] B. G. Levine and T. J. Martnez, Isomerization through conical intersections, Annu. Rev. Phys. Chem. **58**, 613 (2007), PMID: 17291184.

[32] D. J. Jones, S. A. Diddams, J. K. Ranka, A. Stentz, R. S. Windeler, J. L. Hall, and S. T. Cundiff, Carrier-envelope phase control of femtosecond mode-locked lasers and direct optical frequency synthesis, Science **288**, 635 (2000).

[33] R. Holzwarth, T. Udem, T. W. Hänsch, J. C. Knight, W. J. Wadsworth, and P. S. J. Russell, Optical frequency synthesizer for precision spectroscopy, Phys. Rev. Lett. **85**, 2264 (2000).

[34] G. Paulus, F. Grasbon, H. Walther, P. Villoresi, M. Nisoli, S. Stagira, E. Priori, and S. De Silvestri, Absolute-phase phenomena in photoionization with few-cycle laser pulses, Nature **414**, 182 (2001).

[35] G. G. Paulus, F. Lindner, H. Walther, A. Baltuška, E. Goulielmakis, M. Lezius, and F. Krausz, Measurement of the phase of few-cycle laser pulses, Phys. Rev. Lett. **91**, 253004 (2003).

[36] M. J. Abel, T. Pfeifer, A. Jullien, P. M. Nagel, M. J. Bell, D. M. Neumark, and S. R. Leone, Carrier-envelope phase-dependent quantum interferences in multiphoton ionization, J. Phys. B **42**, 075601 (2009).

[37] B. Bergues, S. Zherebtsov, Y. Deng, X. Gu, I. Znakovskaya, R. Kienberger, F. Krausz, G. Marcus, and M. F. Kling, Sub-cycle electron control in the photoionization of xenon using a few-cycle laser pulse in the mid-infrared, New J. Phys. **13**, 063010 (2011).

[38] M. F. Kling, J. Rauschenberger, A. J. Verhoef, E. Hasovi, T. Uphues, D. B. Miloevi, H. G. Muller, and M. J. J. Vrakking, Imaging of carrier-envelope phase effects in above-threshold ionization with intense few-cycle laser fields, New J. Phys. **10**, 025024 (2008).

[39] T. Pfeifer, M. J. Abel, P. M. Nagel, A. Jullien, Z.-H. Loh, M. J. Bell, D. M. Neumark, and S. R. Leone, Time-resolved spectroscopy of attosecond quantum dynamics, Chem. Phys. Lett. **463**, 11 (2008).

[40] S. Chelkowski, A. D. Bandrauk, and A. Apolonski, Phase-dependent asymmetries in strong-field photoionization by few-cycle laser pulses, Phys. Rev. A **70**, 013815 (2004).

[41] S. Chelkowski and A. D. Bandrauk, Asymmetries in strong-field photoionization by few-cycle laser pulses: Kinetic-energy spectra and semiclassical explanation of the asymmetries of fast and slow electrons, Phys. Rev. A **71**, 053815 (2005).

[42] S. Micheau, Z. Chen, T. Morishita, A.-T. Le, and C. D. Lin, Robust carrier-envelope phase retrieval of few-cycle laser pulses from high-energy photoelectron spectra in the above-threshold ionization of atoms, J. Phys. B **42**, 065402 (2009).

[43] T. Tabe, N. Ono, X. M. Tong, and N. Toshima, Laser information encoded in atomic asymmetrical ionization in few-cycle laser fields, Phys. Rev. A **84**, 023409 (2011).

[44] T. Wittmann, B. Horvath, W. Helml, M. Schätzel, X. Gu, A. Cavalieri, G. Paulus, and R. Kienberger, Single-shot carrier–envelope phase measurement of few-cycle laser pulses, Nature Physics **5**, 357 (2009).

[45] A. M. Sayler, T. Rathje, W. Müller, K. Rühle, R. Kienberger, and G. G. Paulus, Precise, real-time, every-single-shot, carrier-envelope phase measurement of ultrashort laser pulses, Opt. Lett. **36**, 1 (2011).

[46] A. M. Sayler, T. Rathje, W. Müller, C. Kürbis, K. Rühle, G. Stibenz, and G. G. Paulus, Real-time pulse length measurement of few-cycle laser pulses using above-threshold ionization, Opt. Exp. **19**, 4464 (2011).

[47] A. Gazibegović-Busuladžić, E. Hasović, M. Busuladžić, D. B. Milošević, F. Kelkensberg, W. K. Siu, M. J. J. Vrakking, F. Lépine, G. Sansone, M. Nisoli, I. Znakovskaya, and M. F. Kling, Above-threshold ionization of diatomic molecules by few-cycle laser pulses, Phys. Rev. A **84**, 043426 (2011).

[48] D. Mathur, K. Dota, A. K. Dharmadhikari, and J. A. Dharmadhikari, Carrier-envelope-phase effects in ultrafast strong-field ionization dynamics of multielectron systems: Xe and CS_2, Phys. Rev. Lett. **110**, 083602 (2013).

[49] S. Zherebtsov et al., Controlled near-field enhanced electron acceleration from dielectric nanospheres with intense few-cycle laser fields, Nature Physics **7**, 656 (2011).

[50] S. Zherebtsov, F. Smann, C. Peltz, J. Plenge, K. J. Betsch, I. Znakovskaya, A. S. Alnaser, N. G. Johnson, M. Kbel, A. Horn, V. Mondes, C. Graf, S. A. Trushin, A. Azzeer, M. J. J. Vrakking, G. G. Paulus, F. Krausz, E. Rhl, T. Fennel, and M. F. Kling, Carrier-envelope phase-tagged imaging of the controlled electron acceleration from SiO_2 nanospheres in intense few-cycle laser fields, New J. Phys. **14**, 075010 (2012).

[51] M. Krüger, M. Schenk, and P. Hommelhoff, Attosecond control of electrons emitted from a nanoscale metal tip, Nature **475**, 78 (2011).

[52] P. B. Corkum, Plasma perspective on strong field multiphoton ionization, Phys. Rev. Lett. **71**, 1994 (1993).

[53] K. J. Schafer, B. Yang, L. F. DiMauro, and K. C. Kulander, Above threshold ionization beyond the high harmonic cutoff, Phys. Rev. Lett. **70**, 1599 (1993).

[54] M. Lewenstein, P. Balcou, M. Y. Ivanov, A. L'Huillier, and P. B. Corkum, Theory of high-harmonic generation by low-frequency laser fields, Phys. Rev. A **49**, 2117 (1994).

[55] P. Raith, C. Ott, K. Meyer, A. Kaldun, M. Laux, M. Ceci, C. P. Anderson, and T. Pfeifer, Carrier-envelope phase- and spectral control of fractional high-harmonic combs, J. Appl. Phys. **114**, (2013).

[56] C. Ott, M. Schnwald, P. Raith, A. Kaldun, G. Sansone, M. Krger, P. Hommelhoff, Y. Patil, Y. Zhang, K. Meyer, M. Laux, and T. Pfeifer, Strong-field spectral interferometry using the carrier-envelope phase, New J. Phys. **15**, 073031 (2013).

[57] T. Pfeifer, A. Jullien, M. J. Abel, P. M. Nagel, L. Gallmann, D. M. Neumark, and S. R. Leone, Generating coherent broadbandcontinuum soft-X-ray radiation byattosecond ionization gating, Opt. Exp. **15**, 17120 (2007).

[58] A. Jullien, T. Pfeifer, M. Abel, P. Nagel, M. Bell, D. Neumark, and S. Leone, Ionization phase-match gating for wavelength-tunable isolated attosecond pulse generation, Appl. Phys. B. **93**, 433 (2008).

[59] E. Mansten, J. M. Dahlström, J. Mauritsson, T. Ruchon, A. L'Huillier, J. Tate, M. B. Gaarde, P. Eckle, A. Guandalini, M. Holler, F. Schapper, L. Gallmann, and U. Keller, Spectral signature of short attosecond pulse trains, Phys. Rev. Lett. **102**, 083002 (2009).

[60] G. Sansone, E. Benedetti, J. P. Caumes, S. Stagira, C. Vozzi, M. Nisoli, L. Poletto, P. Villoresi, V. Strelkov, I. Sola, L. B. Elouga, A. Zair, E. Mével, and E. Constant, Shaping of attosecond pulses by phase-stabilized polarization gating, Phys. Rev. A **80**, 063837 (2009).

[61] C. Haworth, L. Chipperfield, J. Robinson, P. Knight, J. Marangos, and J. Tisch, Half-cycle cutoffs in harmonic spectra and robust carrier-envelope phase retrieval, Nature Physics **3**, 52 (2007).

[62] N. Ishii, K. Kaneshima, K. Kitano, T. Kanai, S. Watanabe, and J. Itatani, Carrier-envelope phase-dependent high harmonic generation in the water window using few-cycle infrared pulses, Nature Communications **5** (2014).

[63] V. Roudnev, B. D. Esry, and I. Ben-Itzhak, Controlling HD^+ and H_2^+ dissociation with the carrier-envelope phase difference of an intense ultrashort laser pulse, Phys. Rev. Lett. **93**, 163601 (2004).

[64] J. J. Hua and B. D. Esry, The role of mass in the carrierenvelope phase effect for H_2^+ dissociation, J. Phys. B **42**, 085601 (2009).

[65] F. He, Control of electron localization in the dissociation of H_2^+ using orthogonally polarized two-color sequential laser pulses, Phys. Rev. A **86**, 063415 (2012).

[66] Z.-T. Liu, K.-J. Yuan, C.-C. Shu, W.-H. Hu, and S.-L. Cong, The carrier-envelope phase dependence of above threshold dissociation for HD^+ driven by the modulated laser field, J. Phys. B **43**, 055601 (2010).

[67] K. Liu, W. Hong, Q. Zhang, and P. Lu, Wavelength dependence of electron localization in the laser-driven dissociation of H_2^+, Opt. Exp. **19**, 26359 (2011).

[68] P. Lan, E. J. Takahashi, K. Liu, Y. Fu, and K. Midorikawa, Carrier envelope phase dependence of electron localization in the multicycle regime, New J. Phys. **15**, 063023 (2013).

[69] F. Anis and B. D. Esry, Enhancing the intense field control of molecular fragmentation, Phys. Rev. Lett. **109**, 133001 (2012).

[70] D. Geppert, P. von den Hoff, and R. de Vivie-Riedle, Electron dynamics in molecules: a new combination of nuclear quantum dynamics and electronic structure theory, J. Phys. B **41**, 074006 (2008).

[71] X. M. Tong and C. D. Lin, Dynamics of light-field control of molecular dissociation at the few-cycle limit, Phys. Rev. Lett. **98**, 123002 (2007).

[72] F. Kelkensberg, G. Sansone, M. Y. Ivanov, and M. Vrakking, A semi-classical model of attosecond electron localization in dissociative ionization of hydrogen, Phys. Chem. Chem. Phys. **13**, 8647 (2011).

[73] F. He and A. Becker, Coherent control of electron localization in a dissociating hydrogen molecular ion, J. Phys. B **41**, 074017 (2008).

[74] F. He, C. Ruiz, and A. Becker, Coherent control of electron wave packets in dissociating H_2^+, Journal of Physics B: Atomic, Molecular and Optical Physics **41**, 081003 (2008).

[75] M. Kling, C. Siedschlag, A. Verhoef, J. Kahn, M. Schultze, Y. Ni, T. Uphues, M. Uiberacker, M. Drescher, F. Krausz, and M. Vrakking, Control of electron localization in molecular dissociation, Science **312**, 246 (2006).

[76] M. Kling, C. Siedschlag, I. Znakovskaya, A. Verhoef, S. Zherebtsov, F. Krausz, M. Lezius, and M. Vrakking, Strong-field control of electron localisation during molecular dissociation, Mol. Phys. **106**, 455 (2008).

[77] I. Znakovskaya, P. von den Hoff, S. Zherebtsov, A. Wirth, O. Herrwerth, M. J. J. Vrakking, R. de Vivie-Riedle, and M. F. Kling, Attosecond control of electron dynamics in carbon monoxide, Phys. Rev. Lett. **103**, 103002 (2009).

[78] Y. Liu, X. Liu, Y. Deng, C. Wu, H. Jiang, and Q. Gong, Selective steering of molecular multiple dissociative channels with strong few-cycle laser pulses, Phys. Rev. Lett. **106**, 073004 (2011).

[79] K. J. Betsch, N. G. Johnson, B. Bergues, M. Kübel, O. Herrwerth, A. Senftleben, I. Ben-Itzhak, G. G. Paulus, R. Moshammer, J. Ullrich, M. F. Kling, and R. R. Jones,

Controlled directional ion emission from several fragmentation channels of co driven by a few-cycle laser field, Phys. Rev. A **86**, 063403 (2012).

[80] M. Kremer, B. Fischer, B. Feuerstein, V. L. B. de Jesus, V. Sharma, C. Hofrichter, A. Rudenko, U. Thumm, C. D. Schröter, R. Moshammer, and J. Ullrich, Electron localization in molecular fragmentation of H_2 by carrier-envelope phase stabilized laser pulses, Phys. Rev. Lett. **103**, 213003 (2009).

[81] I. Znakovskaya, P. von den Hoff, N. Schirmel, G. Urbasch, S. Zherebtsov, B. Bergues, R. de Vivie-Riedle, K.-M. Weitzel, and M. Kling, Waveform control of orientation-dependent ionization of DCl in few-cycle laser fields, Phys. Chem. Chem. Phys. **13**, 8653 (2011).

[82] H. Xu, J.-P. Maclean, D. E. Laban, W. C. Wallace, D. Kielpinski, R. T. Sang, and I. V. Litvinyuk, Carrier-envelope-phase-dependent dissociation of hydrogen, New J. Phys. **15**, 023034 (2013).

[83] X. Xie, K. Doblhoff-Dier, S. Roither, M. S. Schöffler, D. Kartashov, H. Xu, T. Rathje, G. G. Paulus, A. Baltuška, S. Gräfe, and M. Kitzler, Attosecond-recollision-controlled selective fragmentation of polyatomic molecules, Phys. Rev. Lett. **109**, 243001 (2012).

[84] E. Lötstedt and K. Midorikawa, Laser-induced electron localization in a triatomic molecular ion, Phys. Rev. A **88**, 041402 (2013).

[85] E. Lötstedt and K. Midorikawa, Carrier-envelope phase control of electron motion in laser-driven H_3^{2+}, J. Phys. B **47**, 204018 (2014).

[86] I. Znakovskaya, P. von den Hoff, G. Marcus, S. Zherebtsov, B. Bergues, X. Gu, Y. Deng, M. J. J. Vrakking, R. Kienberger, F. Krausz, R. de Vivie-Riedle, and M. F. Kling, Subcycle controlled charge-directed reactivity with few-cycle midinfrared pulses, Phys. Rev. Lett. **108**, 063002 (2012).

[87] K. Liu, Q. Zhang, P. Lan, and P. Lu, Anomalous isotopic effect on electron-directed reactivity by a 3-μm midinfrared pulse, Opt. Exp. **21**, 5107 (2013).

[88] A. Gürtler, F. Robicheaux, W. J. van der Zande, and L. D. Noordam, Asymmetry in the strong-field ionization of rydberg atoms by few-cycle pulses, Phys. Rev. Lett. **92**, 033002 (2004).

[89] P. K. Jha, Y. V. Rostovtsev, H. Li, V. A. Sautenkov, and M. O. Scully, Experimental observation of carrier-envelope-phase effects by multicycle pulses, Phys. Rev. A **83**, 033404 (2011).

[90] E. Lötstedt and K. Midorikawa, Nuclear reaction induced by carrier-envelope-phase controlled proton recollision in a laser-driven molecule, Phys. Rev. Lett. **112**, 093001 (2014).

[91] M. F. Kling, P. von den Hoff, I. Znakovskaya, and R. de Vivie-Riedle, (sub-)femtosecond control of molecular reactions via tailoring the electric field of light, Phys. Chem. Chem. Phys. **15**, 9448 (2013).

[92] M. J. J. Vrakking, Attosecond imaging, Phys. Chem. Chem. Phys. **16**, 2775 (2014).

[93] V. Roudnev and B. D. Esry, General theory of carrier-envelope phase effects, Phys. Rev. Lett. **99**, 220406 (2007).

[94] J. P. Boyd, *Chebyshev and Fourier spectral methods*, Courier Dover Publications, 2001.

[95] M. G. Pullen, W. C. Wallace, D. E. Laban, A. J. Palmer, G. F. Hanne, A. N. Grum-Grzhimailo, K. Bartschat, I. Ivanov, A. Kheifets, D. Wells, H. M. Quiney, X. M. Tong, I. V. Litvinyuk, R. T. Sang, and D. Kielpinski, Measurement of laser intensities approaching 10^{15} w/cm^2 with an accuracy of 1%, Phys. Rev. A **87**, 053411 (2013).

[96] S.-I. Chu and D. A. Telnov, Beyond the floquet theorem: generalized floquet formalisms and quasienergy methods for atomic and molecular multiphoton processes in intense laser fields, Phys. Rep. **390**, 1 (2004).

[97] J. H. Shirley, Solution of the schrödinger equation with a hamiltonian periodic in time, Phys. Rev. **138**, B979 (1965).

[98] T.-S. Ho and S.-I. Chu, Coupled dressed-states formalism for multiphoton excitation and population inversion by coherent pulses, Chem. Phys. Lett. **141**, 315 (1987).

[99] I. Horenko, B. Schmidt, and C. Schtte, A theoretical model for molecules interacting with intense laser pulses: The floquet-based quantum-classical liouville equation, J. Chem. Phys. **115**, 5733 (2001).

[100] U. Peskin and N. Moiseyev, The solution of the timedependent schrdinger equation by the (t,t) method: Theory, computational algorithm and applications, J. Chem. Phys. **99** (1993).

[101] M. W. J. Bromley and B. D. Esry, Classical aspects of ultracold atom wave packet motion through microstructured waveguide bends, Phys. Rev. A **69**, 053620 (2004).

[102] F. Anis and B. D. Esry, Role of nuclear rotation in dissociation of H_2^+ in a short laser pulse, Phys. Rev. A **77**, 033416 (2008).

[103] B. D. Esry and H. R. Sadeghpour, Adiabatic formulation of heteronuclear hydrogen molecular ion, Phys. Rev. A **60**, 3604 (1999).

[104] E. Hamilton, T. Seideman, T. Ejdrup, M. D. Poulsen, C. Z. Bisgaard, S. S. Viftrup, and H. Stapelfeldt, Alignment of symmetric top molecules by short laser pulses, Phys. Rev. A **72**, 043402 (2005).

[105] S. E. Koonin, K. T. R. Davies, V. Maruhn-Rezwani, H. Feldmeier, S. J. Krieger, and

J. W. Negele, Time-dependent hartree-fock calculations for ^{16}O + ^{16}O and ^{40}Ca + ^{40}Ca reactions, Phys. Rev. C **15**, 1359 (1977).

[106] J. Colgan, M. S. Pindzola, and F. Robicheaux, Time-dependent studies of single and multiple photoionization of H_2^+, Phys. Rev. A **68**, 063413 (2003).

[107] F. Anis, *ROLE OF NUCLEAR ROTATION IN* H_2^+ *DISSOCIATION BY ULTRA-SHORT LASER PULSES*, PhD thesis, Kansas State University, 2009.

[108] N. Owschimikow, B. Schmidt, and N. Schwentner, Laser-induced alignment and anti-alignment of rotationally excited molecules, Phys. Chem. Chem. Phys. **13**, 8671 (2011).

[109] T. Seideman, On the dynamics of rotationally broad, spatially aligned wave packets, J. Chem. Phys. **115**, 5965 (2001).

[110] M. Leibscher, I. S. Averbukh, and H. Rabitz, Molecular alignment by trains of short laser pulses, Phys. Rev. Lett. **90**, 213001 (2003).

[111] S. Zhao, P. Liu, Y. Li, R. Li, and Z. Xu, Controlling coherent population transfer in molecular alignment using two laser pulses, Chem. Phys. Lett. **480**, 67 (2009).

[112] V. Makhija, X. Ren, and V. Kumarappan, Metric for three-dimensional alignment of molecules, Phys. Rev. A **85**, 033425 (2012).

[113] X. Ren, V. Makhija, and V. Kumarappan, Measurement of field-free alignment of jet-cooled molecules by nonresonant femtosecond degenerate four-wave mixing, Phys. Rev. A **85**, 033405 (2012).

[114] T. Seideman, Rotational excitation and molecular alignment in intense laser fields, J. Chem. Phys. **103**, 7887 (1995).

[115] R. Torres, R. de Nalda, and J. P. Marangos, Dynamics of laser-induced molecular alignment in the impulsive and adiabatic regimes: A direct comparison, Phys. Rev. A **72**, 023420 (2005).

[116] S. Fleischer, Y. Zhou, R. W. Field, and K. A. Nelson, Molecular orientation and alignment by intense single-cycle thz pulses, Phys. Rev. Lett. **107**, 163603 (2011).

[117] G. Herzberg, Molecular spectra and molecular structure, (1957).

[118] R. Numico, A. Keller, and O. Atabek, Intense-laser-induced alignment in angularly resolved photofragment distributions of H_2^+, Phys. Rev. A **60**, 406 (1999).

[119] L. J. Frasinski, J. H. Posthumus, J. Plumridge, K. Codling, P. F. Taday, and A. J. Langley, Manipulation of bond hardening in H_2^+ by chirping of intense femtosecond laser pulses, Phys. Rev. Lett. **83**, 3625 (1999).

[120] J. H. Posthumus, J. Plumridge, L. J. Frasinski, K. Codling, E. J. Divall, A. J. Langley, and P. F. Taday, Slow protons as a signature of zero-photon dissociation of H_2^+ in intense laser fields, J. Phys. B **33**, L563 (2000).

[121] F. Anis, T. Cackowski, and B. D. Esry, Rotational dynamics of dissociating H_2^+ in a short intense laser pulse, J. Phys. B **42**, 091001 (2009).

[122] M. Fischer, U. Lorenz, B. Schmidt, and R. Schmidt, Fragmentation due to centrifugal forces in the photodissociation of H_2^+ in intense laser fields, Phys. Rev. A **84**, 033422 (2011).

[123] R. Numico, A. Keller, and O. Atabek, Laser-induced molecular alignment in dissociation dynamics, Phys. Rev. A **52**, 1298 (1995).

[124] J. H. Posthumus, The dynamics of small molecules in intense laser fields, Rep. Prog. Phys. **67**, 623 (2004).

[125] A. Giusti-Suzor, F. H. Mies, L. F. DiMauro, E. Charron, and B. Yang, Dynamics of H_2^+ in intense laser fields, J. Phys. B **28**, 309 (1995).

[126] R. N. Zare, Dissociation of H_2^+ by electron impact: Calculated angular distribution, J. Chem. Phys. **47**, 204 (1967).

[127] X. M. Tong, Z. X. Zhao, A. S. Alnaser, S. Voss, C. L. Cocke, and C. D. Lin, Post ionization alignment of the fragmentation of molecules in an ultrashort intense laser field, J. Phys. B **38**, 333 (2005).

[128] S. Voss, A. S. Alnaser, X.-M. Tong, C. Maharjan, P. Ranitovic, B. Ulrich, B. Shan, Z. Chang, C. D. Lin, and C. L. Cocke, High resolution kinetic energy release spectra and angular distributions from double ionization of nitrogen and oxygen by short laser pulses, J. Phys. B **37**, 4239 (2004).

[129] X. M. Tong, Z. X. Zhao, and C. D. Lin, Theory of molecular tunneling ionization, Phys. Rev. A **66**, 033402 (2002).

[130] E. Wrede, E. R. Wouters, M. Beckert, R. N. Dixon, and M. N. R. Ashfold, Quasiclassical and quantum mechanical modeling of the breakdown of the axial recoil approximation observed in the near threshold photolysis of IBr and Br_2, J. Chem. Phys. **116**, 6064 (2002).

[131] H. Adaniya, B. Rudek, T. Osipov, D. J. Haxton, T. Weber, T. N. Rescigno, C. W. McCurdy, and A. Belkacem, Imaging the molecular dynamics of dissociative electron attachment to water, Phys. Rev. Lett. **103**, 233201 (2009).

[132] D. S. Slaughter, D. J. Haxton, H. Adaniya, T. Weber, T. N. Rescigno, C. W. McCurdy, and A. Belkacem, Ion-momentum imaging of resonant dissociative-electron-attachment dynamics in methanol, Phys. Rev. A **87**, 052711 (2013).

[133] C.-C. Shu, K.-J. Yuan, W.-H. Hu, and S.-L. Cong, Carrier-envelope phase-dependent field-free molecular orientation, Phys. Rev. A **80**, 011401 (2009).

[134] B. GAIRE, *IMAGING OF SLOW DISSOCIATION OF THE LASER INDUCED FRAGMENTATION OF MOLECULAR ION*, PhD thesis, Kansas State University, 2011.

[135] F. He, C. Ruiz, and A. Becker, Control of electron excitation and localization in the dissociation of H_2^+ and its isotopes using two sequential ultrashort laser pulses, Phys. Rev. Lett. **99**, 083002 (2007).

[136] P. Lan, E. J. Takahashi, and K. Midorikawa, Efficient control of electron localization by subcycle waveform synthesis, Phys. Rev. A **86**, 013418 (2012).

[137] P. Q. Wang, A. M. Sayler, K. D. Carnes, J. F. Xia, M. A. Smith, B. D. Esry, and I. Ben-Itzhak, Dissociation of H_2^+ in intense femtosecond laser fields studied by coincidence three-dimensional momentum imaging, Phys. Rev. A **74**, 043411 (2006).

[138] I. Ben-Itzhak, P. Q. Wang, J. F. Xia, A. M. Sayler, M. A. Smith, K. D. Carnes, and B. D. Esry, Dissociation and ionization of H_2^+ by ultrashort intense laser pulses probed by coincidence 3d momentum imaging, Phys. Rev. Lett. **95**, 073002 (2005).

[139] F. von Busch and G. H. Dunn, Photodissociation of H_2^+ and D_2^+ experiment, Phys. Rev. A **5**, 1726 (1972).

[140] P. Q. Wang, A. M. Sayler, K. D. Carnes, J. F. Xia, M. A. Smith, B. D. Esry, and I. Ben-Itzhak, Highlighting the angular dependence of bond softening and bond hardening of H_2^+ in an ultrashort intense laser pulse, J. Phys. B **38**, L251 (2005).

[141] N. G. Johnson, O. Herrwerth, A. Wirth, S. De, I. Ben-Itzhak, M. Lezius, B. Bergues, M. F. Kling, A. Senftleben, C. D. Schröter, R. Moshammer, J. Ullrich, K. J. Betsch,

R. R. Jones, A. M. Sayler, T. Rathje, K. Rühle, W. Müller, and G. G. Paulus, Single-shot carrier-envelope-phase-tagged ion-momentum imaging of nonsequential double ionization of argon in intense 4-fs laser fields, Phys. Rev. A **83**, 013412 (2011).

[142] H. R. Sadeghpour, C. H. Greene, and M. Cavagnero, Extensive eigenchannel R-matrix study of the h$^-$ photodetachment spectrum, Phys. Rev. A **45**, 1587 (1992).

[143] T. Nakajima and E. Cormier, Effects of the carrier-envelope phase of chirped laser pulses in the multiphoton ionization regime, Opt. Lett. **32**, 2879 (2007).

[144] W. R. Thorson and J. B. Delos, Theory of near-adiabatic collisions. i. electron translation factor method, Phys. Rev. A **18**, 117 (1978).

[145] K. C. Kulander, F. H. Mies, and K. J. Schafer, Model for studies of laser-induced nonlinear processes in molecules, Phys. Rev. A **53**, 2562 (1996).

[146] G. L. V. Steeg, K. Bartschat, and I. Bray, Time-dependent model calculations for a molecular hydrogen ion in a strong ultra-short laser pulse, J. Phys. B **36**, 3325 (2003).

[147] S. Chelkowski, T. Zuo, O. Atabek, and A. D. Bandrauk, Dissociation, ionization, and coulomb explosion of H_2^+ in an intense laser field by numerical integration of the time-dependent schrödinger equation, Phys. Rev. A **52**, 2977 (1995).

[148] C. B. Madsen, F. Anis, L. B. Madsen, and B. D. Esry, Multiphoton above threshold effects in strong-field fragmentation, Phys. Rev. Lett. **109**, 163003 (2012).

[149] R. E. F. Silva, F. Catoire, P. Rivière, H. Bachau, and F. Martín, Correlated electron and nuclear dynamics in strong field photoionization of H_2^+, Phys. Rev. Lett. **110**, 113001 (2013).

[150] L. Yue and L. B. Madsen, Dissociation and dissociative ionization of $H_2{}^+$ using the time-dependent surface flux method, Phys. Rev. A **88**, 063420 (2013).

[151] S. Chelkowski, A. Conjusteau, T. Zuo, and A. D. Bandrauk, Dissociative ionization of H_2^+ in an intense laser field: Charge-resonance-enhanced ionization, coulomb explosion, and harmonic generation at 600 nm, Phys. Rev. A **54**, 3235 (1996).

[152] H.-X. He, R.-F. Lu, P.-Y. Zhang, K.-L. Han, and G.-Z. He, Dissociation and ionization competing processes for H_2^+ in intense laser field: Which one is larger?, J. Chem. Phys. **136**, (2012).

[153] V. Roudnev and B. D. Esry, HD^+ in a short strong laser pulse: Practical consideration of the observability of carrier-envelope phase effects, Phys. Rev. A **76**, 023403 (2007).

[154] V. Roudnev and B. D. Esry, HD^+ photodissociation in the scaled coordinate approach, Phys. Rev. A **71**, 013411 (2005).

[155] K. J. Schafer and K. C. Kulander, Energy analysis of time-dependent wave functions: Application to above-threshold ionization, Phys. Rev. A **42**, 5794 (1990).

[156] F. Catoire and H. Bachau, Extraction of the absolute value of the photoelectron spectrum probability density by means of the resolvent technique, Phys. Rev. A **85**, 023422 (2012).

[157] F. Catoire, R. E. F. Silva, P. Rivière, H. Bachau, and F. Martín, Molecular resolvent-operator method: Electronic and nuclear dynamics in strong-field ionization, Phys. Rev. A **89**, 023415 (2014).

[158] B. Feuerstein and U. Thumm, On the computation of momentum distributions within wavepacket propagation calculations, J. Phys. B **36**, 707 (2003).

[159] F. He and U. Thumm, Dissociative ionization of h_2 in an attosecond pulse train and delayed laser pulse, Phys. Rev. A **81**, 053413 (2010).

[160] T. Niederhausen and U. Thumm, Controlled vibrational quenching of nuclear wave packets in $D_2{}^+$, Phys. Rev. A **77**, 013407 (2008).

[161] U. Thumm, T. Niederhausen, and B. Feuerstein, Time-series analysis of vibrational nuclear wave-packet dynamics in D_2^+, Phys. Rev. A **77**, 063401 (2008).

[162] M. V. Ammosov, N. B. Delone, and V. P. Krainov, Tunnel ionization of complex atoms and atomic ions in electromagnetic field, Sov. Phys. JETP **0664**, 138 (1986).

[163] X. M. Tong and C. D. Lin, Empirical formula for static field ionization rates of atoms and molecules by lasers in the barrier-suppression regime, J. Phys. B **38**, 2593 (2005).

[164] A. Perelomov, V. Popov, and M. Terentev, Ionization of atoms in an alternating electric field, Sov. Phys. JETP **23**, 924 (1966).

[165] A. Saenz, Behavior of molecular hydrogen exposed to strong dc, ac, or low-frequency laser fields. ii. comparison of ab initio and ammosov-delone-krainov rates, Phys. Rev. A **66**, 063408 (2002).

[166] M. Awasthi and A. Saenz, Internuclear-distance dependence of ionization of H_2 in strong laser fields, J. Phys. B **39**, S389 (2006).

[167] L. B. Madsen and M. Plummer, H_2^+ in intense laser fields: mechanisms for enhanced ionization in the multiphoton regime, J. Phys. B **31**, 87 (1998).

[168] E. Goll, G. Wunner, and A. Saenz, Formation of ground-state vibrational wave packets in intense ultrashort laser pulses, Phys. Rev. Lett. **97**, 103003 (2006).

[169] L. Fang and G. N. Gibson, Strong-field induced vibrational coherence in the ground electronic state of hot I_2, Phys. Rev. Lett. **100**, 103003 (2008).

[170] T. Ergler, B. Feuerstein, A. Rudenko, K. Zrost, C. D. Schröter, R. Moshammer, and J. Ullrich, Quantum-phase resolved mapping of ground-state vibrational D_2 wave packets via selective depletion in intense laser pulses, Phys. Rev. Lett. **97**, 103004 (2006).

[171] X. Urbain, B. Fabre, E. M. Staicu-Casagrande, N. de Ruette, V. M. Andrianarijaona, J. Jureta, J. H. Posthumus, A. Saenz, E. Baldit, and C. Cornaggia, Intense-laser-field ionization of molecular hydrogen in the tunneling regime and its effect on the vibrational excitation of H_2^+, Phys. Rev. Lett. **92**, 163004 (2004).

[172] T. K. Kjeldsen and L. B. Madsen, Vibrational excitation of diatomic molecular ions in strong field ionization of diatomic molecules, Phys. Rev. Lett. **95**, 073004 (2005).

[173] T. K. Kjeldsen and L. B. Madsen, Strong-field ionization of diatomic molecules and companion atoms: Strong-field approximation and tunneling theory including nuclear motion, Phys. Rev. A **71**, 023411 (2005).

[174] H. A. Leth, L. B. Madsen, and K. Mølmer, Monte carlo wave packet theory of dissociative double ionization, Phys. Rev. Lett. **103**, 183601 (2009).

[175] H. A. Leth, L. B. Madsen, and K. Mølmer, Monte carlo wave packet approach to dissociative multiple ionization in diatomic molecules, Phys. Rev. A **81**, 053409 (2010).

[176] H. A. Leth, L. B. Madsen, and K. Mølmer, Dissociative double ionization of H_2 and D_2: Comparison between experiment and monte carlo wave packet calculations, Phys. Rev. A **81**, 053410 (2010).

[177] A. Staudte, D. Pavičić, S. Chelkowski, D. Zeidler, M. Meckel, H. Niikura, M. Schöffler, S. Schössler, B. Ulrich, P. P. Rajeev, T. Weber, T. Jahnke, D. M. Villeneuve, A. D. Bandrauk, C. L. Cocke, P. B. Corkum, and R. Dörner, Attosecond strobing of two-surface population dynamics in dissociating H_2^+, Phys. Rev. Lett. **98**, 073003 (2007).

[178] B. H. Bransden and C. J. Joachain, *Physics of Atoms and Molecules*, volume 2nd Ed., New York: Prentice-Hall, 2003.

Appendix A

Representing electronic wave function with linear combination of atomic orbitals (LCAO)

To approximate the adiabatic electronic wavefunction to a reasonable accuracy, we use the superposition of two $1s$ atomic orbital to construct the lowest two electronic state $1s\sigma_g$ and $2p\sigma_u$ of H_2^+. The derivation follows the procedure in Ref. [178] in combination with the variational principle for better accuracy. The electronic Hamiltonian in two centers $H = T - \frac{1}{r_A} - \frac{1}{r_B} + \frac{1}{R}$ is symmetric or anti-symmetric under exchange operator:

$$\Pi_{AB}\Psi(\mathbf{r}_A, \mathbf{r}_B) = \Psi(\mathbf{r}_B, \mathbf{r}_A) = \pm\Psi(\mathbf{r}_A, \mathbf{r}_B) \tag{A.1}$$

then

$$\Psi(\mathbf{r}) = N\big[\phi_{1s}(\mathbf{r}_A) \pm \phi_{1s}(\mathbf{r}_B)\big] \tag{A.2}$$

where N is the renormalization factor and ϕ_{1s} is the $1s$ atomic wavefunction $\phi_{1s}(\mathbf{r}_i) = (Z^3/\pi)^{1/2}e^{-Zr_i}$. We apply the variational principle with respect to the Z. For the simplicity of the notation, we use $|\mathbf{r}_A\rangle$ to mark $1s$ atomic orbital ϕ_{1s}.

$$\frac{\langle\Psi|H|\Psi\rangle}{\langle\Psi|\Psi\rangle} = \frac{\langle\mathbf{r}_A|H|\mathbf{r}_A\rangle + \langle\mathbf{r}_B|H|\mathbf{r}_B\rangle \pm 2\langle\mathbf{r}_A|H|\mathbf{r}_B\rangle}{2 \pm 2\langle\mathbf{r}_A|\mathbf{r}_B\rangle}$$

$$= E_\alpha(Z) + \frac{1}{R} + \frac{\langle\mathbf{r}_A|\frac{Z-1}{r_A} - \frac{1}{r_B}|\mathbf{r}_A\rangle + \langle\mathbf{r}_B|\frac{Z-1}{r_B} - \frac{1}{r_A}|\mathbf{r}_B\rangle \pm 2\langle\mathbf{r}_A|\frac{Z-1}{r_B} - \frac{1}{r_B}|\mathbf{r}_B\rangle}{2 \pm 2\langle\mathbf{r}_A|\mathbf{r}_B\rangle}$$

$$= -\frac{1}{2}Z^2 + \frac{1}{R} + \frac{(Z-1)\langle\frac{1}{r}\rangle - J \pm (Z-2)K}{1 \pm I}, \tag{A.3}$$

where the two-center integral I,J,K can be evaluated in confocal elliptic coordinates analytically,

$$I = \langle\mathbf{r}_A|\mathbf{r}_B\rangle = \frac{1}{3}e^{-ZR}(Z^2R^2 + 3ZR + 3),$$

$$J = \langle\mathbf{r}_A|\frac{1}{r_B}|\mathbf{r}_B\rangle = \frac{1}{R}e^{-2ZR}(-ZR - 1 + e^{2ZR}), \tag{A.4}$$

$$K = \langle\mathbf{r}_A|\frac{1}{r_B}|\mathbf{r}_B\rangle = Ze^{-ZR}(ZR + 1).$$

This yields the final variation form of the Hamiltonian in terms of Z and R,

$$\frac{\langle\Psi|H|\Psi\rangle}{\langle\Psi|\Psi\rangle} = -\frac{1}{2}Z^2 + \frac{1}{R}$$
$$+ \frac{1}{R}\frac{(Z-1)ZR - 1 + e^{-2ZR}(ZR+1) \pm (Z-2)ZR(ZR+1)e^{-ZR}}{1 \pm (1 + ZR + Z^2R^2/3)e^{-ZR}} \tag{A.5}$$

Then solve the transcendental equation,

$$\frac{\partial}{\partial Z}\left(\frac{\langle\Psi|H|\Psi\rangle}{\langle\Psi|\Psi\rangle}\right)\bigg|_{Z=Z_{\text{eff}}} = 0, \tag{A.6}$$

for Z_{eff} as a function of R. The solutions for both channels are plotted in Fig. A.1. The values of both cases at large R approaches 1 as expected from the separate atom limit. On the other hand, two curves diverge at small R due to different parity. In the $1s\sigma_g$ channel, Z_{eff} rises as two nuclei become closer due to the stronger attraction from both nuclei. The value of Z_{eff} eventually approach 2 at $R \to 0$, resembling He$^+$. In the $2p\sigma_u$ channel, Z_{eff} decreases in small R because the electronic wavefunction heavily cancel each other near the center, compelling the electronic density further out. The potentials for the given Z_{eff} are compared to the exact potentials in Fig. A.1(b). The overall characteristics of

	a	b	c	d	e	f
$1s\sigma_g$	1.042	5.597	5.086	3.100	1.668	1.7065
$2p\sigma_u$	-0.5711	0.8581	-0.5276	0.8291	0.3609	0.9846

Table A.1: *Coefficients for the fitting function of the effective charge in $Z_{eff}(R) = ae^{-bR} + cRe^{-dR} + eR^2e^{-fR} + 1$*

.

the potentials are reproduced by LCAO, nevertheless there is visible discrepancy in the $1s\sigma_g$ channel. However, for the purpose of obtaining pictorial sense of electronic dynamics, it is more than sufficient. For convenience, the LCAO potentials can be fitted to an analytical form with reasonable accuracy. The fitting function and its coefficients are given in Tab. A,
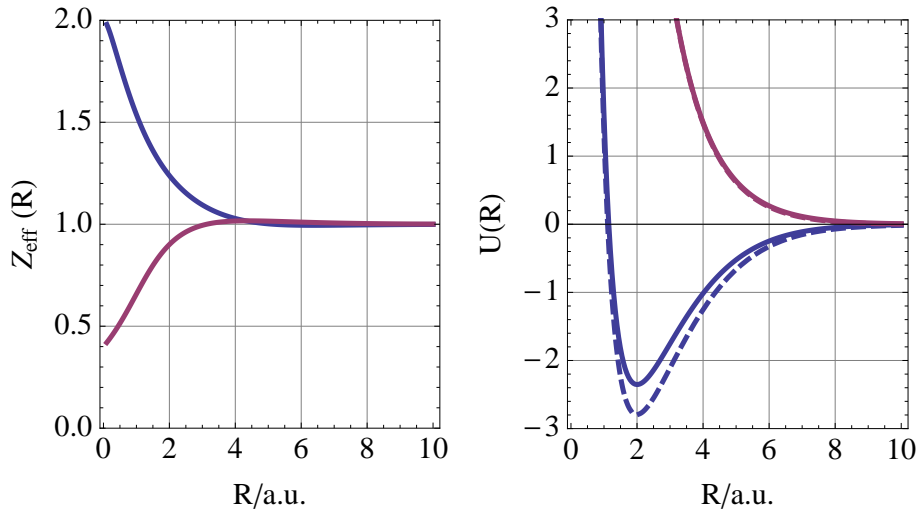

Figure A.1: *The calculated effective charge number Z_{eff} and the potential curves as a function of R for $1s\sigma_g$ and $2p\sigma_u$ channels. The blue curves are for $1s\sigma_g$ and the red curves are for $2p\sigma_u$. The dashed lines are the exact potentials as a comparison with the LCAO results.*

Appendix B

Error analysis in the numerical calculation

Absent of statistical deviation and the equipment accuracy error in experiments, a theoretical calculation introduces its own error caused by numerical convergences and other factors. It is, in general, very useful to have a systematic description to quantify these errors, especially when the observables span several order of magnitude.

Being specific about the problem, we aim to provide error bars for the intensity-averaged FC-averaged KER spectra and asymmetry in order to compare to experiments. Given differential observables $P(\Omega; E)$, where Ω represents all parameters, for instance, the time-step, total propagation time, the peak intensity *etc*, we intend to form the results as the following format :

$$
\begin{aligned}
\tilde{P}_{g/u}(\Omega; E) &= P_{g/u}(\Omega; E) \pm \Delta_{g/u}(E) \\
\mathcal{A}(\Omega; E) &= \frac{P_A(\Omega; E) - P_B(\Omega; E)}{P_A(\Omega; E) + P_B(\Omega; E)} \\
\tilde{\mathcal{A}}(\Omega; E) &= \mathcal{A}(\Omega; E) \pm \Delta_{\mathcal{A}}(E)
\end{aligned}
\tag{B.1}
$$

where Δ are the errors and the tilde signs on top of observables mean the final form of the quantities with error bars. One can deduce the error of asymmetry based on Eq. (6.4). In our problem, Δ are mainly caused by three factors: (1) $\Delta^{(1)}$ convergence error restricted by the input parameters and the numerical method, (2) $\Delta^{(2)}$ due to the physical approximation, (3) $\Delta^{(3)}$ due to the interpolation to the discrete data points.

The first kind error $\Delta^{(1)}$ can be quantified as

$$\Delta^{(1)} = |P(\Omega; E) - P(\Omega_b; E)| \tag{B.2}$$

and Ω_b is the best convergence parameter set. To be emphasized, this is only one approach to estimate the error. The best convergence parameters are limited by the computation capability we can afford within reasonable timescale. On top of the numerical convergence error, the main approximation error is ignoring the higher manifold as well as the ionization. This error is quantified by comparing the difference of the calculations with and without include $n = 2$ manifold

$$\Delta^{(2)} = |P(\Omega, n\text{Max} = 1; E) - P(\Omega, n\text{Max} = 2; E)| \tag{B.3}$$

As for the third kind of errors $\Delta^{(3)}$ due to the intensity-averaging, we have to take a slightly different approach because this type of error is actually a consequences of accumulating the first two types of errors. Besides, generating a dense grid for numerous intensities is very inefficient for the purpose of estimating the overall errors. According to the intensity average procedure in Eq. (5.2), one can write down

$$\begin{aligned} \bar{P}(\Omega, I_0; E) &= \int^{I_0} P(\Omega, I; E) d\ln I \\ &= \sum_i P(\Omega, I_i; E)\delta \ln I \end{aligned} \tag{B.4}$$

then

$$\begin{aligned} \Delta_{\bar{P}} &= \delta \ln I \sqrt{\sum_i P(\Omega, I_i; E)^2} \\ &= \delta \ln I \sqrt{\sum_i (\frac{\Delta_{P_i}}{P_i} P_i)^2} &&(\text{ assume } \tfrac{\Delta_{P_i}}{P_i} \text{ is constant}) \\ &= \delta \ln I \frac{\Delta_{P_i}}{P_i} \sqrt{\sum_i P_i^2} \\ &< \delta \ln I \frac{\Delta_{P_i}}{P_i} \sqrt{(\sum_i P_i)^2} \end{aligned} \tag{B.5}$$
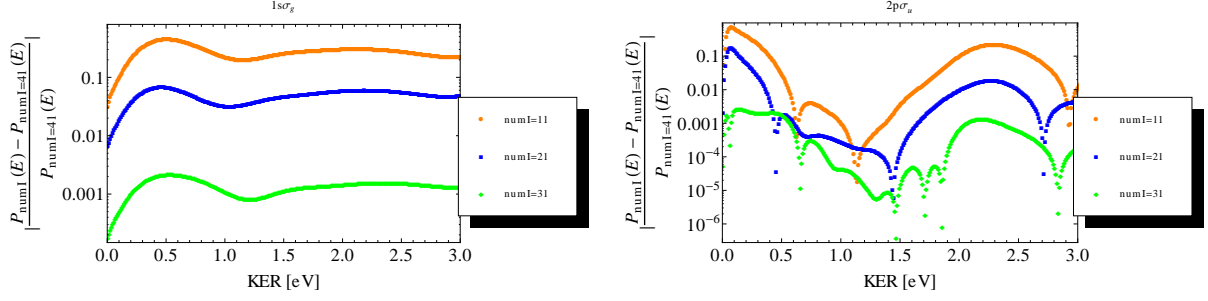
Figure B.1: *The convergence of KER spectrum of each molecular channel with respect to the intensity grid points. The maximum grids points is 41 in our calculation across the range from 10^{10} to 10^{14} W/cm^2.*

thus we conclude

$$\frac{\Delta_{\bar{P}}}{\bar{P}} < \frac{\Delta_{P_i}}{P_i} \tag{B.6}$$

This expression above is concluded from the assumption that observables at every intensity I_i can be calculated directly with sufficiently dense grid points to make Eq. (B.4) valid, in which case the relative error will not be larger than the error of a single intensity calculation. No interpolation has been taken into account so far. To estimate how accurate the interpolation is, one simple approach is to see the convergence of the integrated quantity with respect to intensity points.

$$\Delta^{(3)} < \left| \bar{P}(\Omega, \text{num}I = \text{Max}; E) - \bar{P}(\Omega, \text{num}I'; E) \right| \tag{B.7}$$

From Fig. B.1, we know that intensity-averaged KER spectra are converged to 2-3 digits across the whole KER range. So $\Delta^{(3)}$ is typically one order of magnitude smaller than $\Delta^{(1)}$ and even much smaller than $\Delta^{(2)}$, therefore the interpolation errors is negligible in the following discussion.

Based on Eq. (B.6), we are able to determine the accuracy of $\bar{P}$ by showing the convergence result of P at a single intensity 1×10^{14} W/cm^2. In Fig. B.2, the calculated KER
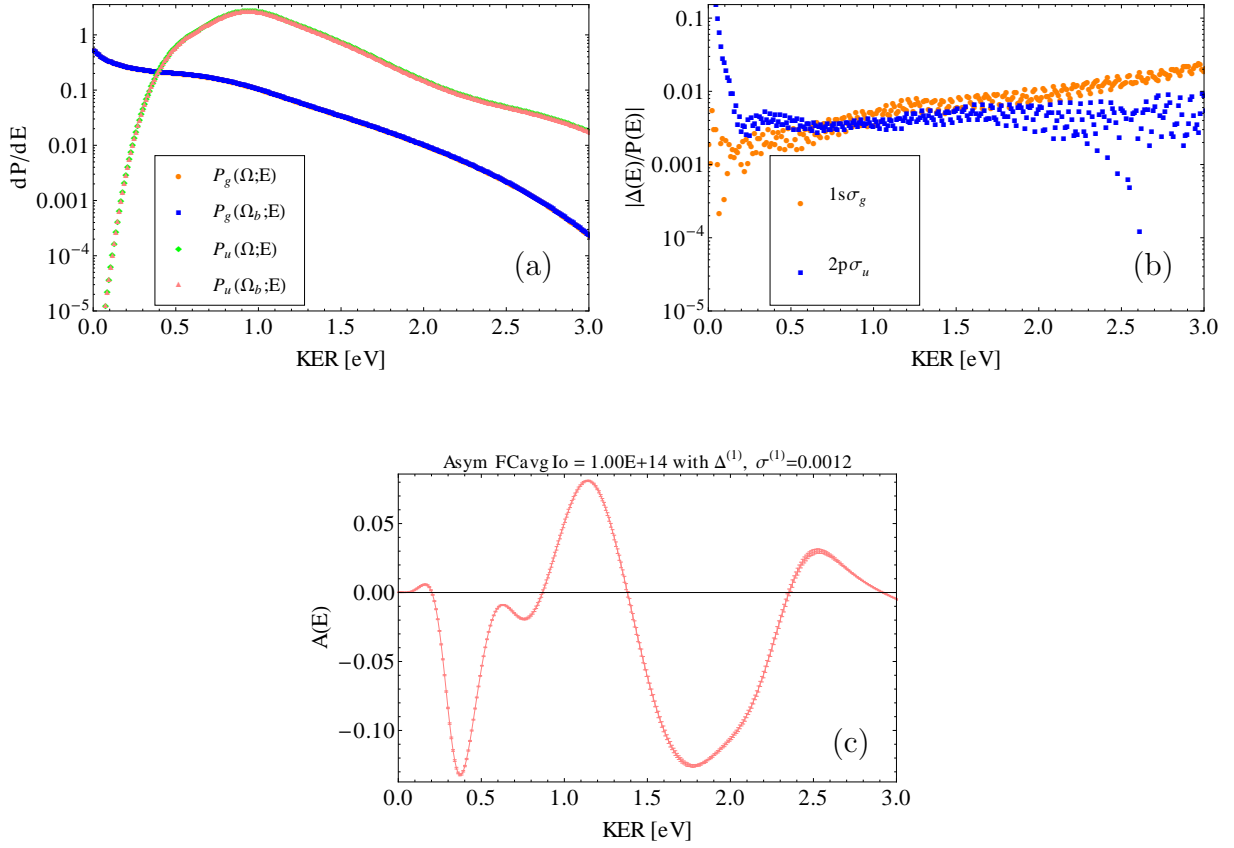
Figure B.2: *(a) KER spectra $P_{g/u}(\Omega; E)$ and $P_{g/u}(\Omega_b; E)$;(b) the relative first kind of errors $\Delta^{(1)}/P$; (c) the asymmetry with error bar $\Delta^{(1)}$. These plots are all generated from the calculation at a single intensity of 1×10^{14} W/cm^2*

distribution are overall converged to about 2 digits across the energy range 0-3 eV. As for the asymmetry, defining the accuracy in terms of convergence digits is not very appropriate for the fact that the asymmetry is not a positive-definite function. To display the overall accuracy, we apply standard deviation to quantify errors. Following the similar notation,
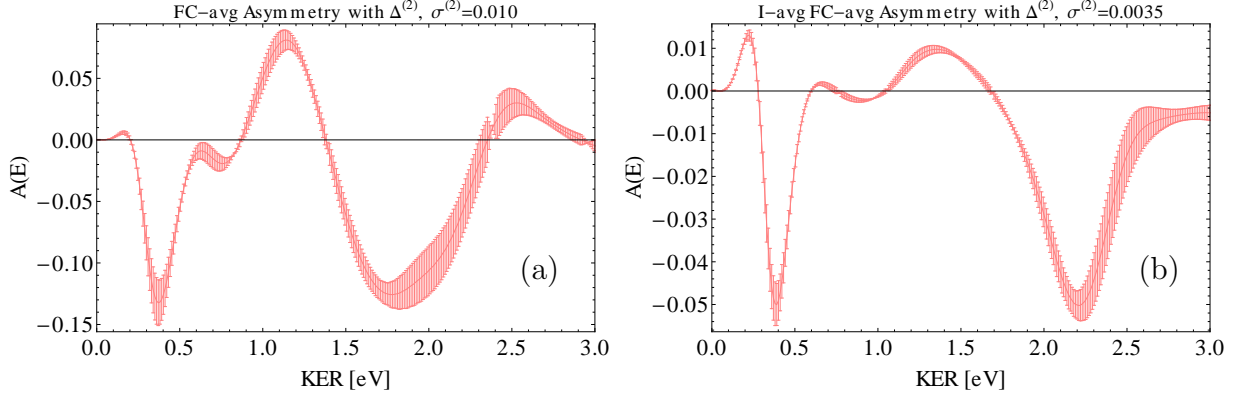
Figure B.3: *(a) FC-averaged Asymmetry with the second kind of error $\Delta^{(2)}$; (b) same plot with the intensity-averaged quantities. Both quantities are calculated at the peak intensity 1×10^{14} W/cm^2.*

we define:

$$\sigma_{\mathcal{A}}^{(1)} = \sqrt{\frac{1}{n_E} \sum_i^{n_E} \Big(\mathcal{A}(\Omega; E) - \mathcal{A}(\Omega_b; E) \Big)^2}$$

$$\sigma_{\mathcal{A}}^{(2)} = \sqrt{\frac{1}{n_E} \sum_i^{n_E} \Big(\mathcal{A}(\Omega, n\mathrm{Max} = 1; E) - \mathcal{A}(\Omega, n\mathrm{Max} = 2; E) \Big)^2} \qquad \text{(B.8)}$$

where n_E is the number of energy points within the $0 - 3\mathrm{eV}$. The value is given along the Fig. B.2 and B.3. The results are sufficiently accurate from the respective to convergence, however, the main error comes from the second kind of error especially at the high intensity 1×10^{14} W/cm^2. As we can notice in Fig. B.3, the modification to the asymmetry caused by higher manifolds are significant if quantitative comparisons with experiments are needed at this intensity. Even though the procedure of intensity average, which is likely to enhance the contribution from the lower intensities, however, the effects of higher manifold to the asymmetry is not yet negligible.

Appendix C

Numerical improvement for TDSE

This appendix is to provide some details of parallelizing the finite difference code for H_2^+ by using OpenMP. A simple and substantial improvement of performance can be implemented by identifying parallelizable procedure in the short-time propagator when solving Eq. 3.5,

$$\mathbf{F}(R, t + \delta) = e^{-i\delta\mathbf{H}(t+\delta/2)}\mathbf{F}(R, t). \tag{C.1}$$

The total Hamiltonian matrix $\mathbf{H}$ is split into the field-free kinetic part $\mathbf{H}_0$ and the dipole coupling part $\mathbf{V}(t)$ as below,

$$e^{-i\delta\mathbf{H}(t+\delta/2)} \approx e^{-i\delta\mathbf{H}_0/2}e^{-i\delta\mathbf{V}(t+\delta/2)}e^{-i\delta\mathbf{H}_0/2}. \tag{C.2}$$

Each sub-step of the propagator is reduced to a linear system problem by Cranck-Nicolson method,

$$\left(\mathbf{I} - i\delta\mathbf{H}_0/4\right)\mathbf{F}(t + \delta/2) = \left(\mathbf{I} + i\delta\mathbf{H}_0/4\right)\mathbf{F}(t)$$
$$\left(\mathbf{I} - i\delta\mathbf{V}(t + \delta/2)/2\right)\mathbf{F}(t + \delta) = \left(\mathbf{I} + i\delta\mathbf{V}(t + \delta/2)/2\right)\mathbf{F}(t). \tag{C.3}$$

In this case, the propagation of each sub-step is substantially more efficient by taking advantage of the regular matrix structure in $\mathbf{H}_0$ and $\mathbf{V}(t)$. For $\mathbf{H}_0$, propagations of different electronic and rotational channels are completely independent, thus can be treated in parallel with minimal penalty. Similar parallelism works for the coupling operator because dipole operator is a local operator that only couples different channels at the same R. More specif-
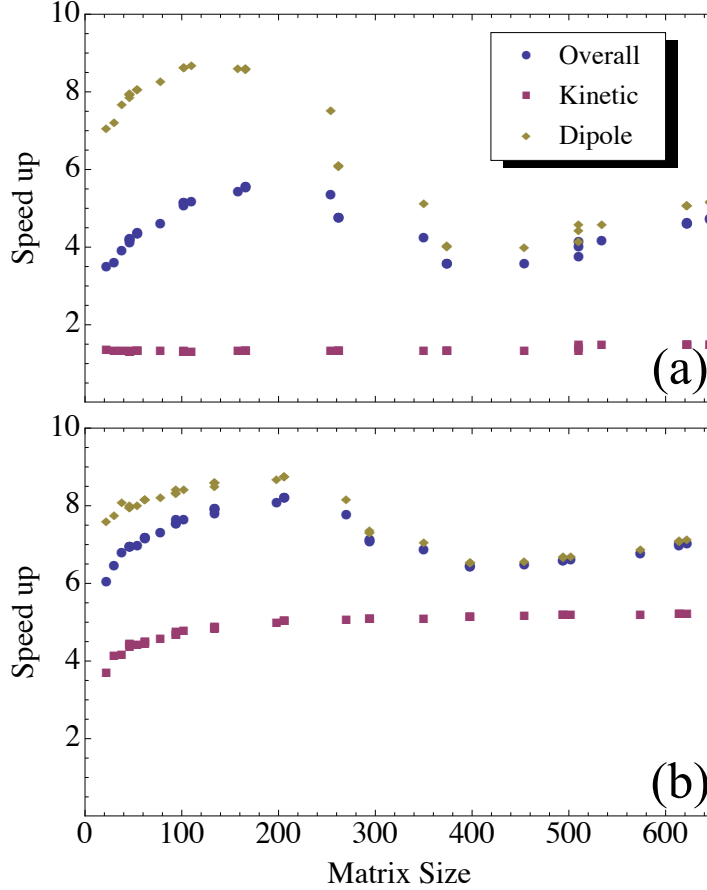
Figure C.1: *Speedup by enabling OpenMP to during the time-propagation of. (a) The test results in a calculation with* 11939 *radial points; (b) with* 2694 *radial points. Both cases include the* $n = 2$ *manifold, corresponding to eight electronic channels.*

ically, $\mathbf{H}_0$ is tri-diagnal and $\mathbf{V}(t)$ is banded matrix in our finite-difference scheme, which can be solved very efficiently with Intel math kernel library.

Given that our parallelism avoids the communication, the performance speedup is expected to linearly scale with number of cores available. However, depending on the matrix size in the calculations, the overall speedup gained from using OpenMP is about 4–8 on a 12-cores machine with two Xeon X5650 CPUs. In our calculations, we dynamically adapt the J_{Max} during propagation, which reduces the number of floating point operations. The matrix size in the dipole propagator, namely the number of channels in the kinetic propaga-

tor, changes in time accordingly. In Fig. C.1, we show the calculation speedup in comparison to the serial code as a function of this matrix size. In both cases, the speedup gained in the kinetic propagator relatively limited and does not vary significantly as the matrix size changes, especially in the case of larger radial grid. This signals that the underlying operation, a tridiagonal linear system, is not a CPU-bound problem. Instead, the performance is limited by the memory bandwidth during the data communication between the CPU and memory. On the other hand, the dipole propagator has better performance in terms of occupying multiple cores. This is likely due to the fact that banded matrices require more operations per data compared to the tridiagonal linear solve. The overall performance gain is mostly attributed to speed up the dipole coupling propagator as witnessed that the blue and yellow dots converge towards each other as the matrix size increases. The practical speedup may be more significant than what Fig. C.1 shows because the baseline of this comparison, single-thread calculation, is likely to be affected by running multiple jobs at the same time. Depending on the job size, the cache-, memory- competition can slow down the calculation to a non-trivial amount. Generally speaking, by taking advantage of the split-operator, we are able to use OpenMP directives to shorten calculation time by a significant amount, which largely benefits the quantitative comparison study in Chapter 6.